High Frequency Ultrasonic Characterization of Human Skin *In Vivo*

by

Balasundara I. Raju

B. Tech., Mechanical Engineering
Indian Institute of Technology, Madras, India, 1994

M.S., Mechanical Engineering
Massachusetts Institute of Technology, 1998

M.S., Electrical Engineering and Computer Science
Massachusetts Institute of Technology, 1998

Submitted to the Department of Electrical Engineering and Computer Science
in Partial Fulfillment of the Requirements for the Degree of
Doctor of Philosophy
at the

MASSACHUSETTS INSTITUTE OF TECHNOLOGY

June 2002

Author.....
Department of Electrical Engineering and Computer Science
April 11, 2002

Certified by.....
Dr. Mandayam A. Srinivasan
Principal Research Scientist
Thesis Supervisor

Certified by..
Prof. Dennis M. Freeman
Associate Professor of Electrical Engineering
Thesis Supervisor

Accepted by.....
Arthur C. Smith
Chairman, Departmental Committee on Graduate Students

High frequency ultrasonic characterization of human skin *in vivo*

by

Balasundara I. Raju

Submitted to the Department of Electrical Engineering and Computer Science
on April 11, 2002, in partial fulfillment of the
requirements for the degree of Doctor of Philosophy in
Electrical Engineering and Computer Science

High frequency (>20 MHz) ultrasound has numerous potential applications in dermatology because of its ability to penetrate several millimeters into the skin and provide information at a spatial resolution of tens of microns. However, conventional B-scan images of skin tissues often lack the capability to characterize and differentiate various skin tissues. In this work, quantitative ultrasonic methods using the attenuation coefficient, backscatter coefficient, and echo envelope statistics were studied for their potential to characterize human skin tissues *in vivo*.

A high frequency ultrasound system was developed using polymer transducers, a pulser/receiver, high-speed digitizer, 3-axis scanning system, and a PC. Data collected using three different transducers with center frequencies of 28, 30 and 44 MHz were processed to determine the characteristics of normal human dermis and subcutaneous fat. Attenuation coefficients were obtained by computing spectral slopes vs. depth, with the transducers axially translated to minimize diffraction effects. Backscatter coefficients were obtained by compensating recorded backscatter spectra for system-dependent effects, and additionally for one transducer, using the reference phantom technique. Good agreement was seen between the results from the different transducers/methods. The attenuation coefficients were well described by a linear frequency dependence whose slope showed significant differences between the forearm and fingertip dermis, but not between the forearm dermis and fat. The backscatter coefficient of the dermis showed an increasing trend with frequency and was significantly higher than that of fat. A maximum likelihood fit of six probability distributions (Rayleigh, Rician, K, Nakagami, Weibull, and Generalized Gamma) to fluctuations in echo envelope data showed that the Generalized Gamma distribution modeled the envelope better than the other distributions. Fat was seen to exhibit significantly more pre-Rayleigh behavior than the dermis. Data were also obtained from the skin of patients patch-tested for contact dermatitis. A significant increase in skin thickness, decrease in mean backscatter of the upper dermis, and decrease in attenuation coefficient slope was found at the affected sites compared to normal skin. However, no differences in terms of echo statistics were found in the mid-dermis. These results indicate that a combination of ultrasonic parameters have the potential to non-invasively characterize skin tissues.

Thesis committee:
Dr. Mandayam A. Srinivasan (advisor)
Prof. Dennis M. Freeman (advisor)
Prof. Arthur B. Baggeroer
Dr. Timothy K. Stanton

Acknowledgements

During the course of graduate studies, especially at the doctoral level, one often wonders whether all the effort is worth it. I am happy to say that in my case the answer is a resounding "yes". I think one of the reasons for this is the friendship I had forged with many people over the past several years at MIT. Graduate school, and research in general, is a team effort. A level of independence and maturity is required, but it is rare to be able to do useful work without the help of others. I will make an attempt to acknowledge some of the people who have made this thesis possible. To others who ought be mentioned, but I have forgotten, I can only say that this has to do with my memory and not with my intentions. If you have known me before, and are reading this, chances are that I have benefited from knowing you, and you are worth a mention here.

Before I get to thank any specific individual, I must first mention my thanks to MIT for providing an intellectual environment to pursue graduate studies. Over the years I have spent here, I have learnt to think and act maturely (I think!). I have been lucky to have had Srini as my advisor. He welcomed a new line of research in the lab, provided me with the independence to pursue ideas, and also provided useful and insightful solutions at many critical junctures. On several occasions he was able to overcome what seemed to me like very difficult situations. The friendly and informal atmosphere he provides in the lab lets everyone perform his or her best. Thanks to Denny Freeman for co-supervising this thesis. He has always been very supportive, and I have learnt a good deal on proper research methods from him. I was fortunate to have Tim Stanton on my thesis committee. From Tim I learnt the wonderful field of acoustic scattering, first from his course, and later through numerous individual discussions. In particular I will remember all my visits to the Woods Hole Oceanographic Institution, from where I would return more confident and knowledgeable each time. I also thank Art Baggeroer for serving on the thesis committee, and for believing from the beginning that I was capable of doing important work.

The collaboration with the Wellman Labs at MGH is gratefully acknowledged. I am grateful to Salvador Gonzalez for providing the much needed clinical collaboration for this project. I am glad to have known Kirsty Swindells, and I thank her for scheduling the patients, answering my numerous questions on patch-testing, and providing good friendship. Thanks to Rox Anderson for his help in setting up the clinical collaboration, and for providing space at the Wellman Labs to set up the ultrasound system. Thanks to Bill Farinelli for his help in re-arranging Room 304 and in setting up the system. Also to Nadine Burnet and Susanne Astner for the added laughter in

Room 304, and Sarita Nori for her enthusiasm, and to Martine Sifakis for her help in the administrative aspects.

Several subjects volunteered their time for the study. They have indeed made this research possible, and I thank them for their participation.

I am thankful to Suiren Wan for his help in transporting the ultrasound device to MGH, in testing and setting up the system, and for providing some late night discussions on the project during the last year. I would like to add my thanks to Abraham Cohn (UM, Ann Arbor), who in the initial stages helped me to learn the field of ultrasound by answering all my questions promptly and clearly. I will always be grateful for his help. And to Alan Coulson for sending me his thesis from New Zealand and clarifying some issues regarding the Generalized Gamma distribution. And to Karl Thiele and others at Agilent, for giving me the opportunity to work on an exciting summer project in 1999. During that period, I enhanced my general understanding of ultrasound, learnt to simulate acoustic wave propagation, and learnt a few Matlab tricks that were later useful in this thesis work. I would also like to add my thanks to Peter Morley and the MIT Central Machine Shop, who made it very easy to design and machine parts for the ultrasound system.

I owe a good deal of thanks to all my lab-mates, both past and present. The list is numerous. They have made the lab a wonderful place to work. I also thank the other floor-mates in the CBG group, some of whose friendship I have had the fortune to enjoy. The list of friends outside the lab is also numerous. Thanks to Manish Kothari and Suryaprakash Ganti for their help in welcoming me to Boston when I first came to MIT. I fondly remember the weekend get-togethers with Srikanth Samavedam, Ram Ratnagiri, Srikanth Vedantam, Jyotsana Iyer, Satyan Coorg and others. My roommates, from Ronan in the first year to Sumathy in the last year, have made living in Cambridge a positive experience. I thank them all.

And thanks to my fiancée Rajeswari, for her patience, consideration and encouragement during the final stages of this work. I look forward to sharing my life with her. And to my sister and my parents, who believed in me, and often put my interests ahead of theirs. Their love and support has made this possible.

The work reported here was funded by NIH grant NS33778 and by a Grant-in-Aid of Research from the National Academy of Sciences through Sigma Xi.

Contents

List of Figures

List of Tables

1 Introduction

This thesis is concerned with the development of quantitative methods to characterize human skin tissues in vivo using high frequency ultrasound. This chapter explains the need for non-invasive imaging of skin tissues, describes the suitability of high-frequency ultrasound for imaging skin tissues, and explains the importance of ultrasonic tissue characterization methods in evaluating skin tissues. It also provides a brief survey of ultrasonic tissue characterization methods and previous work on ultrasonic evaluation of skin. The chapter concludes with a note on thesis organization.

1.1 Need for non-invasive imaging of skin tissues

Non-invasive imaging of skin has several applications in dermatology. These include determination of tumor margins prior to surgery, tumor staging, evaluation of non-tumorous skin lesions such as scleroderma, psoriasis, and contact dermatitis, determination of the depth of thermal burn injuries, studying the effects of photoaging, studying the effects of nuclear radiation on skin etc. An accurate diagnosis of suspected skin lesions often requires skin biopsies and subsequent histological evaluation of the biopsy slides. Skin biopsies are minor surgical procedures that require sectioning and staining, are time-consuming, and also have associated morbidity (pain, local anesthesia, and scarring). In many cases, biopsies turn out to be unnecessary as a majority of skin lesions are non-tumorous. Hence it is conceivable that at least in some of the cases, non-invasive imaging of suspected skin lesions could provide information on the nature of the skin lesions so that biopsies are done only in cases that require them.

Non-invasive imaging of skin is also useful when biopsies are determined to be necessary, as in the case of lesions diagnosed to be skin cancer. Types of skin cancer include malignant melanoma, the fastest growing cancer in the US [1], and non-melanoma cancers such as basal cell and squamous cell carcinomas, which represent the most commonly occurring malignancy in humans [2]. The incidence of malignant melanoma, the most serious form of skin cancer, has almost tripled in the past 4 decades, making it the fastest growing cancer in the United States. About 32,000 melanoma cases are reported each year, and 6,500 cases are fatal. No significant change in diagnosis can be attributed to this increase [3]. About 600,000 non-melanoma cancer

cases are reported each year in the United States. The primary form of treatment for all skin cancer cases is a surgical removal of the tumor. However the boundaries of the tumors are not always obvious to the surgeon at the time of surgery. This is because tumors could spread beneath the surface, and their extent may not be visually obvious. Because of this, the general practice is to excise the affected skin areas with wide margins around the tumor, check with histology if the borders are free of tumor, and repeat surgery if more tissue removal is needed. Such an iterative procedure is both time-consuming and expensive. It is therefore very advantageous to have non-invasive imaging methods that could provide information on the extent of the area of skin that needs to be biopsied. Non-invasive imaging of skin cancer is also useful in determining the thickness of the tumor, which is the single most important indicator of the stage of the disease. An additional advantage with non-invasive imaging is that unlike in the case of biopsies, tissues can be examined repeatedly over a period of time. Thus non-invasive imaging can be used for determining the patient's response to chemotherapy and determining the recurrence of tumor. Thus non-invasive imaging methods could play a significant role in the treatment and management of skin cancer.

Evaluation of thermal burn injuries is another important application of non-invasive skin imaging. According to a recent White House report, each year over 3,000 people die and 16,000 are injured in the US by residential fires alone [4]. Burn injuries are graded as first degree burns (only epidermal skin damage), second degree burns (partial thickness damage), or third degree burns (full thickness damage). While first degree burns are considered to be minor and do not require extensive treatment, deep second degree and third degree burns require skin grafting. The treatment for burn injuries is determined by the depth of tissue damage. However it is often difficult to determine the depth of burn injuries through visual examination alone, especially for the case of second degree burns. Therefore in many cases it is difficult to decide whether skin grafting is required or not. In such cases a non-invasive imaging tool that can determine the depth of the thermal injury is very useful in planning the treatment.

Another application of non-invasive skin imaging is the evaluation of cutaneous radiation fibrosis, which is the thickening of the skin due to exposure to nuclear radiation [5]. For instance an ultrasound study of the skin of survivors of the 1986 Chernobyl nuclear accident six years after the accident showed a significant increase in thickness [6]. Other applications of skin imaging include photoaging studies where the changes in skin due to sun damage can be evaluated, evaluation of the effects of cosmetics on skin, and evaluation of laser resurfacing treatments. Also

non-tumorous lesions such as contact dermatitis could be studied non-invasively. Specifically the increase in skin thickness and alterations to the dermis could be studied and related to the degree of the allergic or irritant reactions.

There are also other non-clinical applications for skin imaging. These include studies on human tactile sensing that attempt to relate mechanical loads on the skin surface to neural responses transmitted to the brain [7, 8]. While much is known about the way the human vision and auditory systems work, comparatively little is known about the way human touch works. Just as light intensity triggers neural responses from retinal cells, mechanical strains trigger responses from the mechanoreceptors in skin. Using elastographic techniques [9] imaging of skin could be used to determine these mechanical strains. These mechanical strains could be then related to recorded neural discharge rates from afferent nerve fibers. Imaging could also provide details of fine structures and layers in the skin, which can then be used to develop finite element models. These models can also be used to numerically compute strain fields near the nerve endings due to prescribed mechanical loads on the skin surface, thus obviating the need for experiments. By combining strain imaging and numerical simulations, it might also be possible to determine mechanical properties of skin tissues such as Young's Modulus and Poisson's ratio of various skin layers.

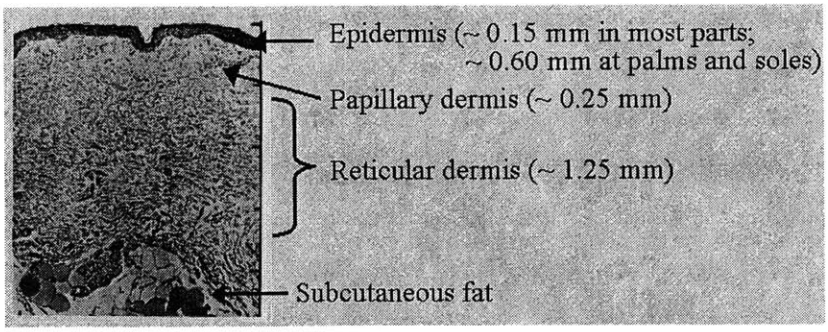

Figure 1.1:Cross-sectional histological image of human skin. Figure adapted from Odland [10].

1.2 Need for high frequency ultrasound

Having described the importance of non-invasive evaluation of skin, we now explain the suitability of high-frequency ultrasound for imaging skin tissues. Selection of a suitable technique for imaging skin is determined primarily by the physical dimensions of skin tissues and the level of resolution required. Skin consists of a superficial layer of epidermis (0.15 mm thick in most

parts) and an underlying layer of dermis (1.2–1.8 mm thick). The total skin thickness in most parts of the body is typically less than 2 mm except at the palms and soles where it is thicker. The dermis consists of an upper layer called papillary dermis and a deeper layer called reticular dermis. The region beneath the reticular dermis consists of subcutaneous fat, which is sometimes considered to be a third layer of the skin and is also referred to as the hypodermis (Fig. 1.1). When affected by certain conditions, e.g., psoriasis or contact dermatitis, the skin thickness could increase significantly. This implies that the imaging technique should be capable of imaging tissues up to a depth of several mm, say a maximum of 5 mm. The next requirement is that the resolution of the device must be small enough, on the order of tens of microns, to differentiate sub-layers within the skin and to identify and isolate pathologies within the skin. This is especially important for evaluating early stage malignant melanoma, where an accurate determination of the tumor thickness is important. Commonly available imaging techniques such as MRI, x-ray, and conventional ultrasound (operating at frequencies in the range 1-10 MHz) are generally used for imaging either the full thickness of human body or for imaging tissues that lie deep within the body (10 cm). The resolution provided by these modalities is about 1 mm, and hence they are not suitable for imaging skin. Confocal microscopy, a technique that uses optical reflections from tissues, is a promising technique for imaging superficial skin tissues because of its high resolution (~ microns) enabling visualization of details at a cellular level [11, 12]. However the technique is limited to imaging only superficial tissues (~ 0.35 mm) and not the full thickness of the skin. Another limitation with this technique is that it can provide only horizontal scans of the tissue. This is disadvantageous in cases where vertical sections of skin tissues are needed, e.g., to determine the thickness of a skin lesion. Optical coherence tomography [13, 14], another technique that uses optical backscatter from tissues to vertical sections, is also a promising technique for imaging skin, but has limited penetration in skin (~ 1 mm). Hence it is less suited for imaging deep skin tissues.

One method that can image the full thickness of skin and provide the required level of resolution is high-frequency ultrasound. High-frequency ultrasound is similar to conventional ultrasound (1-10 MHz) but uses much shorter pulses having higher center frequencies. The shorter pulse length leads to an improvement in the axial (along the beam propagation) resolution and the higher frequency leads to better lateral (perpendicular to the beam propagation) resolution. At a typical frequency of 50 MHz, both the axial and lateral resolutions are on the order of tens of microns, with the former being smaller in general. The depth of penetration is about 5 mm, which is smaller than of conventional ultrasound, but is sufficient enough to image skin tissues. Besides

satisfying the resolution and imaging depth requirements, high-frequency ultrasound poses no known risks unlike methods that rely on ionizing radiation. Additionally high-frequency ultrasound systems could be modified with relative ease to achieving a trade-off between resolution and penetration depth. For instance, it is easy to replace a 50 MHz transducer with a 100 MHz one and image only the epidermis at a lateral resolution of less than 15 μm. High frequency ultrasound also complements optical techniques such as confocal microscopy in that it provides full thickness information at a comparatively lower resolution whereas confocal microscopy provides information at a very high resolution but only of superficial tissues. Finally high-frequency ultrasound systems are also inexpensive compared to most other imaging modalities including conventional ultrasound systems.

1.3 Need for ultrasonic tissue characterization methods

Having described the potential of high-frequency ultrasound in imaging skin, we now describe the need for quantitative ultrasonic methods to characterize skin tissues. Ultrasound images are created by detecting the envelope of the backscattered echoes from the tissues and mapping the envelope into gray levels for display. These images, commonly referred to as B-scans are essentially maps of the envelope of backscatter echoes from different parts of the tissue. The envelope represents only partial information present in the echoes as information such as the frequency dependence of backscatter amplitude or of phase is lost during its computation. Since the primary tissue-wave mechanism responsible for backscattered echoes is diffuse backscattering, the backscattered echoes depend on the size, shape, material properties, and number density of scatterers distributed in the tissue. These scatterers are basically discontinuities in the acoustical properties in the tissue and in the case of skin could be collagen fibers in the dermis, keratinocyte cells in the epidermis, groups of cells or fibers, sub-cellular components or sub-fibrous components. It is conceivable therefore that by analyzing the backscattered echoes, more quantitative information about the tissue and scatterers could be extracted for characterizing and classifying tissues. Another problem with ultrasound images is that identification of tissue structures in the images relies on subjective interpretation of features, which are also highly dependent on operator settings and display conditions. Subjective interpretation is oftentimes difficult due to the presence of speckle in ultrasound scans, which results from the interference of waves scattered from scatterers lying within the resolution cell. Thus quantitative methods might have the potential to reduce ambiguity in inferring tissue features. These quantitative methods are commonly referred to as *tissue characterization methods*.

In the case of skin tissues, the need for tissue characterization studies is evident from earlier studies that have shown the limitations with conventional B-scan imaging. For example it is known that using only B-scans it is difficult to distinguish between benign and malignant lesions [15], between different types of skin tumors [15, 16], between melanoma and an old scar [17], or between tumors and sub-tumoral inflammatory infiltrate [18]. The reason for this is that the gray levels in the images could not always be definitively correlated with any specific type of tissue. For instance all tumors generally appear hypoechoic with respect to normal dermal tissue without any difference among their different types. Thus it is worthwhile to pursue quantitative tissue characterization methods that might, using additional features, be able to classify and differentiate various skin lesions. For example structural changes in skin due to changes in pathology (e.g. infiltration of dermal collagen fibers by tumor cells) could result in changes in ultrasonic properties that are registered by these methods.

Interestingly, dermatologists who have used 20 MHz ultrasound systems to image skin have already investigated the possibility of extracting quantitative features from images to augment information seen in the ultrasound images. For example in studies of contact dermatitis, ultrasonic parameters such as the mean echogenicity values and the number of low-intensity pixels have been used to relate them to the degree of the allergic or irritant reaction [19]. In photoaging studies, the mean echogenicity values have been used to relate to the level of sun damage [20]. Although these parameters are not based rigorously on the physics of wave-tissue interaction, they have shown to be able to add to information available from B-scan images. Hence it is apparent that even practicing dermatologists have found the need and use for extracting additional quantitative features from ultrasonic scans of skin tissues, thus corroborating the importance and need for tissue characterization methods in studying skin.

A very brief survey of various tissue characterization methods and ultrasonic parameters is now presented. The simplest parameter is the speed of sound in the tissue. However this parameter cannot be computed for in vivo tissues using pulse echo techniques with single element transducers. Commonly, the speed of sound is assumed to be some particular value, e.g., 1.5 mm/μs [21], as little variation is seen across soft tissues and across a variety of frequencies. Another parameter that could be inferred from signals backscattered from tissues is the attenuation coefficient. This quantity is the loss in signal amplitude with propagation distance, for any frequency component in a pulsed wave. It is expressed in units of dB/mm, as it is commonly assumed that the wave decays exponentially with distance [22]. Another parameter is the

backscatter coefficient, which is defined as the differential scattering cross-section per unit volume of tissue at an angle of 180 degrees [23]. This quantity directly determines the brightness of pixels in B-scan images. Moreover, if a wide bandwidth pulse is used, then the frequency dependence of both the attenuation and backscatter coefficients can be used as quantitative parameters to characterize tissues. With pulse-echo techniques, the recorded signal at a particular depth within the tissue depends on both the attenuation and backscatter coefficient, and therefore both the quantities cannot be inferred from a single set of measurements (taken over several depths within the tissue). This problem is circumvented by assuming that the region of interest (ROI) is homogeneous and consists of the same tissue, and therefore the backscatter coefficients are the same at all the depths within the ROI. This assumption thus leads us to infer both the attenuation and backscatter coefficients from a single set of measurements. Another possible parameter that can be extracted is the mean scatterer size, which can be estimated once the frequency dependence of backscatter coefficient is known. The extraction of the above parameters requires compensation for the characteristics of the imaging system, as the backscattered echoes depend not only on the tissue being insonified but also on the imaging system characteristics. Theoretical developments for computing the above parameters including compensation for system dependent effects, and tests on tissue-mimicking phantoms have been presented by several earlier researchers [24-32]. These methods are also well described in the book by Shung and Thieme [33].

Another method for tissue characterization uses the fact that ultrasonic signals can be modeled as stochastic signals since the precise details of the scattering structures in tissues, and consequently the details of the backscattered signals, are not known a priori [34, 35]. The backscattered echo is modeled as a random process and the statistical fluctuations (probability density functions) of this process depend primarily on the number density of the scatterers relative to the wavelength as well as spatial heterogeneity within the tissue. The number density has been used as a parameter for characterizing tissues [36-42]. The theoretical background for the above methods was obtained from work done in other fields such as statistical optics, radar and communications [43-47].

Using one or more of the above methods, several tissues have been studied: the heart [48, 49], blood [50], liver [51-54], eye [55-57], kidney [58, 59], spleen [60], breast [38, 61], tendon [62, 63], atherosclerotic plaques [64, 65], lung [66, 67], and skeletal muscle [68]. Skin tissues on the other hand have not been studied well using ultrasonic tissue characterization methods. For the

sake of completion we also mention other parameters that have been explored in the literature. These include mechanical strain imaging (elastography [9, 69]), and nonlinear ultrasonic parameters such as the B/A measure [70].

1.4 Previous studies on ultrasonic skin imaging and characterization

Previous work on ultrasonic imaging of skin has mostly involved 20 MHz systems. Examples of such works include evaluation of tumors [15, 18, 71, 72], scleroderma [73], psoriasis [74, 75], burn injuries [76], contact dermatitis [19], radiation fibrosis [6], photoaging [20, 77] and study of the effects of cosmetics [78]. Systems operating at frequencies greater than 20 MHz have also been demonstrated [79, 80]. The B-scan images of skin produced by such systems have shown that fine structures such as veins and hair follicles can be visualized [17, 81]. Ultrasonic skin characterization is a relatively new field and there are very few studies that report on the ultrasonic properties of skin or utilize tissue characterization techniques for classifying skin tissues. Most of these studies are also based on excised skin tissues, and not in vivo tissues. Of the studies that have been done so far, Olerud et al [82] showed that both speed and attenuation in skin were directly related to collagen content and inversely related to water content. Riederer-Henderson et al [83] measured attenuation and speed in excised normal canine skin at 25 and 100 MHz using backscatter techniques and Scanning Laser Acoustic Microscopy (SLAM) respectively. Using backscatter and SLAM techniques respectively, Forster et al [84] and Olerud et al [85] found that the speed and attenuation values for wounded canine skin were less than that of control skin. Moran et al [21] measured speed, attenuation and backscatter coefficients from excised human skin tissues between 20-30 MHz. Baldeweck et al [86] measured attenuation coefficient of excised porcine skin tissues at 20 MHz. Pan et al [87] measured attenuation and backscatter coefficients in excised rabbit and human skin between 20-30 MHz and found a decreasing trend in attenuation coefficient and a slight increasing trend in backscatter coefficient with increasing strain. Guittet et al [88] measured attenuation at 40 MHz for 150 human volunteers in vivo using a spectral-shift technique and found a decreasing trend in attenuation coefficient slope with age.

1.5 Goals of this thesis and thesis organization

This thesis is concerned with developing quantitative tissue characterization methods for skin tissues using high frequency ultrasound. Three different measures will be studied: the attenuation coefficient, the backscatter coefficient, and parameters related to echo statistics. The fact that these three measures form a related set can be easily seen. The attenuation coefficient is a

measure of mean decay rate of ultrasound with propagation distance in the tissue, the backscatter coefficient is a measure of the mean inherent backscatter from the tissue, and echo statistical parameters measure the statistical fluctuations in the backscatter from the tissue. These parameters are first studied in normal skin tissues in vivo. We also emphasize that unlike most of the previous studies, this study utilizes in vivo human skin tissues rather than in excised tissues. In order for tissue characterization methods to be clinically useful, the studies should be done under in vivo conditions. The properties of in vitro tissues could differ significantly from that of in vivo tissues due to reasons such as changes in skin tension, absence of blood flow, differences between room and body temperatures (when specimens are tested at room temperature), and specimen preparation effects. After normal skin is studied, a clinical example, characterization of contact dermatitis skin, is presented.

Chapter 2 describes the development of the high-frequency ultrasound systems used in this work. Three systems with increasing complexity in design are described. Examples of in vivo skin images are also shown.

In Chapter 3, the computation of attenuation and backscatter coefficients from normal human skin tissues in vivo is described. This chapter makes several contributions. Until now, backscatter coefficients of skin tissues have not been measured under in vivo conditions, and in vitro measurements of backscatter coefficients are very few. Diffuse backscattering is the primary soft tissue-wave interaction responsible for echoes received at the transducer, and hence, for any images that are generated with ultrasound systems. The backscattered signals depend on the size, shape, material properties, and orientation and concentration of scatterers (discontinuities in acoustic properties) in the tissue and could contain potential information about tissue microstructure especially when a broad range of frequencies is available. Therefore measurements of in vivo backscatter coefficients will serve to improve our basic understanding of ultrasound-skin tissue interaction. Another contribution of this chapter is the study of attenuation and backscatter coefficients of subcutaneous fat, which is sometimes considered as a third layer of skin and referred to as the hypodermis. Based on B-scan images, subcutaneous fat is considered hypoechogenic with respect to dermis, but such a difference has not been quantified in terms of integrated backscatter measurements or frequency dependence of backscatter coefficients. It is necessary to study subcutaneous fat because skin lesions such as tumors could extend well beneath the dermis into the fat [1]. Previous studies have indicated that in B-scan images, both subcutaneous fat and skin tumors appear hypoechogenic with respect to the dermis

and therefore there could be ambiguity in determining the bottom margins of thick tumors that extend beneath the dermis into the fat. Chapter 3 also studies whether ultrasonic properties of skin tissues could vary from one location to another. Unlike other organs like the heart, liver etc. that are localized to one region in the body, the skin covers the entire body and large variations in properties are possible because of differences in skin thickness and type (e.g. glabrous vs. hairy skin), the state of tension, exposure to sun and environment, as well as work-related usage of certain parts of the body. By recording data from two grossly different regions in the body, the fingertip and the dorsal forearm, the attenuation coefficients of the dermis at these two locations are compared.

In Chapter 4, the echo statistics of backscattered signals from normal human skin tissues are studied. Until now, the statistical distributions of the envelope of backscattered signals from skin tissues have not been studied. The type of probability distribution of the envelope signals, and their parameters, could contain potential information regarding tissue microstructure that could be exploited for tissue characterization. The capability of six different probability distributions (Rayleigh, Rician, K, Nakagami, Weibull, and Generalized Gamma) to model statistics of envelope of backscattered data collected from the skin of several human volunteers in vivo is studied using the Kolmogorov-Smirnov (KS) statistic as a goodness of fit measure. Although a recent independent work has also proposed the use of the Generalized Gamma distribution in ultrasonic tissue characterization [89], this chapter reports the first attempt to fit empirical ultrasonic backscatter data using the Generalized Gamma distribution for *any* tissue. The variability in parameter estimates and a comparison of the inter- and intra-subject variability are studied. This is important as a large variability in the estimates might limit the capability of the parameters for tissue characterization and methods to reduce such variability should be pursued. Finally the capability of the parameters to differentiate different normal skin tissues (dermis vs. fat, forearm dermis vs. fingertip dermis) is also studied.

Chapter 5 describes a clinical application of the tissue characterization methods. Contact dermatitis, a common inflammatory condition of the skin, is used as an example. The attenuation coefficient, mean backscatter amplitude, and parameters related to echo statistics are computed for the skin lesions and compared with those of normal tissues.

Chapter 6 summarizes the contributions of this work and suggests topics for future work.

A final note about the thesis is in order. Because some of the chapters (3, 4 and 5) were written as separate manuscripts for publication in journals, some discontinuity between the chapters is inevitable. Also for the same reason, some amount of repetition is unavoidable. Such an organization of the thesis with each chapter having some independency of its own will also benefit the reader who wishes to read only a portion of the thesis.

2 System Design

This chapter describes the development of the high-frequency ultrasound imaging systems used in this work. The need for a custom-designed system was based on several reasons. Commercial ultrasound systems operating at frequencies higher than 20 MHz are not commonly available. Moreover, commercial systems have several limitations when it comes to characterization of tissues. For instance in tissue characterization studies, the raw backscatter signals are needed and not just the final images. If raw signals are not available, then all the details of the signal path must be known. If there are nonlinear transformations in the signal path (e.g. signal compression), then the effects of these nonlinearities must be incorporated in the analysis, which is not generally straightforward. Another difficulty is that commercial systems lack flexibility that is needed in tissue characterization studies. For instance, it may not be possible to minimize diffraction effects through axial scanning, or correction curves may not be available to compensate for diffraction correction. Hence it was decided to build a custom-designed system as a research platform in the laboratory. Three systems with increasing complexity and functionality were constructed.

At high frequencies, phased array transducers are not yet available and hence a single element transducer needs to be mechanically scanned over the tissue in order to collect echo signals from various locations. Such a system requires, apart from the transducer, a scanning system to position the transducer, a pulser to excite the transducer, a digitizer to collect the backscattered echoes, and a PC to control the various elements. The first system built was a simple manually scanned system to demonstrate the concept of high frequency ultrasonic imaging of skin tissues. The second system incorporated computer controlled scanning to automate the transducer positioning. The total imaging time for this system was too large due to limitations in the data transfer rate, which made it unsuitable in a clinical environment. The third system was an improved version of the second system with capability to scan at much faster rates. At the heart of all these systems is the transducer that generates the acoustic waves and collects the backscattered echoes. Three different transducers were obtained from Panametrics Inc. (Waltham, MA). A description of these transducers is first presented, after which the three systems are described.

2.1 Transducer characteristics

The ultrasonic transducer works on the principle of piezoelectricity. Application of a high-voltage pulse leads to the generation of acoustic waves. The transducer also receives the backscattered echoes from the tissues and converts them into electrical signals. The quality of the backscattered echoes, and consequently the images, are primarily determined by the properties of the transducer. Among different transducers made of different piezoelectric materials, it was found that ones made of Polyvinylidene Diflouride (PVDF) polymer were good for the purpose of skin imaging. The acoustic impedance of PVDF matches that of water, which leads to effective coupling when water is used as the medium between the transducer and tissue. Commercially available polymer transducers also have large bandwidths and have less noise than those made of other materials such as Lead zirconate titanate (PZT). The axial (along the direction of wave propagation) resolution of the system is determined by the length of the acoustic pulse generated by the transducer, and the speed of sound in the medium:

$$\Delta z = \frac{cT}{2} \cong \frac{c}{2(BW)} \tag{2.1}$$

where c is the speed of sound, T is the pulse length, and BW is the inverse bandwidth of the pulse. For roundtrip measurements, it is common to use the –6 dB points as a measure of the bandwidth. The lateral (perpendicular to the wave propagation) resolution is determined by the wavelength of the sound in the medium and the f-number of the transducer:

$$\Delta x = F\lambda = \frac{Fc}{f} \tag{2.2}$$

where F is the f-number of the transducer, λ is the wavelength of the wave, and f is the frequency corresponding to the wavelength. In cases such as medical ultrasound where a pulsed wave is used, it is common to use the center frequency as an indicator of the frequency of the wave. The depth of focus, or the distance over which the wave stays approximately focused is determined once again by the wavelength and the f-number. The –6 dB depth of focus for round-trip measurements is given by [90]:

$$DOF(\text{-6 dB}) = 7.1\lambda F^2 \tag{2.3}$$

Hence, from the above equations it is clear that the frequency characteristics of the transducer are important in determining the characteristics of the imaging system. The axial and lateral resolutions, besides determining the quality of B-scan images, are important quantities in tissue characterization studies. For instance, in computing attenuation and backscatter coefficients, the

average of power spectra from adjacent independent lateral locations must be computed. The lateral resolution determines how far the transducer should be moved laterally in order to record independent echoes. The axial resolution determines the distance along an echo line required for independence. Independent samples are needed in creating empirical histograms of backscatter fluctuations, and subsequently computing echo statistics parameters. The depth-of-focus is also an important quantity as it provides an indication of the extent over which any features can change appreciably purely due to diffraction effects rather than due to features of the tissue being studied.

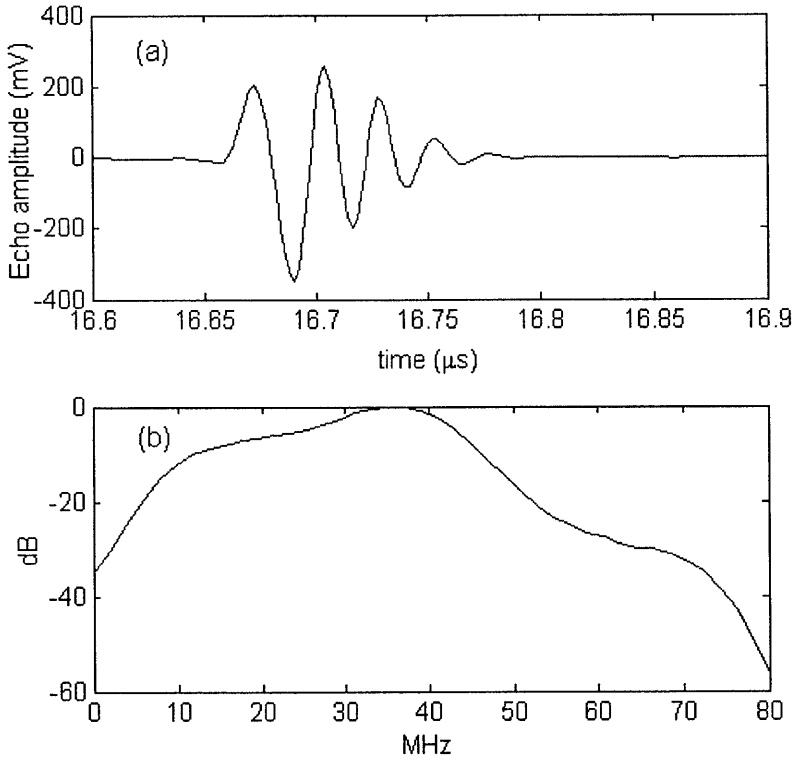

Figure 2.1: (a) Echo reflected from a plane reflector at the focus of the PI50 transducer for an energy setting=4 μJ (b) Frequency spectrum of the corresponding pulse. See also Table 2.1.

The three transducers used in this work had nominal frequency ratings of 50, 75 and 100 MHz. Although the transducers were made to operate at the above frequencies, the actual center frequency is typically lower, possibly due to attenuation in the coupling fluid over a distance of twice the focal length. It was also seen that the excitation energy setting in the pulser changes the frequency of the pulse to some extent. With increasing level of excitation, the center frequency of the transducer was found to decrease due to the inherent characteristics of the pulser. Changing

the excitation level thus leads to a trade-off in the penetration depth and system resolution. With a higher energy setting, the echoes also remain above the noise level for a deeper distance, thereby increasing penetration depth. The downside is the loss in system resolution. The combination of transducers and the energy of excitation, and the resulting properties of the transducers are shown in Table 2.1. These settings were decided mostly by trial and error, with the larger excitation level used for tissue characterization studies and the lower excitation level used for clinical applications that needed both imaging and characterization.

Figure 2.1 shows the echo of the signal reflected by a planar interface placed at the focus for the case of the PI50 transducer for an excitation level of 4 uJ. Also shown is the frequency spectrum of the pulse. The center frequency, taken to be the mean of the –6 dB points, was computed to be 33 MHz, and the –6dB bandwidth was computed to be 28 MHz. In order to determine the depth of focus of the transducer, several echoes were recorded when the reflector was placed at different distances from the transducer. Figure 2.2 shows the recorded pulses. The –6 dB depth of focus was computed to be 1.03 mm.

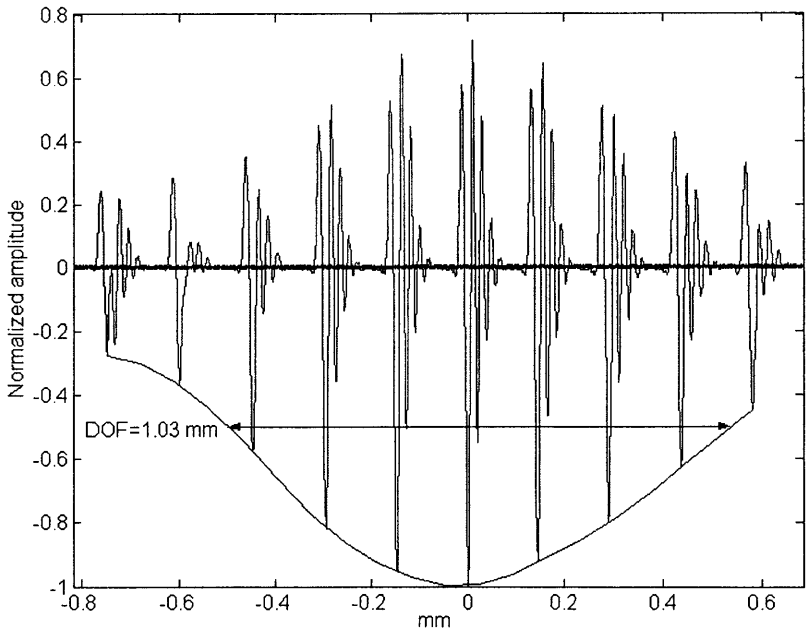

Figure 2.2:Experimental determination of the depth of focus of the PI50 transducer for an energy setting of 4 μJ.

2.2 System I: Manually scanned system

In order to demonstrate the capability of high frequency ultrasound to image skin tissues, a simple manually scanned system was first developed. This system was easy to implement and is described in detail in a previous work [91] and is shown in Fig 2.3. . It consisted of the PI75 polymer transducer, a pulser (Panametrics, Model PR5900), a digitizing oscilloscope (Tektronix, Beaverton, OR; Model TDS 520C), and a high-precision manually scanned 2-axis positioning system (Parker Hannafin/Compumotor, Cleveland, OH). The digitizing oscilloscope sampled the backscattered signals from the tissue at a sampling frequency of 500 MHz. A low pass filter with a cut off frequency of 200 MHz was selected on the receiver portion of the pulser. The transducer was mounted on the scanning system that had a horizontal positioning accuracy of 2 μm. Since the transducer was broadly focused (f/#=4, DOF=5.1 mm), diffraction effects (beam amplitude variations due to the focusing characteristics of the transducer) were minimal in this case and a single echo at every lateral location of the transducer was considered sufficient to create images. Each echo sequence was an average of 100 repeated waveforms obtained at the same location, which vastly improved the signal-to-noise ratio of the echoes. Qualitative evaluation of the system was performed using tissue-mimicking phantoms with various densities of scatterers. Images of human skin in vivo showed the separation between dermis and fat and fingerprints on the surface of a fingertip skin.

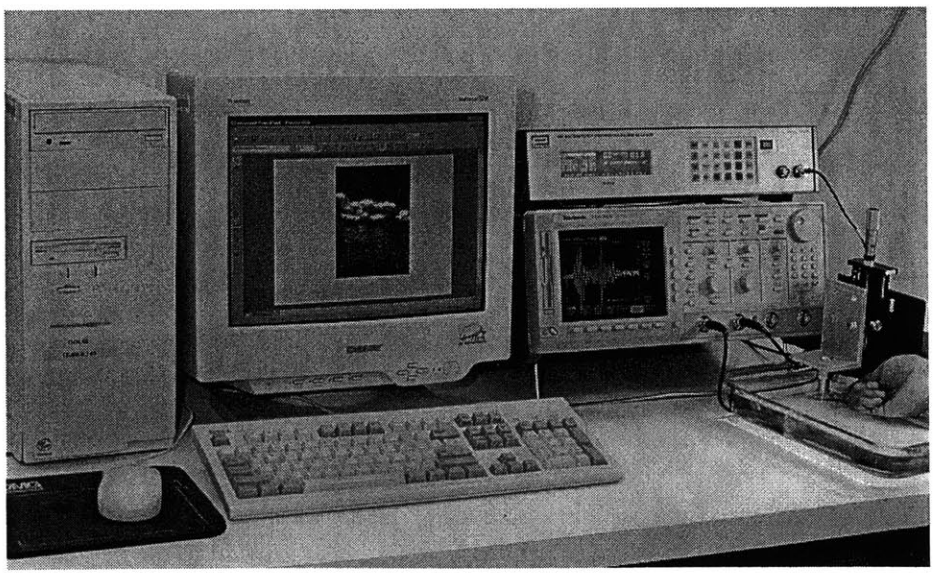

Figure 2.3:Experimental setup of the manually scanned system.

Table 2.1: Properties of the transducers used in this work. The numbers in the first row next to the transducer model numbers indicate the energy setting in the pulser.

Transducer	PI50, 32 μJ	PI50, 4 μJ	PI75, 32 μJ	PI3005, 16 μJ
Center frequency	28 MHz	33 MHz	30 MHz	44 MHz
- 6 dB bandwidth	30 MHz	28 MHz	40 MHz	50 MHz
F-number	2	2	4	2
Diameter	6.35 mm	6.35 mm	3.175 mm	2 mm
Focal length	12.7 mm	12.7 mm	12.7 mm	4.58 mm
-6 dB depth-of-focus	1.3 mm	1.03 mm	5.1 mm	1.27 mm
Axial resolution	25 um	27 um	19 um	15 um
Lateral resolution	107 um	83 um	200 um	68 um

2.3 System II: Computer-controlled scanning system[1]

Once the basic concept of a high frequency imaging system was demonstrated using the manually scanned system, computer-controlled motorized positioning was included to automate scanning. Figure 2.4 shows a schematic of the setup and a picture of the system while data were being collected from a subject's fingertip in vivo. The transducer was mounted on a 3-axis stage that had precision-grade slide assemblies for each of the axes (Parker Hannafin, model number 402006LNMP). The total travel length was 6 inches on each of the axes, and the positioning accuracy and repeatability were 12 μm and 2 μm over the total travel length. Motors (Model number Zeta57-51) attached to the three axes were powered using micro-stepping drives (Model number Zeta4). Encoders were used on the x and y-axes to provide a high lateral positioning accuracy of 1 μm. The drives were controlled a 4-axis controller (Model AT6400), which received commands from the PC through an ISA interface card. Custom programs were developed in a Visual C++ environment to facilitate computer control. The transducer was attached to the scanning system using a manually operated rotary stage and a custom machined bracket. A joystick was used to facilitate initial positioning of the transducer at the start of the experiment. As in the previous system, each echo line was an average of several repeated acquisitions (100 for transducers I and II, and 240 for transducer III), which greatly improved the

[1] This section contains material excerpted from an article published in Ultrasound in Medicine and Biology [92].

signal-to-noise ratio, enabling even weak signals from subcutaneous fat to be studied. An example of the importance of averaging is shown in the next section which describes System III.

All tissue characterization studies described in Chapters 3 and 4 were performed using this system. To facilitate the data acquisition procedure, many other features were added to the system. One such feature was that while recording each echo line, the vertical scale on the digitizing oscilloscope was adjusted in real-time by the controlling program in order to record strong signals like surface reflections free of clipping, as well as weak signals like backscatter from subcutaneous fat without quantization effects. For example, when a full scale of –5 to +5 volts is set, a weak signal with amplitude of only 25 mV might get quantized to a value of zero, because of the finite number of bits. On the other extreme, if the full scale is too low, say –5 mV to + 5mV, the same signal would be recorded with clipping effects. Since there is no a priori way to know the magnitude of signals to be recorded, the software adjusts the scaling on the vertical axis (by trial and error) for each echo sequence to ensure that the signals are being recorded without serious degradation due to quantization effects as well as without clipping. Another feature was that several axial scans were used to combine data collected from different depths in the tissue, so as to minimize diffraction effects. Although such a technique has been used before [79], the present system could adaptively adjust the height of the transducer above the skin surface for every lateral location. Such a procedure was important in tissue characterization studies due to the curvature of the skin. As shown in Fig. 2.5, because of the skin curvature, data from adjacent locations of the focal zones for any given axial location of the transducer could correspond to different depths from the surface when the transducer is rectilinearly scanned across the tissue. In some cases the location of the focal zone might even move out of the surface. This is undesirable when lateral averaging of quantities like power spectra are done. Hence at each lateral location of the transducer, the system first adjusted for the surface curvature by measuring the time-of-flight from the surface and then moved the transducer up or down, so that the surface was at a pre-determined distance from the transducer. Such adjustments still have the problem of oblique incidence due to surface curvature, i.e., the incident angle not being 90^{o}. However since the interaction of waves with the tissues is more of scattering rather than specular reflections, the effect of oblique incidence should be small as long as the incident angle is not very different from 90^{o} [52]. Scanning was first done in the axial direction to collect data from several locations of the focal zones in the tissue for a given lateral location, after which the transducer was moved to the next lateral location, its height adjusted, the axial scans done, and

the procedure repeated for all lateral locations. Scanning was thus done in discrete steps, with the transducer moved and stopped at the appropriate locations.

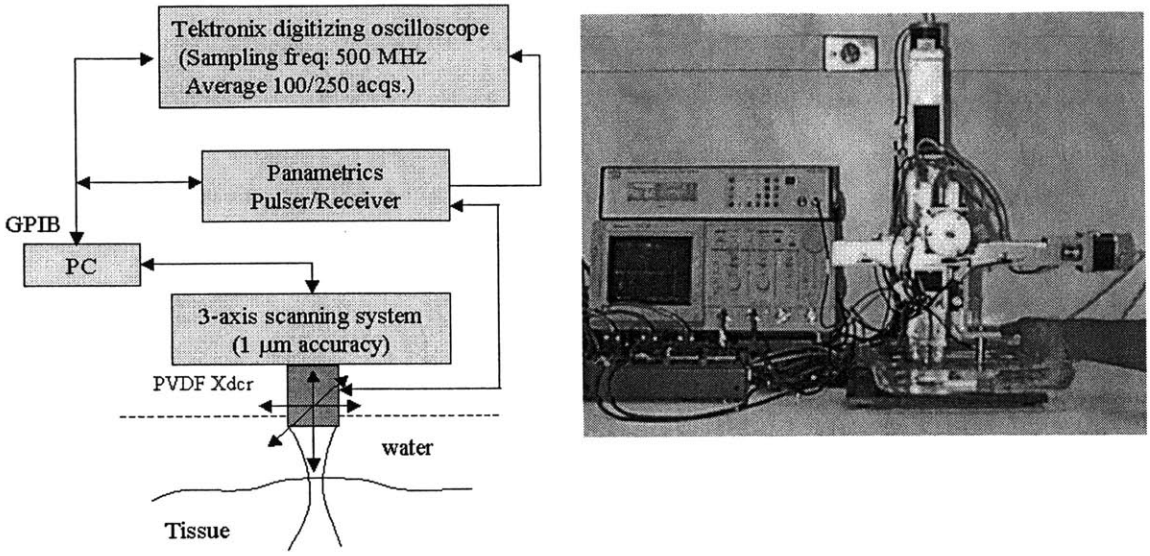

Figure 2.4: System II with computer controlled positioning of the transducer. The right panel shows the fingertip being immersed in the water bath during imaging.

Data for tissue characterization studies were collected from the forearm and the fingertip of human volunteers. During a typical data collection experiment, echo sequences from 25 lateral locations were recorded. At each lateral location, echo sequences from 10 axial locations were recorded. The total time of imaging was about 6 minutes. Although this time was large, problems due to patient movements were not significant in tissue characterization studies, since the aim was to collect independent echo lines though lateral scanning. Still, efforts were undertaken to limit subject movements during the experiment. While collecting data at the forearm, velcro straps were used to hold the arm steady. A small cup was used to hold water. The bottom of the cup had a slot to allow passage of the ultrasound. The cup was glued to the skin using a double stick tape. While collecting data at the fingertip regions, custom designed finger splints made of a thermo polymer material (Smith & Nephew Inc., Germantown, WI; Rolyan #A292-01,) were made for each subject to hold the fingertip steady. The splint was glued to the bottom of a water bath. While no special attempt was made to maintain the temperature of water to be constant during a given experiment, the temperature at the start of the experiment was uniform for all subjects (36°C).

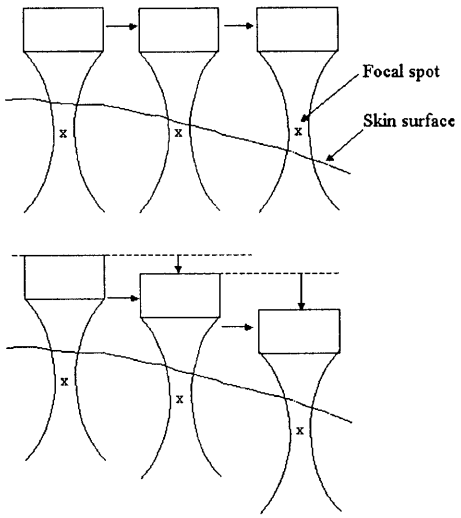

Figure 2.5: Skin curvature effects. In ultrasonic tissue characterization studies, power spectra from focal zone depths of adjacent locations are averaged to compute mean spectra. When such a procedure is applied to high frequency imaging of skin, due to the curvature of the surface, averaging occurs between data at different depths (top). In some cases the focal zone location might even move out of the surface. Hence the system adjusts for this by measuring the time-of-flight and translating the transducer up and down (bottom). Then several axial scans are performed at the same lateral location, followed by lateral scans to collect data from other locations.

2.4 System III: Fast scan system

The next step was to improve the system to be capable of both imaging and tissue characterization in a clinical environment. While the motorized scanning system was a significant improvement over the manually scanned system, the time of imaging was still too long to be used in a clinical setting. In a clinical setting, imaging should be done as quickly as possible in order to reduce strain on the patient. The reason for the long imaging time with the previous system was that the data transfer rate from the digitizing oscilloscope to the PC using the GPIB interface was slow. While GPIB communication protocols can handle high data transfer rates up to 1.5 Mbytes/sec (with an ISA interface board), the increased time taken by the digitizing oscilloscope to parse the commands sent by the PC reduced this to much smaller rates. Benchmark experiments showed that a maximum of 4 waveforms could be transferred per second, independent of the number of samples in the waveform. The time required to transfer a waveform from the digitizing oscilloscope to the PC directly determines the time of imaging as follows: Assume that the data are collected at regular intervals during a continuous motion of the transducer. Then the inter-sampling distance should be smaller than half the lateral resolution of the system in order to avoid aliasing artifacts. Data from the echo line at one location must be

transferred to the computer during the time it takes the transducer to move to the next location. Assuming an inter-sampling distance of 25 μm, it can be seen that with 0.25 sec to transfer a waveform from the digitizing oscilloscope to the PC, the speed of transducer motion could be at most 0.1 mm/sec. This in turn would lead to an imaging time of 50 sec for a typical 5 mm scan, which is too long for the subject to sit still.

To reduce the transfer rate from the digitizer to the PC, the digitizing oscilloscope in the earlier system was replaced with a high-speed A/D board (Gage Applied Sciences, Montreal, Canada; Model CompuScope 8500). The board could transfer data from its on-board memory to the PC's memory at rates of up to 100 Mbytes/sec using the PCI bus. Unlike in the case of the digitizing oscilloscope, very little overhead is required in communicating with the A/D board. Another change from the earlier system was that the discrete step based scan was replaced with a continuous scan of the transducer. In this case, backscattered data from the tissues are tapped off periodically and transferred to the PC's memory while the transducer is in a continuous motion. The continuous scan ensured that communication delays between the PC and the motion control system do not offset the improvement in faster data acquisition rates with the A/D board.

A number of design constraints needed to be addressed while designing this system, due to the conflicting requirements between duration of imaging, image quality, limitations in hardware, ease of building the system, simplicity in use, and overall cost. In order to design the system, the following points were first noted:

1. While the primary aim of this work is tissue characterization, it is often advantageous to visualize conventional B-scan images as well. Tissue characterization experiments and imaging experiments have different requirements. In the former case, there is no need to collect contiguous echo lines that are spaced close together. In fact the echo lines should be separated by distances larger than the lateral resolution of the system in order to collect independent echoes. In the latter case, the echo lines should be spaced by a distance that is less than one half of the lateral resolution of the system (Nyquist sampling criterion), so that an image can be constructed by combining all the echo lines. Thus tissue characterization studies can be done on the data collected in imaging experiments, but not vice versa. Therefore, in order to have the capability to perform both characterization and imaging, the system should be capable of collecting echo lines that are spaced by less than half the lateral resolution of the system.

2. Unlike in the case of the digitizing oscilloscope, the A/D board does not have the ability to do on-board averaging of waveforms. Hence averaging must be done in software once all the independent waveforms are acquired and downloaded to the PC's memory. A finite amount of time is required by the PC to do the averaging and no further data collection can be performed until this averaging operation is completed. Also, enough memory is needed to store all the waveforms on the board before they can be downloaded to the PC. The importance of averaging is illustrated in Fig. 2.6 where it can be seen that the signal-to-noise in the waveform can be greatly improved by signal averaging.

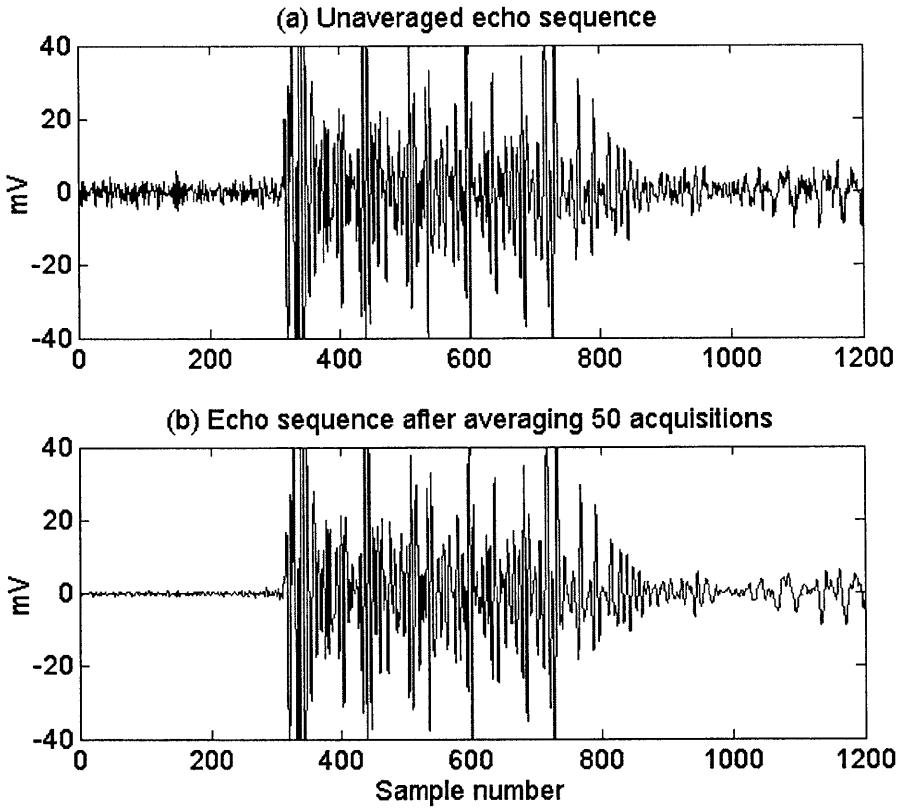

Figure 2.6: Importance of averaging. (a) A single waveform recorded from the human skin. The pre-echo portion of the waveform is seen to have considerable noise. (b) After averaging over 50 independent acquisitions of the same waveform, the noise level is seen to be much lower. (The y-scale in this figure was selected to be from –40 to 40 mV to illustrate the weaker signals. The actual recorded waveforms were not clipped.)

3. The sampling rate of theA/D board could be chosen to be 500 MHz, 250 MHz, 200 MHz, or lower. But the noise inherent in the A/D board was significantly higher when the sampling rates were at 500 or 250 MHz, than at 200 MHz. The lower sampling rate is

also advantageous as it leads to a smaller number of samples to download from the board to the PC (which takes less time) and to reduce time required for subsequent operations such as averaging. With this setting the analog filter setting on the receiver portion of the pulser was set to have a low pass cut off of 100 MHz.

4. The maximum admissible pulse repetition frequency (PRF) of the pulser is 20 kHz for all energy level settings except for the highest setting of 32 μJ, for which the maximum PRF was 10 kHz. These correspond to an inter-pulse interval of 50 and 100 μs respectively. If a total of 50 waveforms are to be recorded for averaging purposes, then a time duration that is 50 times the above period must elapse before all the waveforms could be acquired.

5. While performing a continuous scan, the speed of motion should be generally as high as possible subject to two constraints. First, during the time required to acquire say N waveforms (for averaging purposes), the transducer, which is in a continuous movement, should have moved by only a small fraction of the lateral resolution of the system. Otherwise, the various waveforms being averaged would not correspond to the same tissue location, and hence cannot be averaged together. Second, during the time the transducer takes to move to the next location where another echo line is recorded, three tasks must be completed: (1) All the N waveforms should be acquired at the previous location of the transducer (2) All the acquired waveforms should have been transferred to the PC's memory, and (3) A point-by-point averaging of all the waveforms should be completed.

The solution steps were as follows:

The first step was the selection of the transducer. The transducer PI50 with an energy setting of 4 μJ was chosen. The PI75 transducer lead to fuzzier images because of its poor focusing. The PI3005 transducer was less suited for imaging than the PI50 transducer due to two reasons: First, with a smaller aperture size (smaller collecting area for the backscattered echoes), the signal-to-noise ratio was poorer. Also, because of shorter focal length for this transducer (4.58 mm), secondary reflections (waves that have traveled twice between the transducer and the tissue, presumably due to slight impedance mismatch at the transducer face) were found to interfere with the echoes from deeper tissues. The PI50 transducer does not pose this difficulty as its focal length was much larger (12.7 mm), and secondary reflections, if any, would interfere with echoes from much deeper tissues, beyond any useful imaging depth.

With the 4 μJ setting on the pulser, a pulse repetition frequency of 20 kHz could be chosen. Thus the inter-pulse period was 50 μs. It should also be pointed out that this duration was much longer than the time to record all useful echoes for a single waveform. For instance, for the focal length of 12.7 mm and an additional imaging distance of say 4 mm beyond the focus, the time required for the wave to traverse the roundtrip distance would be about 23 μs (assuming a sound speed of 1.5 mm/μs), which is less than 50 μs.

The sampling frequency was chosen to be 200 MHz, which was sufficient to record echoes for the PI50 transducer (center frequency ~ 30 MHz). The board was chosen to operate in a multiple-record capture mode, wherein it could be triggered repeatedly to capture and stack a pre-determined number of waveforms in its memory. The number of samples in each waveform could be specified beforehand. The board captures the waveform up to the specified number of samples, and then re-arms itself to capture successive waveforms. This feature was especially useful in collecting repeated waveforms for averaging purposes. Rather than collecting the entire 50 μs of data per waveform, only a portion corresponding to the useful duration of about 23 μs was recorded for a each waveform. This reduced the memory requirements on the board and also reduced the number of samples that needed to be transferred and averaged subsequently.

The lateral spacing between the echo lines was chosen to be 25 μm, which was less than one-half of the lateral resolution of the system of 83 μm. The scanning speed and the number of averages that made up a single echo line were chosen by trial and error after some benchmark experiments. The speed was chosen to be 2 mm/sec, and the number of averages was chosen to be 50. For a PRF of 20 kHz, or 50 μs interval between firings, the total time to acquire all the 50 waveforms was 2.5 msec. During this time period, for a scanning speed of 2 mm/sec, the transducer moved by a distance of 5 μm, which was only 6% of the lateral resolution. Thus, this ensured that all the 50 waveforms used in averaging were acquired from more or less the same location of the tissue. Benchmark experiments then confirmed that for the above scanning speed, the system would be ready to collect the next echo line by the time the transducer moved to the next location 25 μm away. In other words, within a time of 12.5 ms (to cover 25 μm at 2 mm/sec) all the three processing steps mentioned earlier were accomplished: It took 2.4992 ms to acquire the 50 waveforms (theoretical value is 2.47 ms since 49 inter-pulse periods need to elapse, plus an additional 20 us for the 50^{th} pulse), another 2.2444 ms to transfer the entire data from the board to

the PC's memory (theoretical value at 100 Mbytes/sec is 4480*50/100 = 2.240 ms), and another 2.5194 ms for averaging the 50 waveforms. Hence a total time of 7.2630 ms elapsed before the system was ready to acquire further data, which was smaller than 12.5 ms. Hence the system was working according to specifications. It should also be noted that the experimental parameters such as the scan speed were not rigidly fixed, but could be modified by the user at the time of the experiment.

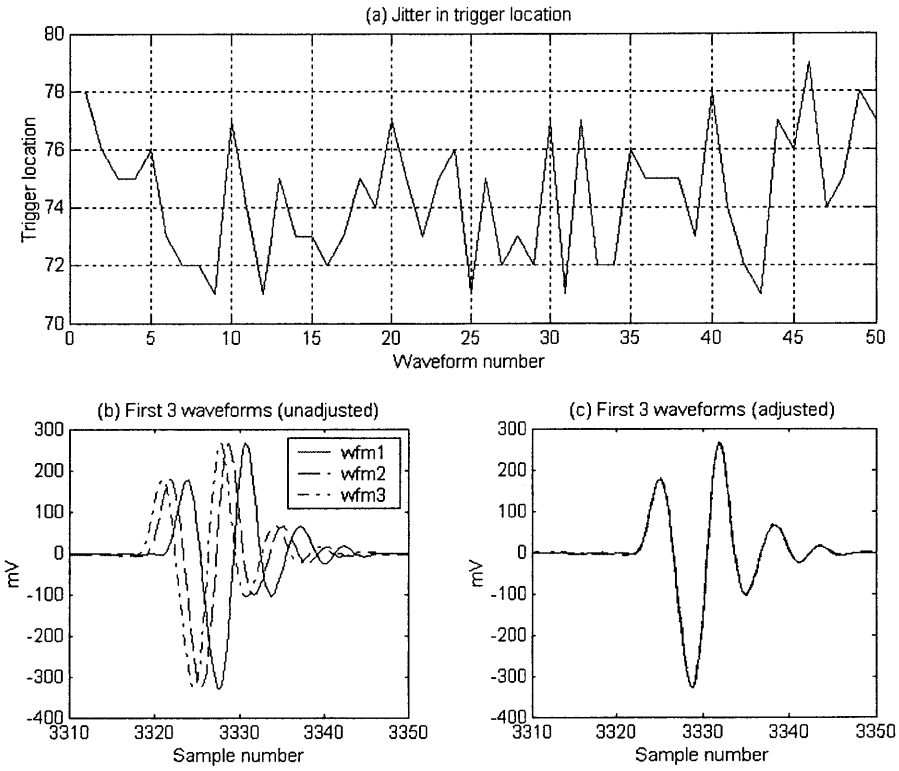

Figure 2.7: Trigger jitter problem in the A/D board. The location of the trigger randomly varied by as much as 8 samples, which made the waveforms to be out of alignment with one another. The problem was corrected in software using an alternate reference point instead of the trigger location.

Before the system could be implemented according to the above specifications, an additional hardware limitation of the A/D board had to be addressed. During the multiple-record mode, the trigger location for each waveform was known only approximately. Hence the starting point of each of the waveforms did not precisely coincide with that of one another. Because of this, the 50 waveforms were shifted a little bit with respect to one another, which meant that they could not be stacked up and averaged sample by sample. Figure 2.7 shows an example of this problem. It can be seen that the location of the trigger as stored by the hardware was not a constant but varied randomly by as much as 8 sample points. Therefore the captured waveforms were not aligned in

time. To overcome this problem, another absolute reference point, the location of the excitation pulse, was used as the start of each waveform. This was possible since the relative location of the excitation pulse with respect to the rest of the waveform was always constant. The location of the new reference point was determined in software (in real-time) in each waveform record after all the waveforms were transferred to the PC. As shown in Figure 2.7 (c), once this adjustment was made, the waveforms indeed coincided with one another in time, and could therefore be averaged to improve the signal-to-noise ratio.

Additional features were also added to the system compared to the previous system. Scanning was made possible in one of 12 horizontal directions. This reduced strain on the patient to adjust himself/herself to conform the tissue being imaged to a pre-determined scanning direction. Also to make the system more ergonomic, the part of the system that held the transducer was made more flexible though the use of custom designed brackets. This increased the workspace of the device and the patient could be more comfortably seated or reclined on a chair or gurney. In order to comply with electrical safety requirements, medical grade isolation transformers (Dale Technology Inc., Thornwood; Model IT 1100) to reduce ground loop currents were also added to the system. Figure 2.8 shows a picture of the imaging system

With a scan speed of 2 mm/s, the total time for imaging for a scan length of 5 mm was only 2.5 seconds, twenty times shorter than the 50 seconds it would have taken with the previous system. The only limitation of this system was that since the imaging time needs to be small, elaborate axial scans and height adjustments to minimize diffraction effects as described in the previous section could not be performed. Instead, in order to correct for diffraction effects, empirically determined correction curves as described in Chapter 5 were used.

.

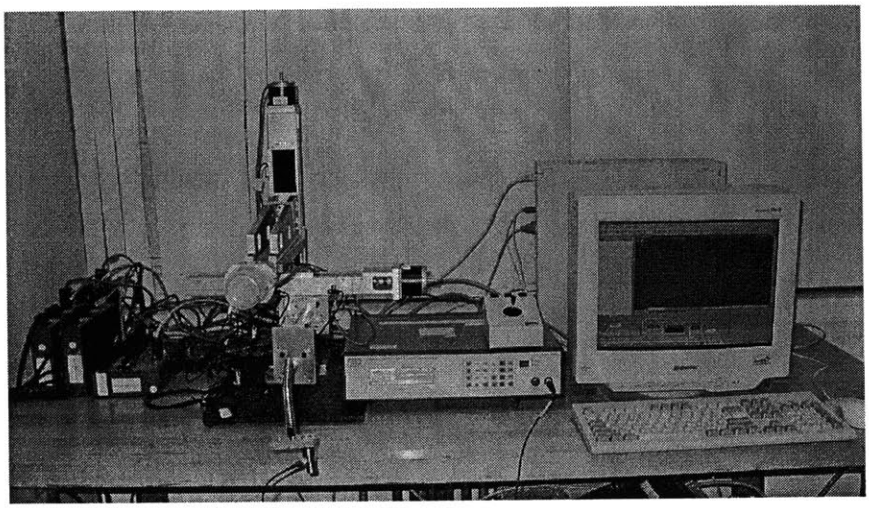

Figure 2.8: Picture of System III.

2.5 In vivo images of human skin

Four examples of skin images obtained in vivo with the fast scan system are now described. All the images correspond to normal skin tissues and were obtained using the PI50 transducer with an energy setting of 4 μJ. Figure 2.9 shows the image taken at the volar side of the forearm of a 47 year-old male subject. The difference between the echo-rich dermis and the echo-poor fat can be clearly seen. Also seen is a vein that is about 2.25 mm in diameter. Figure 2.10 shows the image of the left index fingertip of a 28 year-old male subject. The fingerprints on the surface can be seen in the image. Also seen is an interface below the surface, which most likely corresponds to the interface between the stratum corneum and the viable epidermis. Figure 2.11 shows the image taken at the transition region from the skin to the nail on the dorsal side of the index finger. The difference between the skin and nail regions can be clearly seen. Figure 2.12 shows the image of a scar tissue in the hand of a 30 year-old female subject. The length of the scar measured with a caliper was approximately 5 mm, which is also confirmed by the ultrasound image. In the ultrasound scan, the scar tissue is seen to be hypoechogenic with respect to the dermis. An image of skin affected by contact dermatitis is also shown in Chapter 5.

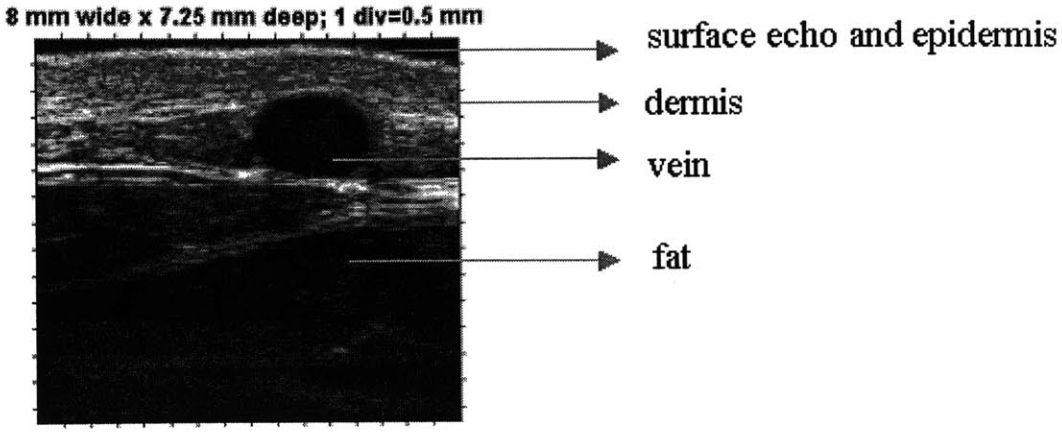

Figure 2.9: In vivo image of the forearm skin. The divisions in this image and following images are 0.5 mm apart.

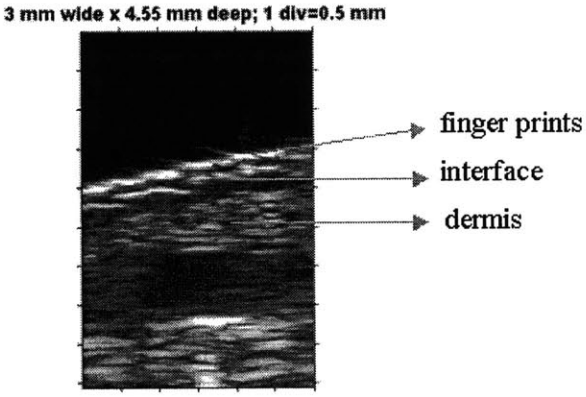

Figure 2.10: Image of a fingertip skin.

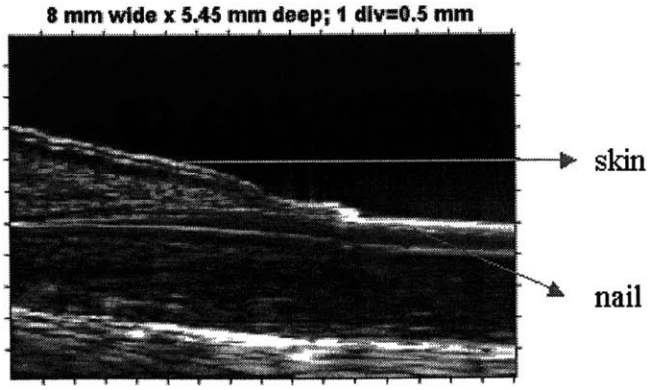

Figure 2.11: Image of the transition from skin to nail.

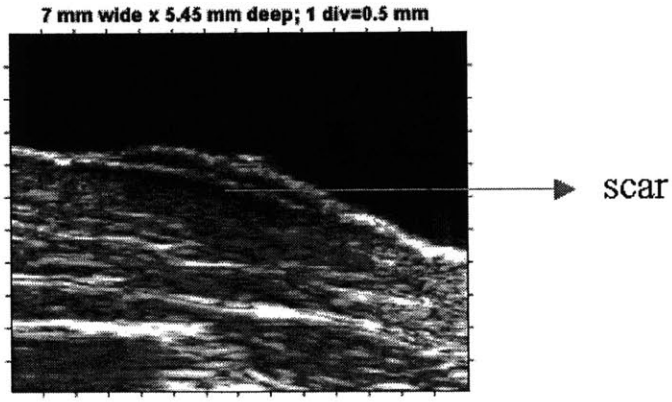

Figure 2.12: Image of a scar tissue.

3 Attenuation and Backscatter Coefficients of Normal Skin Tissues[2]

3.1 Introduction

Ultrasonic tissue characterization studies are undertaken because of the fact that only a portion of the total information in the echoes is used in displaying B-scan images. Therefore additional signal processing to extract quantitative parameters has the potential to enhance the diagnostic utility of ultrasound systems. This chapter describes the extraction of two such parameters, namely the attenuation and backscatter coefficients of normal skin tissues. Ultrasonic attenuation results from two basic mechanisms, namely absorption and scattering. Absorption is the conversion of energy into heat and can be attributed to relaxation mechanisms. However no theoretical mechanism has been shown to be fully capable of modeling the absorption mechanisms in tissues [93, 94]. Scattering loss occurs because the incident wave is partially redirected in many directions, and therefore the energy of the propagating wave is reduced. The exact contributions of absorption and scattering to ultrasonic attenuation are generally unknown, although in the low MHz range (1-10 MHz) evidence exists to show that absorption is a more dominant mechanism [49, 52, 95]. The estimation of attenuation coefficients from in vivo pulse-echo measurements requires comparison of the recorded signals from several depths in the tissue. However the signals being compared between various depths will differ not only because of attenuation, but also because of changes in backscatter coefficients between the depths. This difficulty is overcome by assuming that the region over which attenuation is being computed is homogeneous, which is equivalent to assuming a constant backscatter coefficient for the tissue at all the depths. Thus the attenuation coefficients reported in this work must be interpreted as inferred attenuation coefficients in the sense they represent the signal loss as recorded by the measuring device. The attenuation coefficients of most tissues are seen to have a power-law type of relationship with frequency, with the exponent ranging between 1 and 1.4 [93]. This exponent in the power-law dependence is one parameter that could be exploited for tissue characterization. In some cases a linear dependence is seen with frequency (exponent = 1). In such cases, the slope of the attenuation coefficient could be used as a parameter for tissue characterization.

[2] This chapter is based on an article published in Ultrasound in Medicine and Biology [92].

The backscatter coefficient is defined as the differential scattering cross-section per unit volume of tissue at an angle of 180°. The backscatter coefficient of tissues depends on the size, shape, density and the material properties of the scatterers distributed in the tissue. Theoretical developments for obtaining the backscatter coefficients of single scatterers of regular geometries, such as spheres or cylinders are available in the literature. However in the case of biological tissues, the complexity and diversity of the various tissues make theoretical development difficult. In practice, the computation of backscatter coefficients is done empirically by making simplifying assumptions to remove the effects of the instrument characteristics from the recorded echoes. Since most tissues exhibit an increasing trend in the backscatter coefficient with frequency, a power-law dependence, with an exponent ranging between 0 and 4 is often used to describe the backscatter coefficient. An exponent of zero implies frequency independent geometric scattering while a value of 4 indicates Rayleigh type scattering. This exponent is thus an additional parameter that could be used for characterizing various tissues. The present chapter describes the empirical computation of attenuation and backscatter coefficients of skin tissues in the range 14-50 MHz. In order to make sure that the results are independent of the measuring system, attenuation coefficients are measured using three different transducers. Backscatter coefficients are also measured using three different transducers by compensating for system dependent effects, and additionally for one transducer, using the reference phantom technique [96]. Implications of the results to skin characterization are then discussed.

3.2 Methods

3.2.1 Human subjects and tissues

Skin consists of a superficial layer of epidermis and an underlying layer of dermis. The region beneath the dermis consists of subcutaneous fat, which is sometimes considered as a third layer of skin and is referred to as the hypodermis. In most parts of the body the epidermis is very thin compared to the dermis (0.15 mm vs. 1.2-1.8 mm) except at the palms and soles where it is much thicker (~ 0.6 mm). In this study, data were collected from 2 grossly different locations: the dorsal side of the right forearm (hairy skin) and the left index fingertip (glabrous skin). At the forearm, two body-sites one near the wrist, and the other near the elbow were studied. The reason for choosing two sites at the forearm was that due to their proximity, one of them could serve as a control for the other. Table 3.1 summarizes the tissues studied and the subject population. Since skin condition could depend on the subject's age the present study was restricted to only young

adults. The first transducer was used for all the three body-sites in order to study differences due to body-site. All three transducers were used to collect data from the forearm wrist region in order to test system independencies. In the case of skin regions near the forearm wrist and elbow, data were collected from 10 locations of the focal zones (axial scans) starting from 0.3 mm below the surface up to a depth of 3.0 mm in steps of 0.3 mm, which covered both the dermis and fat. In the case of fingertip, data were recorded from 12 locations of the focal zones from 0.3 mm up to 1.95 mm in steps of 0.15 mm, which covered both the epidermis and dermis. Due to reasons concerning logistics, the same set of subjects were not used for all the three transducers, but the median ages were about the same (Table 3.1). All the subjects that participated in the fingertip study were right-handed. For each of the experiments done, a second independent repetition at a close-by region (displaced by a few mm from the original site) was done to increase the number of independent data sets. All subjects signed an informed consent document approved by the Institutional Review Board of the Massachusetts Institute of Technology.

Table 3.1: Tissues and subjects used in this study.

Body-site	Transducer	Tissues	Subject population	
			n	Ages: range (median)
Forearm wrist	PI50 (I)	Dermis and fat	16	20-36 (26.5)
	PI75 (II)	Dermis and fat	16	22-36 (28.5)
	PI3005 (III)	Dermis	16	19-36 (24.5)
Forearm elbow	PI50 (I)	Dermis and fat	13	19-34 (24.5)
Left index fingertip	PI50 (I)	Dermis	18	20-33 (24.5)

3.2.2 Data collection

In this work data were collected from all three transducers. For the sake of convenience, the PI50, PI75, and PI3005 transducers (Table 2.1) will be referred to as transducer I, II and III respectively. Energy settings of 32 μJ were chosen for transducers I and II, and 16 μJ was selected for transducer III. Echo lines were collected from 25 independent lateral locations of the transducers by scanning along x and y in a 5 by 5 raster format. The area over which the 25 echo lines were recorded was 1.5 mm x 1.5 mm for transducer I, 3 mm x 3 mm for transducer II, and 1 mm x 1 mm for transducer III. These corresponded to lateral stepping distances of 0.3, 0.6, and

0.2 mm for the three transducers. The larger stepping distance for the case of transducer II reflects the poorer resolution of this transducer.

3.2.3 Power spectra computation

Once data from all focal zone locations and all lateral locations were obtained, a time-gate of 128 samples, (total gate length = 0.256 μs, corresponding to a frequency resolution of about 4 MHz) was applied to select data at the focus of the transducers. These gated data were truncated by applying a Hamming window, Fourier-transformed and squared to compute individual power spectra for all lateral locations and at all axial locations of the transducer. While it is customary to compute the mean of the spectra recorded from all lateral locations, in this work it was found that a trimmed mean wherein the top and bottom 25 percentile of the data were eliminated, was more useful. Such a quantity is less sensitive to the presence of extreme variations in the data and will be simply referred to as the mean spectra in this work. The approach was especially useful in the case of subcutaneous fat where strongly reflecting fibrous septae were present occasionally. Figure 3.1 shows mean spectra for 10 locations of the focal zones at the forearm of a human subject obtained with transducer I.

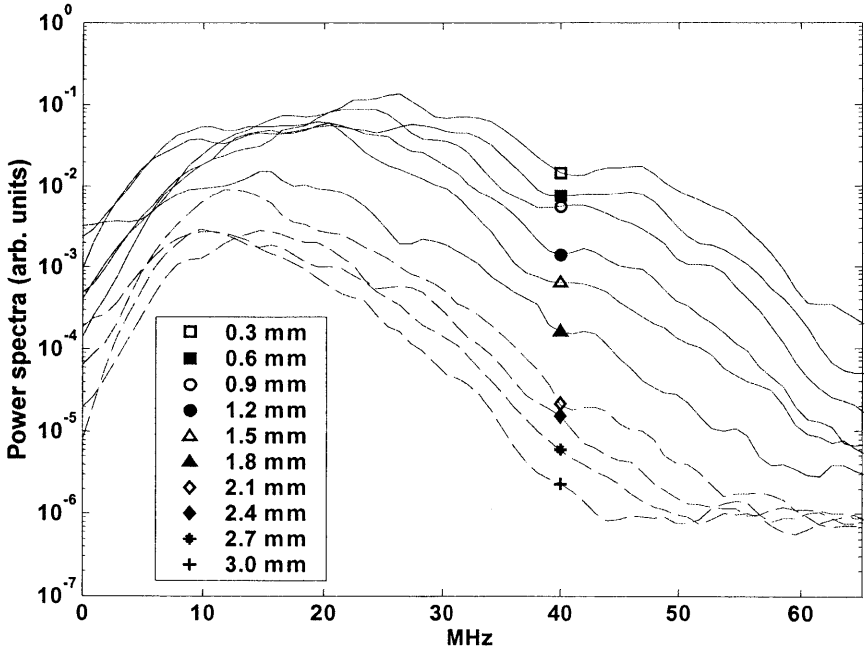

Figure 3.1: Mean power spectra of backscattered signals from 10 focal zone locations in the skin (locations indicated in the inset). See also Fig. 3.2.

3.2.4 Attenuation estimation

The total amplitude attenuation coefficient has contributions from both absorption and scattering effects [93]:

$$\alpha(f) = \alpha_s(f) + \alpha_a(f) \tag{3.1}$$

where $\alpha_a(f)$ is the amplitude absorption coefficient and $\alpha_s(f)$ is the amplitude scattering coefficient. The scattering loss in turn is proportional to the total loss by redirection of the wave over all angles [97]:

$$\alpha_s(f) \propto \int_{4\pi} \left(\frac{d\sigma(f)}{d\Omega} \right) d\Omega \tag{3.2}$$

where $\frac{d\sigma}{d\Omega}$ represents the differential scattering cross-section per unit solid angle of the tissue, and is a function of the frequency f. In this work, the total attenuation coefficient, which is inferred from pulse-echo measurements at several depths, will be referred to as the attenuation coefficient. The mean power spectrum of the echo from a particular depth z_i at a frequency f can be expressed as:

$$S(f, z_i) = H(f, z_i) B(f, z_i) e^{-4\alpha(f) z_i} \tag{3.3}$$

where $H(f, z_i)$ is a term that accounts for the electromechanical frequency response of the transducer as well as depth dependent diffraction effects, and $B(f, z_i)$ is the backscatter coefficient of the tissue at the depth z_i. Since the computed power spectra are dependent on both the attenuation coefficient and the backscatter coefficient, it is in general not possible to extract the two quantities from a single set of measurements. At this point, it is assumed that all the depths correspond to the same tissue, and hence the backscatter coefficient is independent of the depth z_i. Such an assumption is reasonable when a homogeneous region can be identified and considered to constitute a particular tissue, and all the depths are present within this tissue of interest. As described later in this section, such homogeneous regions were chosen for the dermis and fat. With this assumption,

$$B(f, z_i) \cong B(f) \quad \forall z_i \tag{3.4}$$

Moreover with the axial translation technique done to minimize depth-dependent diffraction effects (Section 2.3), the function $H(f, z_i)$ can also be considered to be independent of the depth z_i:

$$H(f, z_i) \cong H(f) \ \forall z_i \tag{3.5}$$

Thus Eq. (3.3) can be written as

$$S(f, z_i) = H(f)B(f)e^{-4\alpha(f)z_i} \tag{3.6}$$

If a particular frequency is now considered, the frequency dependence can be dropped to obtain the following expression for the recorded spectra as a function of depth:

$$S(z_i) = Ae^{-4\alpha z_i} \tag{3.7}$$

where A is a constant that depends only on the frequency. Thus the attenuation coefficient α (dB/mm) at a particular frequency can be obtained through an exponential fit of the power spectra as a function of the depth within the tissue.

In light of the above arguments, the first step in computing the attenuation coefficient is the identification of a homogeneous region corresponding to a particular tissue of interest. This was done by plotting "pseudo-images" using the collected data, as shown in Fig. 3.2. Such images serve to differentiate grossly different regions such as the dermis and fat. In this example, the strongly scattering dermis is seen to extend about 1.8 mm beneath the surface. To convert time-of-flight to depth, a speed of sound of 1.5 mm/μs was assumed throughout this study, which is close to values reported in the literature [21, 98, 99]. Small discrepancies in speed do not affect the computed attenuation values (dB/mm) significantly, and hence a convenient value of 1.5 mm/μs was used. In general, most of the subjects had a dermal thickness between 1.3 and 1.8 mm, and hence the first four focal zone locations (at 0.3, 0.6, 0.9 and 1.2 mm from the surface) were taken to correspond to dermis for all subjects. A few subjects whose forearm dermal thicknesses were less than 1.2 mm were eliminated from the study a priori so as to maintain uniformity. The focal zone locations beneath the dermis were taken to correspond to fat, with care taken to avoid fibrous septa that were sometimes seen in the pseudo-images. Figure 3.1 also demonstrates how the useful frequency range for analysis was chosen. At higher frequencies, the spectra tend to become flat once the noise floor is reached, especially for signals from the deeper fat tissues. In order to have a SNR of at least 10 dB, a frequency range of 14-50 MHz was chosen for the dermis and a range of 14-34 MHz was chosen for fat.

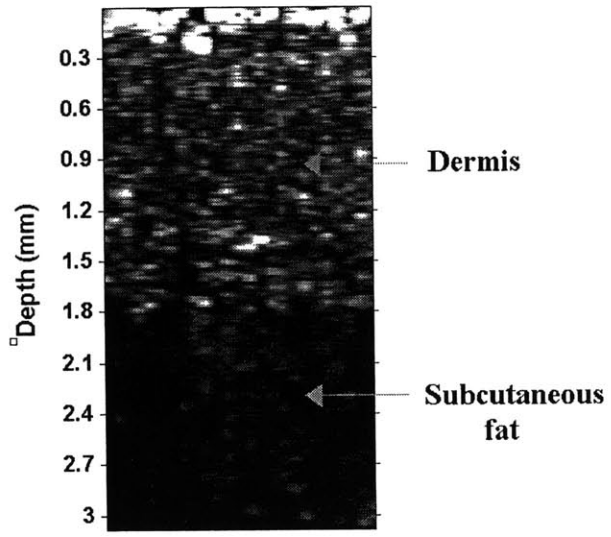

Figure 3.2: A pseudo image based on the collected data. The term pseudo implies that the image is not a usual B-scan image, as the lateral stepping distance was larger than the lateral resolution of the system, and also the collected data was actually 3-dimensional whereas the pseudo image is plotted as though the data is 2-dimensional, by laterally combining all the y-scans and all the x-scans together. Such images were used to a priori differentiate between dermis and fat.

In order to determine whether 4 focal zone locations were sufficient to accurately compute attenuation coefficient, two benchmark experiments were done on forearm skin for one subject before data collection from all subjects were done: The first experiment had seven closely spaced focal zone locations starting from 0.3 mm below the surface and extending to 1.2 mm in steps of 0.15 mm. The second had only four focal zone locations in steps of 0.3 mm. The attenuation coefficient slopes computed for the two cases were 0.2241 and 0.2483 dB/mm/MHz respectively, indicating only a 11% higher value for the case with coarser spacing for than the one with finer spacing. Hence it was decided to use the coarser spacing in the axial direction for all further experiments as adding additional focal zone locations increased the data acquisition time.

3.2.5 Frequency dependence of attenuation coefficient

In order to determine the frequency dependence of the attenuation coefficient, a linear fit of the form $\alpha(f) = \beta f + C$ as well as a power law fit of the form $\alpha(f) = Af^n + C$ were done. While the former was done using linear-least squares techniques, the latter was done using a non-linear optimization method using the optimization toolbox in Matlab.

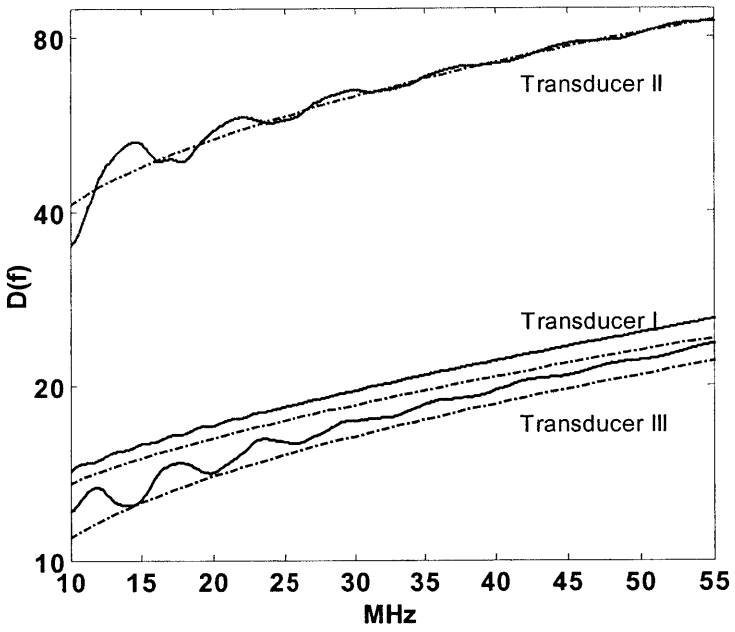

Figure 3.3: Comparison of the diffraction correction term used in this work (solid) with that given by the analytical expressions of Chen et al [100] (dashed).

3.2.6 Backscatter coefficient estimation using compensation for system-dependent effects

Measurement of the backscatter coefficient requires compensating the recorded spectra for the electromechanical response and the focusing properties of the transducer, and for the characteristics of the receiver electronics. In this work, backscatter coefficients were computed by two different methods. The first method is similar to that of Madsen and co-workers [101], wherein the system dependent effects are accounted for by accurately modeling the physics of wave propagation phenomena during the data reduction step, whereas the second method is the reference phantom method as described by Zagzebski and co-workers [96, 102]. Other methods for quantifying backscatter coefficients of tissues can also be found in the literature [24, 27, 30, 100, 103, 104].

The first method involved computing corrections using the known transducer geometries and also recording the signal reflected off a plane reflector at the focus with known acoustic properties. The following formula was used to compute the backscatter coefficient:

$$B_t(f) = \frac{S_t(f)}{S_r(f)} D(f) I(f) \tag{3.8}$$

where $S_t(f)$ is the mean power spectrum recorded from the tissue of interest, $S_r(f)$ is the power spectrum of the signal reflected from a perfect reflector at the focus of the transducer,

$D(f)$ is a diffraction correction term defined below, and $I(f)$ is a term to account for attenuation by intervening tissues lying shallower to the tissue of interest. The attenuation coefficients computed beforehand for each tissue were used to compensate for attenuation within the tissue of interest while computing $S_t(f)$. Such a procedure basically assumes homogeneity in tissue properties for all the depths making up the tissue of interest. The term $I(f)$ is an additional term to correct for intervening attenuation, for example, compensating for attenuation by the dermis while computing backscatter coefficients of fat. The diffraction correction term $D(f)$ is given by

$$D(f) = \frac{\left| \iint_{S_{mirror}} ds \iint_{S'} \frac{e^{jk|r-r'|}}{|r-r'|} ds' \right|^2 \quad \mathrm{R} \quad \left(\frac{1}{0.63}\right)^2}{\iiint_{d\Omega} d\Omega \left| \iint_{S'} \frac{e^{jk|r-r'|}}{|r-r'|} ds' \right|^4 e^{-4\alpha(f)(r-r_1)}} \tag{3.9}$$

The detailed derivation of the above equation is presented in Appendix A. A brief explanation for the terms in the above expression is as follows: The first term in the numerator represents a surface integral over the surface of the transducer (denoted by S'), followed by another surface integral over the surface of an identical transducer placed at a distance equal to twice the focus (denoted as S_{mirror}). The symbols r' and r refer to position vectors on the surface of the transducer and a generic point in the integration space respectively. The second term R is the intensity reflection coefficient between the plane reflector and the coupling medium water. The third term in the numerator $(1/0.63)^2$ is a factor that accounts for the Hamming window function used in computing the spectra [32]. The denominator consists of a surface integral over the surface of the transducer (denoted by S'), followed by a volume integral over the region occupied by the scatterers (denoted by Ω), modified by an exponential term that accounts for the attenuation within the gate ($\alpha(f)$ is the amplitude attenuation coefficient of the tissue of interest, and r_1 is the distance up to the start of gate). In practice, the computation of these integrals is a time-consuming task when numerical integration techniques are used. In this work, the above integrals were computed using the Angular Spectrum Method [105], which yields a much faster solution due to the efficient computation of FFTs. The computed diffraction correction functions were compared with simpler analytical functions given by Chen et al [100] for all three

transducers used in this work (Fig. 3.3) Good match is seen in terms of frequency dependence, but the simper formulation of Chen et al slightly under-predicts the diffraction correction for transducers I and III, both of which were more focused (f-number =2) than transducer II (f-number=4). In this work, the full diffraction corrections $D(f)$ as defined above were used, as they could be computed and stored a priori.

3.2.7 Backscatter coefficient estimation using the reference phantom method

The second method to compute backscatter coefficient was based on the use of a reference phantom, which has been previously employed in determining in vivo backscatter coefficients of other tissues such as liver [106-108] and kidney [108]. Such a method was used for computing backscatter coefficients using data from transducer II. The reference phantom was obtained from CIRS, Norfolk, VA and contained gelatin with randomly distributed spherical glass beads having a mean size of 82 μm and a standard deviation in size of 3 μm. Properties of the scatterers were provided by the manufacturer: The longitudinal wave speed is 5600 m/s; the density is 2.5 g/cc; and the Poisson's ratio is 0.22. The concentration of scatterers is 8000 particles/cc. The gel has a longitudinal wave speed of 1529 m/s and a density of 1.02 g/cc. The backscatter coefficient was computed using the formula

$$B_t(f) = \frac{S_t(f)}{S_{ref}(f)} B_{ref}(f) I(f) \tag{3.10}$$

where $S_t(f)$ is the mean power spectrum recorded from the tissue of interest compensated for attenuation within the tissue of interest, $S_{ref}(f)$ is the mean power spectrum recorded from the reference phantom (compensated for attenuation in the phantom up to the depth at which spectra were computed and for the transmission loss through the saran-wrap covering the phantom), $B_{ref}(f)$ is the backscatter coefficient of the reference phantom, and $I(f)$ is the intervening tissue attenuation compensation term. The quantity $B_{ref}(f)$ was computed according to Faran's model [109], assuming that the scatterers are randomly distributed, which leads to only incoherent scattering contributions. To compute the mean backscattered spectra from the phantom, $S_{ref}(f)$, 800 RF lines were recorded for averaging purposes in order to minimize possible effects of inhomogeneities. The phantom had a protective saran-wrap cover, and compensation for non-unity transmission coefficients at the water-saran-phantom interface was

computed at the required frequencies (14-50 MHz) using the methods described in Madsen et al [110].

3.2.8 Integrated backscatter

Once the backscatter coefficients were computed, the integrated backscatter was obtained in the range of 14-34 MHz using the formula

$$\text{Integrated Backscatter} = \frac{1}{f_2 - f_1}\int_{f_1}^{f_2} B_t(f)df \tag{3.11}$$

where $f_1 = 14$ MHz and $f_2 = 34$MHz. Even though reliable spectra were available up to 50 MHz for the dermis, the use of 34 MHz as the upper limit made it possible to compare dermis and fat tissues.

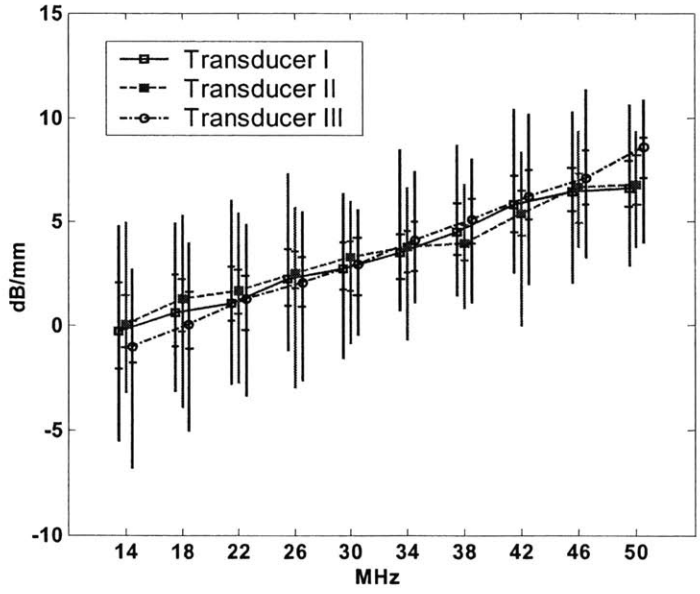

Figure 3.4: In vivo attenuation coefficients of the forearm dermis (wrist) in the range 14-50 MHz based on the 3 transducers. The markers indicate the median among subjects and the error bars indicate the full range of data. The tick marks on the error bars indicate the 25^{th} and the 75^{th} percentile points. The 3 curves are displaced slightly along the x-axis to make them more legible and the frequencies indicated on the x-axis are the actual values at which the attenuation coefficients were computed.

3.2.9 Statistical tests

In order to quantify differences in parameters between dermis and fat, such as attenuation coefficient slope and integrated backscatter, a paired t-test was used.

3.3 Results

Figure 3.4 shows the attenuation coefficient of the forearm dermis at the wrist, obtained using data from all three transducers. It can be seen that the attenuation coefficients based on the different transducers agree well with one another. To quantify the frequency dependence, both linear and power-law fits were done for data from all subjects, for all three transducers. The linear fit gave a slope β that ranged between 0.08 and 0.39 for all subjects (median=0.21 dB/mm/MHz). The power-law fit gave an exponent that ranged between 0.05 and 3.52 (median=1.06). The goodness of fit as determined by the correlation coefficient for both the linear and power law fits were quite similar (mean correlation coefficient R^2=0.95 for linear fit vs. R^2=0.96 for power law fit). It was also found that the power-law fit gave fitting parameters that had more variations from one subject to another than the linear fit parameters. Such variations were found even for repetitions done on a single subject (not shown), and can be attributed to difficulties in fitting power-law functions within a limited frequency range [111]. Hence within the range 14-50 MHz, the simpler linear frequency dependence of attenuation coefficient of the dermis adequately described the results obtained in this work. The use of a non-zero intercept for curve-fitting the frequency dependence is discussed in the next section.

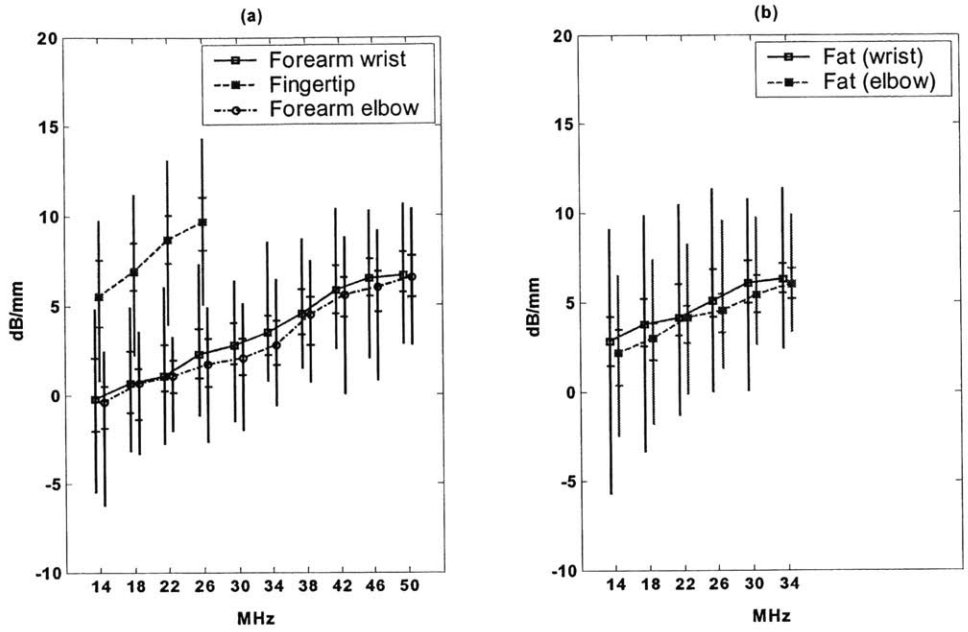

Figure 3.5: In vivo attenuation coefficient of (a) the dermis at 3 body-sites and (b) subcutaneous fat at two body-sites. The markers indicate the median and the error bars indicate the full range of data. The tick marks on the error bars indicate the 25^{th} and the 75^{th} percentile points. Individual curves are slightly displaced along the x-axis to improve legibility. Data at frequencies higher than 26 MHz in the case of fingertip dermis, and higher than 34 MHz in the case of subcutaneous fat were not used due to poorer SNR at these frequencies.

Figure 3.5 (a) shows the attenuation coefficient of the dermis at the three body-sites: forearm wrist, forearm elbow, and the fingertip obtained using transducer I. In the case of fingertip dermis only data up to 26 MHz was used due to a poorer SNR at higher frequencies. As expected, the results at the two forearm regions are similar (median $\beta = 0.21$ dB/mm/MHz at the wrist and 0.20 dB/mm/MHz at the elbow). At the fingertip however, the attenuation coefficient slope is higher (median $\beta = 0.33$ dB/mm/MHz) than that at the other two locations. Figure 3.5 (b) shows the attenuation coefficient of subcutaneous fat at the two forearm regions. The median β at the wrist and elbow were 0.18 and 0.19 dB/mm/MHz respectively. These values are close to that of the dermis, indicating similarity in attenuation coefficient slopes between dermis and fat. Figure 3.6 shows a histogram of the difference in attenuation coefficient slope between dermis and fat computed individually for all subjects (for transducers I and II). A paired t-test gave a p-value of 0.61 for the equivalence of the two means, indicating that there is little difference between dermis and fat in terms of attenuation coefficient slope within the frequency range studied.

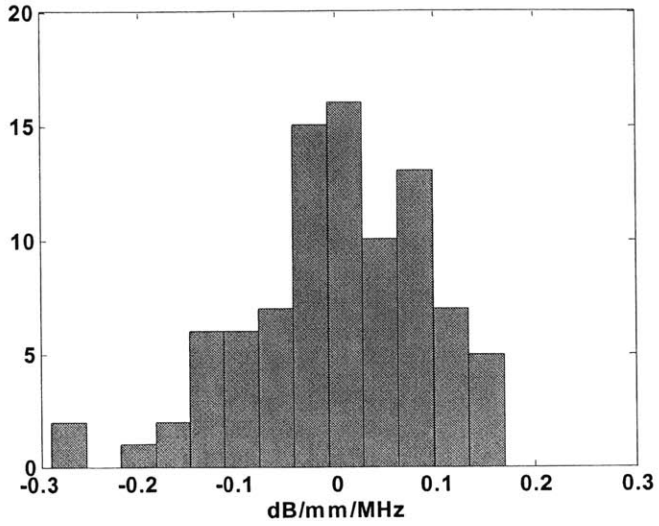

Figure 3.6: Histogram of difference in attenuation coefficient slope between the dermis and subcutaneous fat. All data obtained using transducer I at both forearm wrist and elbow regions and transducer II at forearm wrist regions were used to create the histogram (n=90). On the average little difference is seen between the dermis and fat in terms of attenuation coefficient slope within the range of frequencies studied.

Figure 3.7 shows the backscatter coefficient of forearm wrist dermis obtained using all three transducers as well as the reference phantom method using data from transducer II. Good agreement can be seen among these results despite differences in transducer characteristics. Some discrepancies seen in the plots could be attributed to assumptions used in computing backscatter coefficients as well as using a slightly different subject population for the three transducers. The backscatter coefficients were generally in the range 10^{-3} to $10^{-1}\,\mathrm{Sr}^{-1}\,\mathrm{mm}^{-1}$ and showed an increasing trend with frequency. Data from these plots were combined with data from transducer I at the forearm elbow and were plotted on a log-log scale (Fig. 3.12). An approximate increase in slope is seen at higher frequencies, which implies increasing power-law exponents when piece-wise power-law fits are done. For example if two power-law fits are done on the data, one for 14-30 MHz and the other for 30-50 MHz, the latter would show a larger value for power-law exponent than the former.

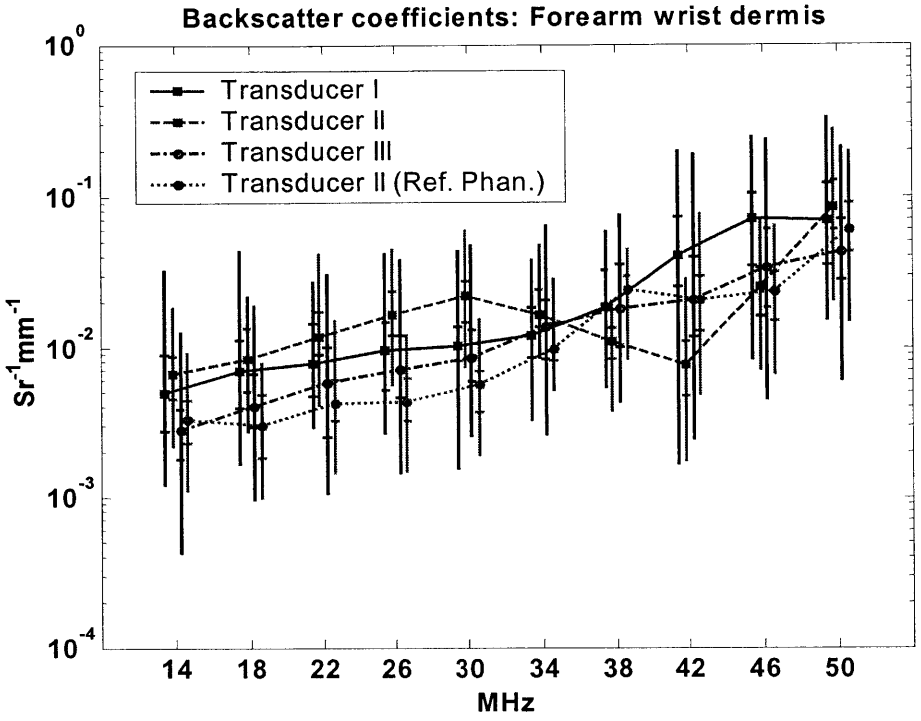

Figure 3.7: In vivo backscatter coefficients of the dermis at the forearm wrist location in the range 14-50 MHz. The markers indicate the median and the error bars indicate the full range of data. The tick marks on the error bars indicate the 25^{th} and the 75^{th} percentile points. Individual curves are slightly displaced along the x-axis to improve legibility. The backscatter coefficients were computed for the three transducers by compensating backscattered spectra for system-dependent effects, and additionally for transducer II, using the reference phantom method.

Figure 3.8 shows the backscatter coefficients of the dermis and fat at the two forearm regions obtained using data from transducer I. Results from the two regions match well for both dermis and for fat. Within the range 14-34 MHz, backscatter coefficient of fat showed a slight increasing trend followed by a slight decreasing trend. The results for fat also showed more variations than for dermis, the reasons for which could be attributed primarily to the occasional presence of strongly scattering fibrous septae in the fat. To compare the backscatter levels of the dermis and fat, a histogram of the differences in integrated backscatter (14-34 MHz) between the two was plotted (Fig. 3.9). All of the values were positive indicating higher integrated backscatter for dermis compared to fat. A paired t-test gave a p-value ≈ 0 for the hypothesis that the two means are the same. The ratio of integrated backscatter of dermis to that of fat computed for all data ranged from 1.03 to 87.1 (median value was 6.45), indicating that within 14-34 MHz, dermis on the average backscatters about six times stronger than fat.

3.4 Discussion

3.4.1 Summary of results

In this work, attenuation and backscatter coefficients from normal human dermis and subcutaneous fat were determined using human subjects under in vivo conditions. Attenuation coefficients of dermis in the range 14-50 MHz at the forearm wrist region were computed using data from 3 transducers, which showed good agreement with one another. Backscatter coefficients of dermis at the same location were also computed by compensating recorded backscatter spectra for the system-dependent effects, and additionally for one transducer using the reference phantom method. The computed backscatter coefficients based on the 4 methods agreed well with one another. Comparison of attenuation and backscatter coefficients between dermis and fat at the forearm region was done. Attenuation coefficients of the dermis at two locations, fingertip and forearm, were also compared. Table 3.2 presents a summary of the results.

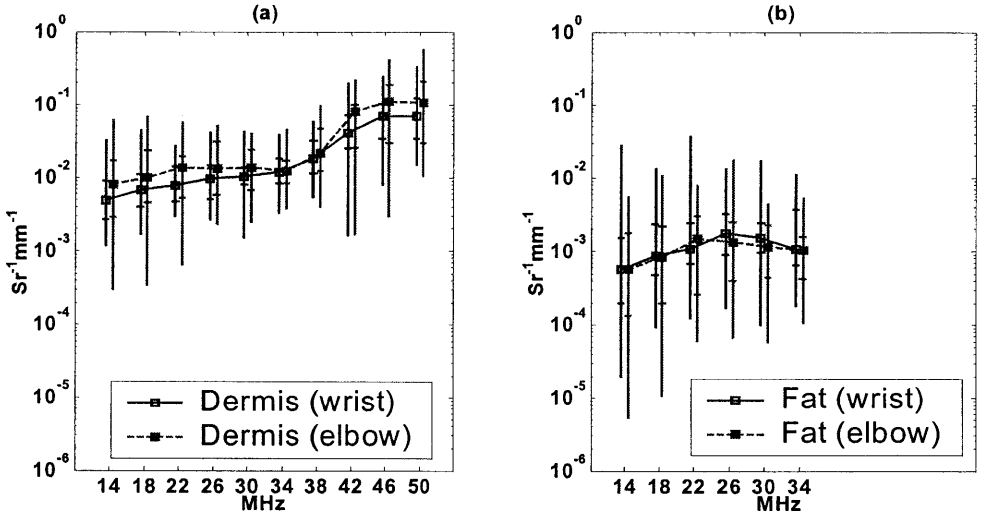

Figure 3.8: Backscatter coefficient of (a) the dermis and (b) fat at the two forearm regions obtained with transducer I. Markers and error bars indicate median and full range of data respectively. The tick marks on the error bars indicate the 25^{th} and the 75^{th} percentile points. Individual curves are slightly displaced along the x-axis to improve legibility.

Although the initial aim was to study all the 3 layers (epidermis, dermis, and fat) at both the forearm and fingertip regions, only a sub-set of these tissues could be studied, the reasons for which are as follows: First, for tissue characterization studies, the thickness of the tissue being investigated should be sufficient to compute power spectra over a windowed region free of surface and interface echoes. To compute the attenuation coefficients several such windows at successive depths are required. At the frequencies and pulse lengths used in this study, the

epidermis at the forearm region was too thin to fit this criterion. Next, while it was initially thought that the epidermis at the fingertip could be studied due to its increased thickness, the inhomogenities within the layer itself, such as the presence of a sharp interface at the stratum corneum-viable epidermis border made it difficult to select homogeneous regions, and therefore the fingertip epidermis could not be reliably studied from a tissue characterization perspective. The presence of such imhomogeneities noted in this study is consistent with earlier studies of ultrasound imaging of skin [81, 112]. Next, subcutaneous fat at the fingertip region could not be studied because the signals from this tissue were too weak and close to the noise floor level. Thus, in this work the forearm dermis, the forearm subcutaneous fat, and the fingertip dermis were the three tissues studied. Furthermore, because the fingertip epidermis was not studied, the backscatter coefficient of the fingertip dermis could not be computed because the intervening attenuation due to the epidermis could not be determined reliably.

Table 3.2: Summary of attenuation and backscatter results.

Tissue	**Attenuation coefficient slope[3] (dB/mm/MHz)** Range across subjects (median)	**Integrated backscatter (14-34 MHz) $\times 10^{-3}$ Sr^{-1} mm^{-1}** Range across subjects (median)
Forearm dermis	0.081-0.388 (0.211)	1.57-47.7 (8.52)
Forearm fat	0.037-0.399 (0.184)	0.06-14.6 (1.60)
Fingertip dermis	0.088-0.524 (0.331)	-

3.4.2 Attenuation coefficient measurements

Previous work by Riederer-Henderson et al [83] at 25 and 100 MHz indicated that the attenuation coefficient in skin might have a power-law type of dependence. Moran et al [21] also reported a power-law type of dependence of dermal and epidermal attenuation coefficients with frequency within the range 20-30 MHz, but whether a simpler linear fit could have modeled the data well enough was not mentioned in their work. Work by Pan et al [87] showed that attenuation coefficients in human skin at 20 and 30 MHz were 5.5 and 8.4 dB/mm respectively, from which a

[3] When the frequency dependence of the attenuation coefficient is linear, it is sometimes useful to express the attenuation on a per wavelength basis, which is a dimensionless quantity. The attenuation per wavelength can also be represented using the Q factor [113] using the analogy with loss in second order systems. The attenuation per wavelength for the dermis is 0.32 dB, and the Q factor is about 86.

power-law exponent (assuming $\alpha(f) = Af^n$) could be obtained to be n=1.04. Other researchers have assumed a linear frequency dependence while computing attenuation coefficients for the dermis [86, 88]. In this work, although power-law fits were analyzed, no advantage in using them over simpler linear frequency dependence was seen in the range 14-50 MHz for the dermis. It should also be noted that even if a power-law dependence is truly present, a large BW and computation of attenuation coefficients at several independent frequencies within this BW are needed to accurately determine the appropriate parameters [111]. Thus over the frequency range analyzed, a linear frequency dependence adequately described the attenuation coefficient of the dermis.

A surprising result from this study is that the attenuation coefficient slope of the dermis and subcutaneous fat are similar. This is different from earlier results by Guittet et al [88] where a lower value of attenuation coefficient slope was reported for subcutaneous fat. The reason for this difference is not clear, but it can be noted that the applicability of the spectral-shift method used in their studies becomes more limited when the bandwidth of the signals starts to change with depth. In their case a bandwidth equal to that obtained at the focus on a steel plate reflector was used for all depths, in which case an under-estimation of the attenuation coefficient slope could occur if the bandwidth is actually smaller than the one used. The results in this work show a decreasing trend in the bandwidth of the signals backscattered from deeper fat layers compared to the shallower dermis (Fig. 3.1). Another reason could be due to the different frequency ranges used. In this work the useful frequency for subcutaneous fat was chosen to be 14-34 MHz so as to avoid noise from biasing the results, whereas the values reported by Guittet et al were at a center frequency of 40 MHz. A histogram of differences in attenuation coefficient slopes between the dermis and fat computed in this work showed that on the average there is little difference between the two tissues (Fig. 3.6).

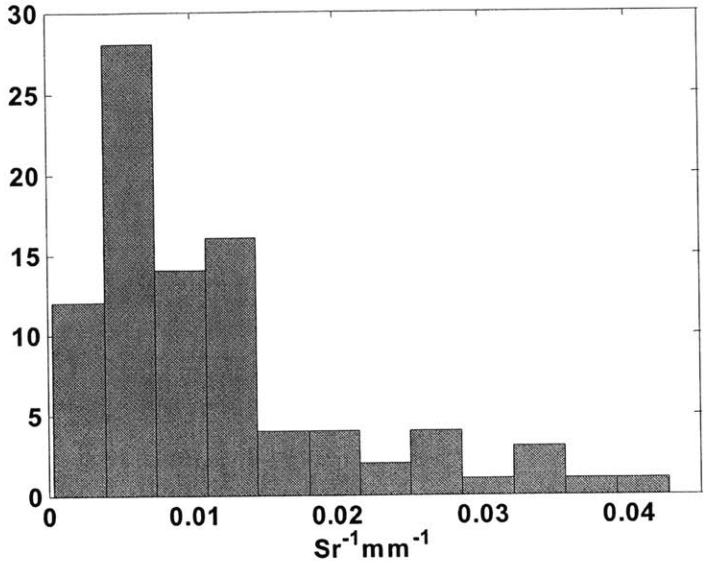

Figure 3.9: Histogram of difference in integrated backscatter between the dermis and fat in the range 14-34 MHz. All data obtained using transducer I at both forearm wrist and elbow regions and transducer II at forearm wrist were used to create the histogram.

The results in this work support the possibility that attenuation coefficients of the dermis could depend on the location in the body. The values at the fingertip were found to be higher than that at the forearm. Possible reasons are differences in skin tension at the two locations and differences in the underlying collagen structure at the two locations [87]. Further studies involving data collection from several body-sites are needed to establish regional variations in ultrasonic properties of skin.

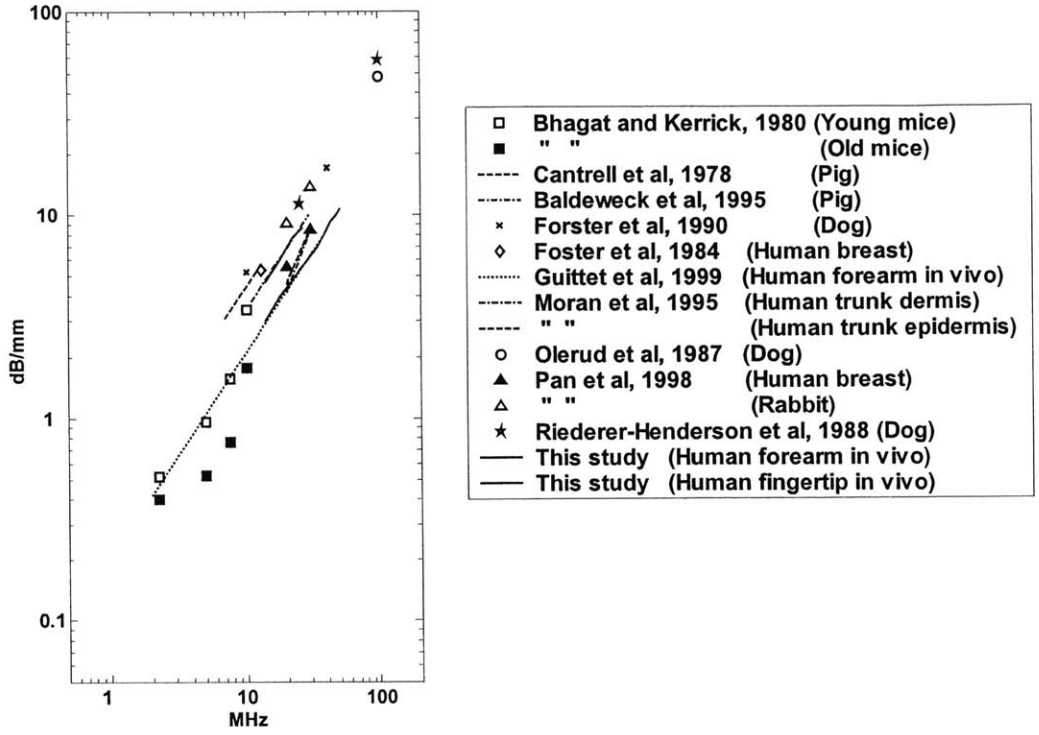

Figure 3.10: Comparison of in vivo attenuation coefficients of the dermis from this study with literature data.

When analyzing the frequency dependence of the attenuation coefficient of the forearm dermis, a non-zero intercept was used in both the linear and power-law models. This is consistent with the data shown in Fig. 3.5, wherein an extrapolation of the attenuation coefficients of dermis would lead to negative y-intercepts. Such negative intercepts imply an increase in recorded signal levels with distance at lower frequencies and can be attributed to increases in backscatter coefficients within the region analyzed. As described before, estimation of attenuation coefficients with in vivo backscattered data requires the assumption that backscatter coefficients are constant with depth within the region analyzed. When such a condition does not exist, the computed attenuation coefficients may not be true attenuation coefficients inherent to the tissues, but can only serve as a relative measure between different tissues. Several researchers have used such assumptions: Guittet et al for skin [88], Wilson et al [64] for vascular tissues, and Lu et al [107] for liver to name a few. Examples of fitting frequency dependence curves for attenuation coefficients with non-zero intercepts can also be found in the literature [51, 114]. Under these conditions, the measured backscatter coefficients are also only averages over the region of interest (e.g. in the case of dermis, over the range 0.3-1.2 mm beneath the surface). It is also worthwhile to note that

if changes in backscatter coefficients from one depth to another within the region of interest are relatively frequency independent, then the frequency dependence of attenuation is not affected except for a shift along the y-axis. Thus, the computed linear slope β would be independent of any frequency independent changes in backscatter coefficients over the region analyzed.

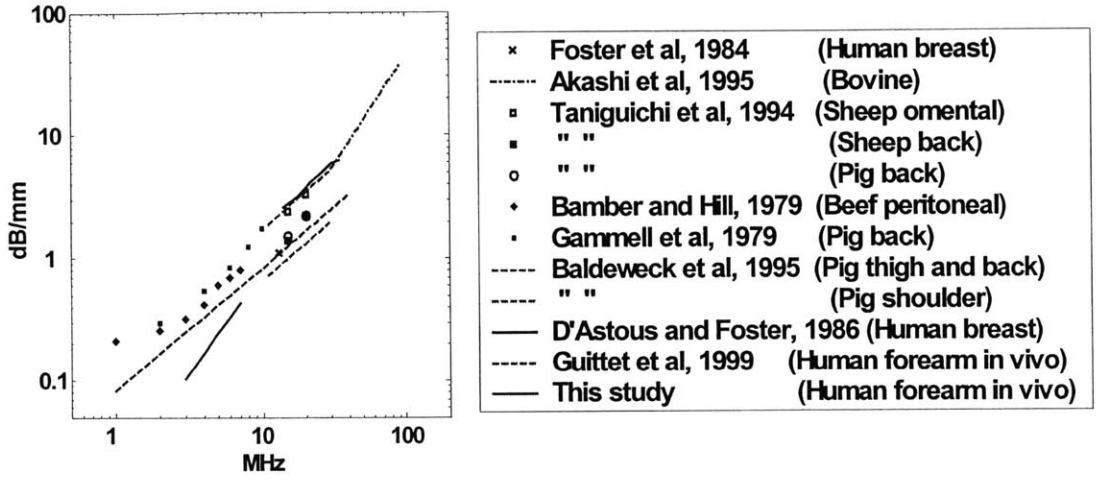

Figure 3.11: Comparison of in vivo attenuation coefficients of fat from this study with literature data.

Figure 3.10 shows the comparison of the results of computed attenuation coefficient slopes from this work with that found in the literature. To be consistent with other methods, only the attenuation coefficient slope (with the intercept removed) was used in comparing with literature data. It is to be noted that the previous in vivo results by Guittet et al (1999) were based on a spectral-shift method whereas the results here were based on a spectral-difference method and a good agreement between the two could be seen despite differences in methodology. Figure 3.11 shows a comparison of attenuation coefficient slopes of fat estimated in this work with that found in the literature. Additional references were obtained from Bamber and Hall [115], Akashi et al [116], Taniguchi et al [117], and Gammell et al [118].

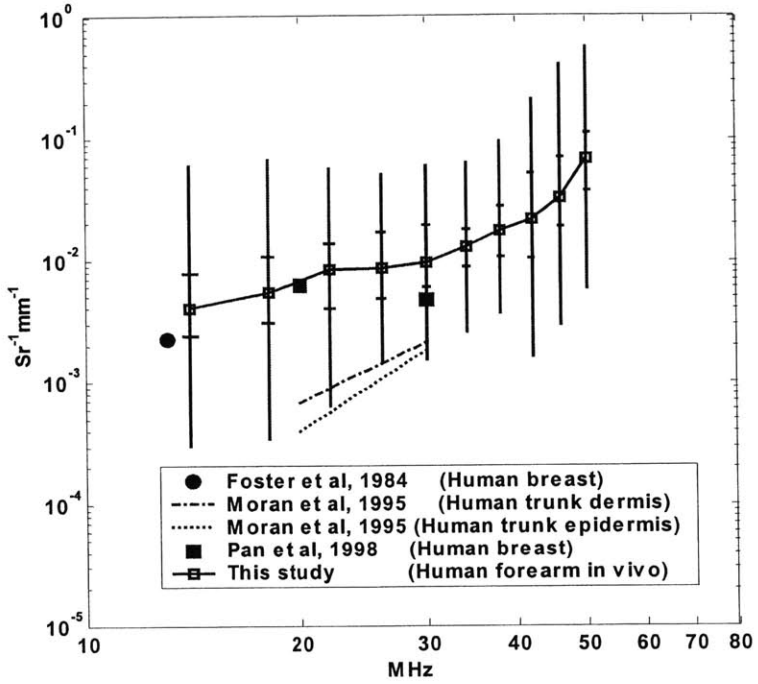

Figure 3.12: Comparison of in vivo backscatter coefficient of dermis from this study with literature data (in vitro). Data from Moran et al. (1995) is based on a power-law fit mentioned in their study.

3.4.3 Backscatter coefficient measurements

This work seems to be the first one where in vivo backscatter coefficients are being reported for dermis and subcutaneous fat. Only few in vitro data are available and a comparison is shown in Fig. 3.12. Differences between the present results and previous studies can be attributed to genuine differences between in vivo and in vitro tissues, specimen preparation effects, or differences in skin properties between forearm and other body-sites used for the other studies. To mathematically describe the frequency dependence of backscatter coefficients, a power-law fit has been used for many tissues, as backscatter coefficients typically tend to increase with frequency. In the case of the dermis, the backscatter coefficient computed in this study does not show such a simple behavior but rather increasingly stronger dependence at higher frequencies within the range 14-50 MHz. Such a behavior could result due to scattering from multiple populations of scatterers in the dermis. The dermis consists of a network of collagen fibers whose sizes approximately increase with depth. At the papillary layer closer to the surface the fibers are 0.3 to 3 μm in size whereas at the deeper reticular layer the sizes are coarser and 10 to 40 μm in size [119]. Scattering at lower frequencies (14-30 MHz) could be dominated by the larger sized

collagen fibers giving rise to a smaller power-law exponent, while scattering at higher frequencies (30-50 MHz) could be dominated by a high density of small-sized collagen fibers giving rise to a more Rayleigh type scattering with a higher value of power-law exponent. This is broadly consistent with the anatomical structure of the dermis. If a bimodal distribution of scatterers is assumed for the dermis, previous methods developed to estimate scatterer sizes from measured backscattered spectra could be used to estimate mean scatterer sizes for these two populations after suitably filtering the data to select relevant frequency ranges [26, 28]. Such analyses have been useful in determining scatterer sizes in kidney [58], liver [28, 54] and the eye [28]. The application of such methods to skin tissues will be the subject of future work. The possibility of complex frequency dependence of backscatter coefficient such as the presence of resonance patterns also exists if there is regularity in the size of scatterers. Such resonance patterns were not found (even on a single-subject basis, results not shown) in this study most probably due to wide variations in the sizes of the scattering structures in dermis. Conventional B-scans typically show that subcutaneous fat is hypoechoic compared to the dermis, but such a difference has not been quantified previously. The present results indicate that within the range 14-34 MHz, the integrated (average) backscatter of the dermis is about six times larger than that of fat (median of ratio of integrated backscatter of dermis and that of fat was 6.45). In conventional B-scans such a difference could get more exaggerated when the compensation for intervening attenuation is based on a smaller value of 0.5 dB/cm/MHz typical of soft tissues than the value of 2 dB/cm/MHz for dermis.

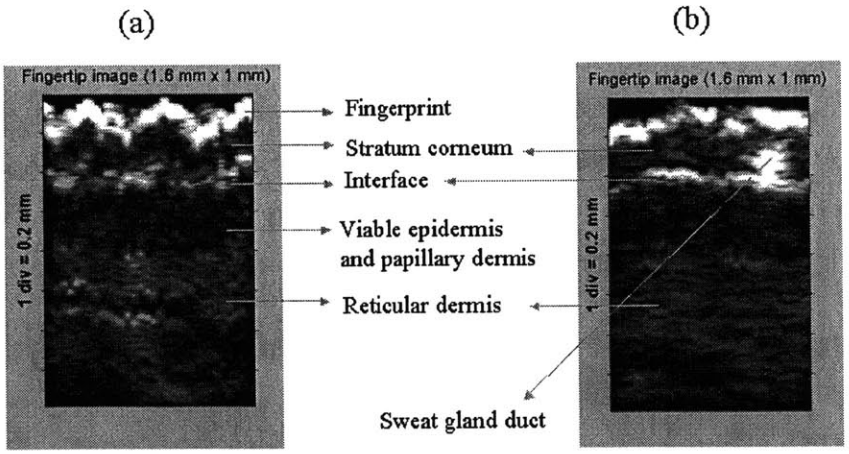

Figure 3.13: In vivo B-scan images of the fingertip of two human subjects. Both images show strongly reflecting interfaces beneath the surface that possibly correspond to the transition from the stratum corneum to the rest of the epidermis. In (a) scanning was done perpendicular to the finger ridges on the surface and fingerprints could be seen. In (b) bright structures within the stratum corneum that could possibly correspond to sweat gland ducts could be seen.

3.4.4 Limitations of the study

(a) Effect of epidermis: In this work, while computing backscatter coefficients of dermis and fat tissues, compensation for intervening attenuation was done by assuming that the attenuation coefficient of epidermis is the same as that of the dermis. The effect of making such an assumption can be estimated to first order from the in vitro data of attenuation coefficients of epidermis and dermis by Moran et al [21]. From their results, at a frequency of 26 MHz, the ratio in attenuation between epidermis and dermis for a round trip distance of 0.3 mm (approximately twice the epidermal thickness at the forearm) is calculated to be 0.93 dB or a factor of about 1.24. This indicates that the backscatter coefficients of the dermis and fat reported in this work could be lower than the true value by about 24%. Efforts to determine attenuation and backscatter coefficients of the epidermis at the fingertip were not successful with the present system due to the presence of gross inhomogeneities in the epidermis. Figure 3.13 shows B-scan images of the fingertip of two subjects. Notable is the presence of an interface below the surface and above the dermis, most probably corresponding to the transition from the stratum corneum to the viable epidermis [81]. While it is possible to separate the sub-layers in B-scan images, efforts to separate them for tissue characterization were not successful with the present system due to finite pulse length and the requirement of several windows free of interfaces within each layer to compute attenuation (and therefore backscatter) coefficients. The epidermis is best studied using much higher frequency systems (e.g. 100 MHz) with shorter pulses.

(b) Hydration effects: Since water is used as a coupling medium in the experiments, hydration effects are possible during the time of the experiment (about 6 minutes). The effect of the hydration on the attenuation and backscatter coefficients cannot be quantified at present but presumably due to the barrier function of the stratum corneum in the epidermis [120], such effects are limited to only the superficial layers in the skin, and the dermis and fat are not affected very much. Such effects can also be reduced in future studies by using a faster imaging system.

3.4.5 Implications to tissue characterization

At present excision-biopsy is the gold standard for analysis of skin lesions such as suspected skin tumors. This is a time-consuming and expensive practice, especially as the majority of skin lesions are benign. High frequency ultrasound is a promising technique for evaluating skin due to its ability to penetrate deep tissues (several mm), its low-cost, and non-invasiveness. Tissue characterization parameters such as attenuation and backscatter coefficients have the potential to

aid classification and differentiation between normal and abnormal skin tissues, as well as between benign and malignant tissues. The computation of such parameters for normal skin tissues in vivo is an important step in that direction. Future studies would deal with the evaluation of such parameters for specific skin lesions. Moreover other parameters such as speckle statistics, doppler, and elasticity may have the potential for providing useful information for the evaluation of skin lesions and are worth being investigated in further studies. The epidermis could also be studied using much higher frequency systems.

4 Echo Envelope Statistics of Normal Skin Tissues[4]

4.1 Introduction

One approach for obtaining additional information for characterizing tissues using ultrasound is to analyze the statistical fluctuations of the backscattered signals. Ultrasonic signals can be modeled as stochastic signals since the precise details of the scattering structures in tissues, and consequently the details of the backscattered signals, are not known a priori. Support for this type of stochastic modeling comes from the fact that the ultrasound images of soft tissues have a random interference pattern called speckle, similar to the appearance of a rough surface irradiated by a coherent laser source. In ultrasound, speckle has both been considered as an unwanted effect that must be minimized using speckle-reduction techniques, or as an information-carrying phenomenon that can be exploited in tissue characterization. In this chapter we adopt the latter methodology to characterize skin tissues. In prior studies, the first order statistics of the amplitude of backscattered signals from several tissues such as the liver [121, 122], heart [123-125], breast [126], eye [57], and kidney [42] have been studied. Parameters related to amplitude statistics such as the scatterer number density [36, 42] and its frequency dependence [127] have also been studied for their potential for tissue characterization. Moreover second order statistics have also been studied [128]. Much of the theoretical background for such studies was obtained from earlier works in other fields such as optics, radar, and communications.

Until now, the statistical distributions of the envelope of backscattered signals from skin tissues have not been studied. The type of probability distribution of the envelope signals, and their parameters, could contain potential information regarding tissue microstructure that could be exploited for tissue characterization. In this work, we study the capability of six different probability distributions (Rayleigh, Rician, K, Nakagami, Weibull, and Generalized Gamma) to model statistics of envelope of backscattered data collected from the skin of several human volunteers in vivo using the Kolmogorov-Smirnov (KS) statistic as a goodness of fit measure. We also study the variability in parameter estimates and compare inter- and intra-subject variability. This is important as a large variability in the estimates might limit the capability of the parameters for tissue characterization and methods to reduce such variability should be pursued. Finally the

[4] This chapter uses material from an article accepted for publication in the *IEEE Transactions on Ultrasonics, Ferroelectrics, and Frequency Control*: B. I. Raju and M. A. Srinivasan, "Statistics of envelope of high frequency ultrasonic backscatter from human skin in vivo".

capability of the parameters to differentiate different skin tissues (dermis vs. fat, forearm dermis vs. fingertip dermis) is also studied.

4.2 Probability density functions

The signal received by an ultrasound transducer can be modeled as a phasor sum of the returns from several scatterers within the resolution cell of the system:

$$re^{j\psi} = \sum_{i=1}^{n} a_i e^{j\theta_i} \tag{4.1}$$

where a_i's are the amplitudes of signals scattered from the individual scatterers, which in turn depend on the shape, size and acoustical properties of the scatterers and the surrounding medium, and the θ_i's depend on the position of the scatterers. Since the precise details regarding the scattering cross-sections of the individual scatterers are unknown, the a_i's are modeled as random variables. Also since the locations of the scatterers are unknown, the θ_i's are also modeled as random variables. Moreover n, the number of scatterers contributing to the resultant, can also be a random quantity in general. Hence the resultant amplitude r is also a random quantity that can be described using probability density functions (pdfs). It should be pointed out that the model presented in Eq. (4.1) is an idealized one since realistic scattering occurs continuously throughout the tissue and not at discrete points. Nevertheless, it provides a convenient starting point for analysis. Even with this simplified model, it is generally difficult to obtain the exact pdf of the amplitude r except when n is small, and the θ_i's are assumed to be uniformly distributed between 0 and 2π [129]. In practice several well-known distributions are employed to describe the pdf of r and their appropriateness is evaluated using goodness of fit measures. In making such a description, one desires that the distribution fits empirical data well and is sufficiently rich enough to model a variety of scattering conditions. With the aim of determining the pdf that best models backscatter data from skin tissues, six probability distributions summarized below were studied in this work. Expressions for their pdfs, denoted as $p(r)$, and their cumulative distribution functions (cdfs), denoted as $F(r)$, are also given. The expressions for the cdfs were used in computing the KS goodness of fit measures. Also mentioned are the bounds on the ratio of the mean to standard deviation, denoted as SNR.

4.2.1 Rayleigh distribution

The Rayleigh distribution [130] results as a consequence of the central limit theorem, when the scattering medium contains a large number of randomly distributed scatterers (θ_i's uniformly distributed between 0 and 2π). This is a consequence of the application of the central limit theorem to the random phase summation problem. The Rayleigh distribution can also result if the individual scattering amplitudes a_i in Eq. (4.1) are themselves Rayleigh distributed even for finite n. Its pdf and cdf are given by

$$p(r) = \frac{r}{\sigma^2} e^{-\left(\frac{r^2}{2\sigma^2}\right)} \qquad r \geq 0;\ \sigma > 0 \tag{4.2}$$

$$F(r) = 1 - e^{-\left(\frac{r^2}{2\sigma^2}\right)} \tag{4.3}$$

It is instructive to present a brief derivation of the Rayleigh pdf using the central limit theorem. From Eq. (4.1), the real and imaginary parts of the resultant phasor are given by

$$\begin{aligned} A_R &= a_1 \cos(\theta_i) + a_2 \cos(\theta_2) + \ldots + a_N \cos(\theta_N) \\ A_I &= a_1 \sin(\theta_i) + a_2 \sin(\theta_2) + \ldots + a_N \sin(\theta_N) \end{aligned} \tag{4.4}$$

When n is large, the distribution of both A_R and A_I approach Gaussian with zero mean and variance $\sigma^2 = \frac{n\,E(a^2)}{2}$ where $E(.)$ indicates the expectation operator. This follows directly from the fact that the θ_i's are uniformly distributed between 0 and 2π and are independent of one another. Moreover it is easy to show that A_R and A_I are uncorrelated and jointly Gaussian with a joint pdf given by

$$p(A_R, A_I) = \frac{1}{2\pi\sigma^2} e^{-\left(\frac{A_r^2 + A_I^2}{2\sigma^2}\right)} \tag{4.5}$$

To evaluate the pdf of the amplitude of the resultant phasor $r = \sqrt{A_R^2 + A_I^2}$, a transformation to polar coordinates is made:

$$p(r, \psi) = \frac{r}{2\pi\sigma^2} e^{-\left(\frac{r^2}{2\sigma^2}\right)} \tag{4.6}$$

where ψ is the phase of the resultant phasor. The pdf of r can be now be obtained by integrating the above expression over all ψ. Since ψ can be seen to be uniformly distributed between 0 and

2π, a straightforward integration of Eq. (4.6) over ψ gives the Rayleigh pdf for r in Eq. (4.2). For this distribution, the SNR is equal to 1.91. When conditions leading to Rayleigh statistics are present, the B-scan images of the tissue show a speckle pattern that is often referred to as *fully-developed speckle.*

4.2.2 Rician distribution

The Rician distribution [131] results if in addition to conditions leading to the Rayleigh distribution, a specular or unresolved coherent component exists yielding the following pdf and cdf for the amplitude of the resultant phasor:

$$p(r) = \frac{r}{\sigma^2} e^{-\left(\frac{r^2+s^2}{2\sigma^2}\right)} I_0\left(\frac{sr}{\sigma^2}\right) \qquad r \geq 0;\ s \geq 0, \sigma > 0 \qquad (4.7)$$

$$F(r) = 1 - Q_1\left(\frac{s}{\sigma}, \frac{r}{\sigma}\right) \qquad (4.8)$$

where $I_0(x)$ is the modified Bessel function of the first kind of order 0, Q_1 is the Marcum Q function [132], and s is the amplitude of the coherent term. The Rician distribution includes the Rayleigh distribution as a special case for $s = 0$. The SNR for the Rayleigh distribution is ≥ 1.91. The term *post-Rayleigh* is sometimes used to refer to conditions leading to Rician statistics.

4.2.3 K distribution

The K distribution [45] results when the θ_i's are distributed uniformly between 0 and 2π, and the number of scatterers is random and follows negative binomial statistics, provided the mean number of scatterers is large. This distribution also arises if the individual scattering amplitudes a_i's are themselves K distributed even for finite *N*. The pdf and cdf are given by

$$p(r) = 2\left(\frac{r}{2}\right)^{\alpha} \frac{b^{\alpha+1}}{\Gamma(\alpha)} K_{\alpha-1}(br) \quad r \geq 0;\ \alpha, b > 0 \qquad (4.9)$$

$$F(r) = 1 - \frac{2}{\Gamma(\alpha)}\left(\frac{br}{2}\right)^{\alpha} K_{\alpha}(br) \qquad (4.10)$$

where α and b are the shape and scale parameters respectively, $\Gamma(\alpha)$ is the gamma function, and $K_\alpha(x)$ is the modified Bessel function of the second kind of order α. The relationship between the Rayleigh and K distributions was given by Jakeman and Tough [133], who showed that a Rayleigh process with non-constant second-moments is K distributed. Thus variations in scattering cross-sections of the individual scatterers tend to lead to deviations from the Rayleigh distribution to the K distribution. The K distribution has an SNR ≤ 1.91 and includes the Rayleigh distribution as a special case for $\alpha = \infty$. The term *pre-Rayleigh* is sometimes used to refer to conditions where the number density of the scatterers is not large enough to lead to the Rayleigh distribution. The K distribution is thus one example of a pre-Rayleigh distribution.

4.2.4 Nakagami distribution

The Nakagami distribution, first derived by Nakagami [47] based on his large-scale observations in high-frequency long-distance radio propagation, has the following expressions for the pdf and cdf:

$$p(r) = \frac{2m^m}{\Gamma(m)\Omega^m} r^{(2m-1)} e^{-\left(\frac{mr^2}{\Omega}\right)} \quad r \geq 0;\ m, \Omega > 0 \tag{4.11}$$

$$F(r) = \Gamma_{\text{inc}}\left(m, \frac{mr^2}{\Omega}\right) \tag{4.12}$$

where m and Ω are the shape and scale parameters respectively, and $\Gamma_{\text{inc}}(m,x)$ is the incomplete gamma function. Although derived empirically, theoretical justifications for encountering this type of distribution were provided by Yacoub [134] based on the observation that the power of a Nakagami distributed signal is the same as that of another signal composed of the incoherent sum of several Rayleigh signals. For example, if signals from two Rayleigh regions are added coherently, then the sum has a Rayleigh envelope. However, if these signals are added incoherently (powers added rather than instantaneous amplitudes), the resultant power is the sum of two exponential random variables, which is gamma distributed, in which case the amplitude is Nakagami distributed. Thus the Nakagami signal can be understood to be composed of clusters of waves added incoherently, for which within any one cluster the resultant obeys Rayleigh statistics, and the clusters are randomly distributed resulting in the incoherent addition of the resultants. In an ultrasound context, Shankar [135] showed that the Nakagami distribution could model a variety of conditions including pre-Rayleigh, Rayleigh, and post-Rayleigh conditions and can be useful in modeling backscatter signals from the human breast [126]. The

Nakagami distribution includes the Rayleigh distribution as a special case $(m=1)$ and approximates the Rician distribution for $m>1$. The distribution can model pre-Rayleigh, Rayleigh and post-Rayleigh conditions and its SNR can take any positive value.

4.2.5 Weibull distribution

The Weibull distribution was first proposed in the context of reliability engineering [136] and is described by the following pdf and cdf:

$$p(r)=\frac{b}{a}\left(\frac{r}{a}\right)^{b-1} e^{-\left(\frac{r}{a}\right)^{b}} \quad r\geq 0;\ a,b>0 \tag{4.13}$$

$$F(r)=1-e^{-\left(\frac{r}{a}\right)^{b}} \tag{4.14}$$

where, b and a are the shape and scale parameters respectively. Good evidence for this distribution has been observed in modeling radar clutter signals [137]. No theoretical explanation seems to be available for encountering this type of distribution. However the fact that this distribution can model pre-Rayleigh, Rayleigh and post-Raleigh conditions can be seen from the relationship between the SNR and the shape parameter b:

$$\text{SNR}=\frac{\Gamma\left(1+\frac{1}{b}\right)}{\sqrt{\Gamma\left(1+\frac{2}{b}\right)-\Gamma^{2}\left(1+\frac{1}{b}\right)}} \tag{4.15}$$

The SNR monotonically increases with b, with $0<b<2$ corresponding to pre-Rayleigh $(\text{SNR}<1.91)$, $b=2$ corresponding to Rayleigh $(SNR=1.91)$, and $b>2$ corresponding to post-Rayleigh or Rician $(SNR>1.91)$ conditions. The primary reason for including this distribution in this study is that the functional form of its pdf is different from that of the other distributions such as the K and the Nakagami distributions, thereby increasing the search space of appropriate distributions for skin tissues. The SNR of the Weibull distribution can take any positive value.

4.2.6 Generalized Gamma distribution

The generalized gamma distribution, hereafter referred to as the GG distribution, was introduced by Stacy [138] and is a three parameter distribution whose pdf and cdf are given by

$$p(r) = \frac{cr^{(c\nu-1)}}{a^{c\nu}\Gamma(\nu)} e^{-\left(\frac{r}{a}\right)^c} \quad r \geq 0;\ a,\nu,c > 0 \tag{4.16}$$

$$F(r) = \Gamma_{\text{inc}}\left(\nu, \left(\frac{r}{a}\right)^c\right) \tag{4.17}$$

where, c and ν are two shape parameters that provide flexibility in adjusting the shape of the pdf, a is the scale parameter, and $\Gamma_{\text{inc}}(m,x)$ is the incomplete gamma function. This distribution has previously been found to be useful in modeling the fading of signals in a mobile radio environment [139]. Recently, while the present work was under review, Shankar [89] independently proposed the use of this distribution to model ultrasound envelope signals. The GG distribution is especially attractive since it contains several distributions as special cases: Rayleigh (c=2 and ν=1), exponential (c=1 and ν=1), Nakagami (c=2), Weibull (ν=1), and also the usual gamma (c=1) distribution. The lognormal distribution also arises as a limiting case when ν approaches ∞. Moreover the GG distribution provides two parameters for tissue characterization instead of at most one for all the other distributions. It is also interesting to note that if r is GG distributed, so is r^2 and hence the GG distribution can be used for modeling both the amplitude and intensity fluctuations.

For the sake of completeness we also mention some other distributions that have been studied in the literature: the Generalized-Rician [41, 140], the Homodyned-K [37], and the Generalized-K distributions [133]. They were not used in this study because the simpler Nakagami distribution can model conditions leading to the above distributions [135].

4.3 Methods

4.3.1 Experimental system

The experimental system and data acquisition procedure are described in detail elsewhere [92] and only brief details will be given here. The system consisted of a PVDF transducer (Panametrics, Waltham, MA; Model PI50), a pulser/receiver (Panametrics; Model PR5900), a

digitizing oscilloscope sampling at 500 MHz (Tektronix, Beaverton, OR; Model TDS 520C), and a 3-axis scanning system (Parker Hannifin/Compumotor, Cleveland, OH). The characteristics of the transducer used in this study are shown in Table 2.1. A PC was used to control both mechanical scanning and GPIB-based data acquisition. By averaging 100 repeated acquisitions, the signal-to-noise ratio of each echo sequence was vastly improved. This approach was especially useful to record signals from subcutaneous fat, which were considerably weaker than those from the dermis. The scanning system had encoders on the x and y-axes that enabled the transducers to be positioned with an accuracy of 1 μm. Echo sequences were collected from 25 independent lateral locations of the transducers by scanning along x and y axes over an area of 1.5 mm x 1.5 mm in a 5 by 5 raster format. The stepping distance of 0.3 mm was larger than the lateral resolution of the system (0.1 mm). Since the transducer was well focused, diffraction effects could lead to signal variations with depth. Therefore the transducer was axially translated to focus at a desired depth, while data were recorded from the location of the focal zone. Once the raw data were collected, further analyses were done off-line on a PC.

4.3.2 Human subjects and tissues

In most parts of the body, the skin consists of a thin layer of epidermis (0.15 mm thick) and a thicker underlying layer of dermis (1.2-1.8 mm thick). The region beneath the dermis consists of subcutaneous fat, which is sometimes considered as a third layer of the skin and referred to as the hypodermis. In the palms and soles, the skin is vastly different from that at other locations. Notably, the epidermal thickness is much larger (about 0.6 mm) in these regions due to the increased thickness of the stratum corneum, the dead layer of cells. In this work, data were collected from the dorsal side of forearm skin (close to the wrist) as well as the tip of the left index finger on the palmar side. Since skin conditions could depend on age, the study was restricted to only young adults. Eighteen subjects aged between 20-36 (median = 26) were used. In the case of the forearm region, both the dermis and subcutaneous fat tissues were studied whereas at the fingertip only the dermis was studied, as the signals from subcutaneous fat at this region were close to the noise level. At the forearm, data collected when the focal zone was at 0.6 mm below the surface were taken to correspond to the dermis while data collected when the focal zone was located at 2.4 mm below the surface were considered to correspond to fat. Occasionally for some subjects when fibrous septae were seen to be present in the fat at a depth of 2.4 mm (identified as hyperechoic structures within a relatively hypoechoic fat), another depth between 1.8–3.0 mm was used to extract data corresponding to fat. In the case of the fingertip, data

collected when the focal zone was at 1.05 mm below the surface were taken to correspond to the dermis. For each of the experiments, a second independent repetition at a close-by region (displaced by a few mm from the original site) was done to increase the number of independent samples. In order to study intra-subject variability and compare it with inter-subject variability, 18 repetitions of the experiment were done for 1 subject (male, 28 years) at the fingertip region. Water was used a coupling medium between the transducer and the tissue. During imaging, the forearm was held steady on a table using Velcro straps. The fingertip was kept steady using custom-made finger splints. All the subjects who participated in the study signed an informed consent document approved by the Institutional Review Board of the Massachusetts Institute of Technology.

4.3.3 Determination of empirical probability density functions

Once echo sequences were recorded, the Hilbert transform approach was used to obtain envelope signals. Sixteen independent samples of the envelope all lying within the focal zone region were extracted from a particular echo sequence by picking every eighteenth sample. Assuming a speed of sound of 1.5 $mm/\mu s$ in skin, the spacing between the extracted samples was 27 μm, which was larger than the axial resolution of the transducer (25 μm). Also the total length of 405 μm spanned by all the 16 axial samples was considerably smaller than the –6 dB depth-of-focus of the transducer (1.3 mm). With 16 samples per echo sequence, 25 such echo sequences through lateral scanning (the transducer was focused at one specific depth, e.g. 0.6 mm below the surface for the case of the dermis for all the 25 echo sequences), and 2 repetitions of the experiment, a total of 800 samples were available to construct empirical histograms. Before combining the samples in the above manner, compensation for attenuation within the 405 μm distance was done by assuming attenuation coefficient slopes of 0.21, 0.18 and 0.33 dB/mm/MHz for the forearm dermis, forearm fat, and fingertip dermis respectively [92]. Also, occasional specular reflectors, e.g., fibrous septae in subcutaneous fat were eliminated prior to analysis to the extent possible. Such occasional specular reflectors would make the results more pre-Rayleigh than the ones reported in this work [41] and were removed because they were considered extraneous to the tissue of interest. These occasional high peaks were considered to be outliers if their amplitudes were very far from the median of all the samples. A distance of four times the inter-quartile range (IQR) from the median was used as a cut off to categorize these samples as outliers. Median and IQR were used (instead of mean and SD), as they are much less affected by the presence of outliers. The reason for choosing 4 times the IQR was that further reduction in the cut-off

distance did not change the statistics appreciably. It is a matter of personal judgment whether to include or eliminate these samples. It is reasonable to consider that the *occasional* large peaks were extraneous to the tissue of interest and therefore could be eliminated.

4.3.4 Estimation of the parameters

Estimation of the parameters of all the six distributions was done using the maximum likelihood (ML) method, in which the set of parameters that maximizes the likelihood function or its logarithm is determined. In the case of the Rayleigh distribution, the ML parameter was obtained using a closed-form expression:

$$\hat{\sigma}^2_{ML} = \frac{E(r^2)}{2} \tag{4.18}$$

In the above and following equations, $E(x)$ represents the mean of the random variable x, and is taken to be equal to the sample mean. For distributions other than Rayleigh, simple closed-form solutions for the parameters do not exist, and the ML procedure was implemented as an optimization problem that sought to determine parameters that maximized the log-likelihood function. The optimization procedure was implemented using the Nelder-Mead Simplex method [141] available in the Matlab optimization toolbox (The Math Works Inc., Natick, MA). This method does not require the computation of derivatives but requires an initial guess of the solution. The initial guesses of the parameters (denoted with subscript 0 in this paper) were obtained using the method of moments as described below. For the Rician, K, and Nakagami distributions, the initial guesses were obtained using estimated second and fourth moments of the data. For the Rician distribution we have,

$$s_0 = \sqrt[4]{2\left[E(r^2)\right]^2 - E(r^4)} \tag{4.19}$$

$$\sigma_0 = \sqrt{\frac{E(r^2) - s_0^2}{2}} \tag{4.20}$$

For the K distribution we have,

$$\alpha_0 = \frac{2}{\frac{E(r^4)}{\left[E(r^2)\right]^2} - 2} \tag{4.21}$$

$$b_0 = \sqrt{\frac{4\alpha_0}{E(r^2)}} \tag{4.22}$$

And for the Nakagami distribution the initial guesses were obtained as,

$$m_0 = \frac{\left[E(r^2)\right]^2}{E(r^4) - [E(r^2)]^2} \tag{4.23}$$

$$\Omega_0 = E(r^2) \tag{4.24}$$

Under some conditions, the above equations for the Rician and K distributions do not yield meaningful solutions. For instance, if the data were truly pre-Rayleigh distributed (e.g., K distributed), the computed value of s_0 would be complex. This was indeed the case for almost all of the data obtained (see Results section). The ML procedure for the Rician distribution was implemented by assuming the initial guess s_0 to be a small positive quantity, equal to 0.1. On the other hand if the data were truly Rician distributed, the computed value of α_0 would be negative. However no such problem was seen for all the data sets analyzed in this paper.

For the Weibull distribution, an iterative procedure was used to compute the initial guess b_0 by solving the following equation:

$$\frac{\Gamma\left(1+\frac{2}{b_0}\right)}{\Gamma^2\left(1+\frac{1}{b_0}\right)} = \frac{E(r^2)}{\left[E(r)\right]^2} \tag{4.25}$$

Figure 4.1 shows a plot of the LHS of the above equation as a function of b_0. A monotonic relationship is seen, and therefore a unique solution exists for b_0 for a given value of the RHS. The solution was obtained using a look-up table containing pre-computed values of the LHS as a function of finely spaced b_0 (accuracy of estimate was 0.005 in the range $1 \le b_0 \le 2$ where the solution was found for the data sets in this work). Once b_0 was obtained, a_0 was obtained from the following expression:

$$a_0 = \frac{E(r)}{\Gamma\left[1+\frac{1}{b_0}\right]} \tag{4.26}$$

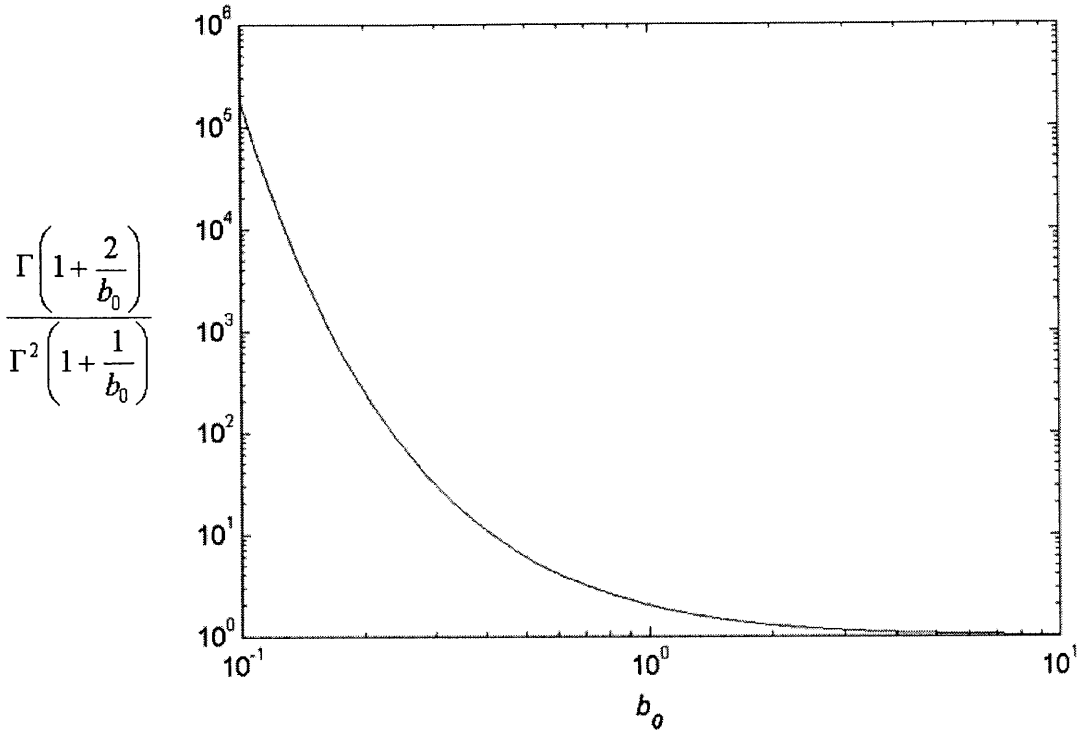

Figure 4.1: Computation of the initial guess for the Weibull-*b* parameter. The graph shows the LHS of Eq. (4.25) as a function of b_0.

For the GG distribution, the initial guesses for the parameters were obtained using the moments of logarithm of data as proposed by Stacy and Mihram [142]:

$$\frac{\psi''(\nu_0)}{[\psi'(\nu_0)]^{1.5}} = -\left| \frac{E\left[\left(\ln(r)-\overline{\ln(r)}\right)^3\right]}{\left\{E\left[\left(\ln(r)-\overline{\ln(r)}\right)^2\right]\right\}^{1.5}} \right| \tag{4.27}$$

$$c_0 = \sqrt{\frac{\psi'(\nu_0)}{E\left[\left(\ln(r)-\overline{\ln(r)}\right)^2\right]}} \tag{4.28}$$

$$a_0 = E(r)\frac{\Gamma(\nu_0)}{\Gamma\left(\nu_0+\frac{1}{c_0}\right)} \tag{4.29}$$

In the above equation $\psi^n(\nu) = \frac{d^{n+1}}{d\nu^{n+1}}\ln[\Gamma(\nu)]$ is the polygamma function, which was evaluated using the *polygamma* function in Matlab's Symbolic Toolbox. At first ν_0 was obtained by

solving Eq. (4.27), where the RHS of this equation is the skewness of the logarithm of the data. Figure 4.2 shows a plot of the LHS of this equation as a function of ν_0. It can be seen that this function is monotonic, and hence a unique solution for ν_0 exists as long as the RHS is between -2 and 0, which was the case for all the data sets analyzed in this work. A look-up table with pre-computed values of the LHS as a function of ν_0 was used for this purpose (accuracy of estimate was 0.005 for the values estimated in this work). Once ν_0 was obtained, the value of c_0 was then obtained using Eq. (4.28), and subsequently the value of a_0 was then obtained using Eq. (4.29).

Once the initial guesses of the parameters of the Rician, K, Nakagami, Weibull, and the generalized gamma distributions were obtained as described above, the ML estimation was implemented using the Nelder-Mead optimization technique. We note that there are other simpler methods to compute the parameters of some of the above distributions [143], including the use of fractional order moments [144]. However, in order to compare the capability of various distributions to model data from tissues, it is preferable to use the same method for estimating the parameters of all the distributions. Thus the ML method was used for estimating the parameters of all the distributions. Also the Nelder-Mead technique provided a uniform scheme to implement the ML method for the various distributions, although we note that alternate implementations of the ML method are also possible [145]. Additional optimization techniques employing Genetic Algorithms were also studied for their potential to estimate the parameters, especially for the Generalized Gamma pdf. However they performed poorly compared to the Nelder-Mead technique.

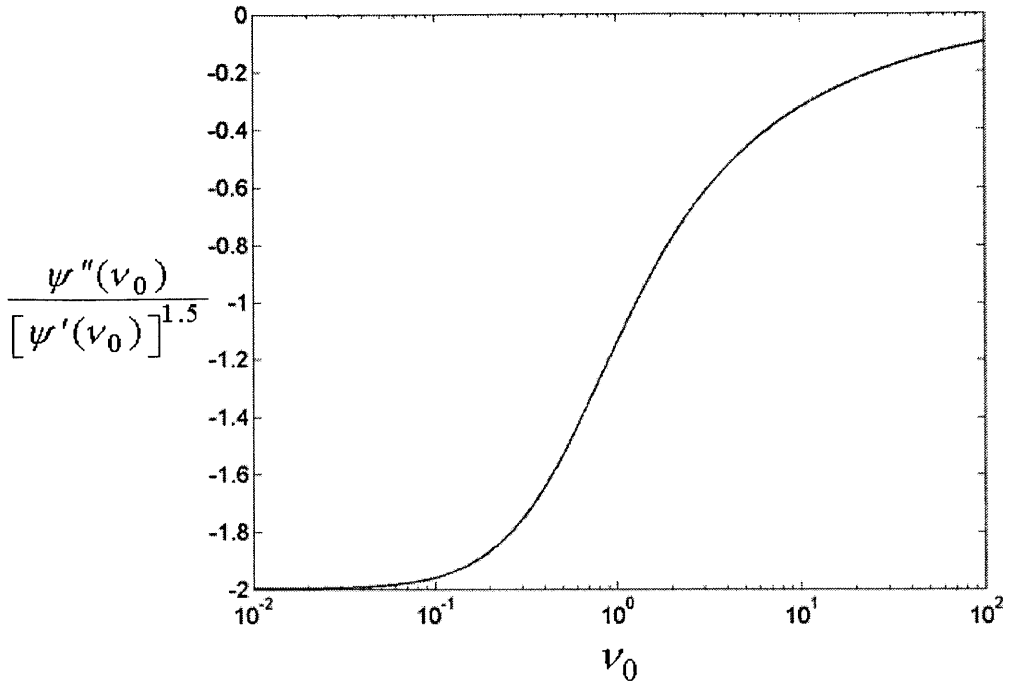

Figure 4.2: Computation of the initial guess for the GG-ν parameter. The graph shows the LHS of Eq. (4.27) as a function of the parameter ν_0.

4.3.5 Numerical issues

One issue in implementing the ML estimation procedure is that proper care is needed to prevent overflow problems while computing the log-likelihood functions. For example, the gamma function present in expressions for the pdfs of some of the distributions could easily overflow the maximum limit of most computers when its argument is large. However its logarithm has a much smaller value, and therefore while computing the log-likelihood functions, a direct evaluation of the logarithm of the gamma function was used. Also while computing the log-likelihood functions for the K distribution, the Bessel function $K_{\alpha-1}(x)$ could overflow the maximum limit of computers for small values of x. Hence an exponential approximation was used in such cases [146]:

$$K_{\alpha-1}(x) \simeq \frac{\Gamma(\alpha-1)}{2}\left(\frac{2}{x}\right)^{\alpha-1} \quad \text{for } x \ll \alpha-1 \tag{4.30}$$

The logarithm of the above function was evaluated directly without first computing the exponential, thereby avoiding numerical overflows.

4.3.6 Goodness of fit testing

The goodness of fit of each of the candidate distributions to the empirical distribution was evaluated using the KS goodness of fit measure, which is the maximum absolute difference between the fitted cdf and the empirical cdf [147]. A smaller value of the KS statistic indicates a better fit of the particular distribution to empirical data. For computing the fitted cdfs, the expressions given in Section II were used. The KS test also enables us to accept or reject the hypothesis that a particular distribution could model the empirical data for a chosen level of significance. For example, for a significance level of 0.01, in order to accept the model, the KS value should be less than (see Table A14 in [147])

$$D = \frac{1.63}{\sqrt{N}} \tag{4.31}$$

which, for a sample size of $N = 800$, is 0.0576.

4.3.7 Statistical tests

To study the capability of the parameters of the various distributions to differentiate different tissue types (dermis vs. fat; forearm dermis vs. fingertip dermis), the Wilcoxon sign rank test (without the normal approximation for the test statistic) was used. In this test, the two values being compared as taken as paired samples.

4.4 Results

4.4.1 Probability density function of amplitude of backscattered signals from skin tissues

Figure 4.3 shows typical pdf fits to empirical envelope data obtained at the forearm of a human subject in vivo, for all the six distributions. Figure 4.4 shows the corresponding cdf fits to the empirical cdf. The fits were obtained using the ML method for estimating the parameters with a sample size of 800. It can be seen that the GG pdf fitted the empirical histograms very well and had the smallest KS value (smallest cdf deviation from the empirical cdf) compared to the other distributions. The empirical histograms were pre-Rayleigh, and the Rayleigh and Rician distributions modeled the empirical histograms poorly compared to the other distributions. Also the best Rayleigh and Rician fits were almost the same, which is consistent with the fact that the best Rician fit to data that are pre-Rayleigh distributed is the Rayleigh fit. Other distributions,

especially the K and Weibull distributions also show good fits to the data. The empirical histogram for the case of fat was more pre-Rayleigh than that of the dermis.

Figure 4.5 shows the KS goodness of fit measures between each one of the six distributions and the empirical distribution for the case of the forearm dermis, forearm fat, and fingertip dermis. The GG distribution provided the best fit in a majority of cases, and on the average had the smallest KS statistic values. Next to the GG distribution, the K and Weibull distributions also provided good fits to the data as seen by the closeness of their KS values to that of the GG distribution. If a hypothesis test was undertaken at a significance level of 0.01 to accept or reject each of the models, the KS values should be less than $1.63/\sqrt{N}$, which for $N = 800$ is 0.0576. It can be seen from Fig. 4.5 that on the average, the GG, K and Weibull distributions would satisfy this criterion for all the three tissues. The Nakagami distribution, though better than the Rayleigh/Rician models did not fit the data as well as the GG, K and Weibull distributions. For all the data sets, the Rayleigh and Rician distributions gave poor fits to the data, because of which their parameters were not studied further.

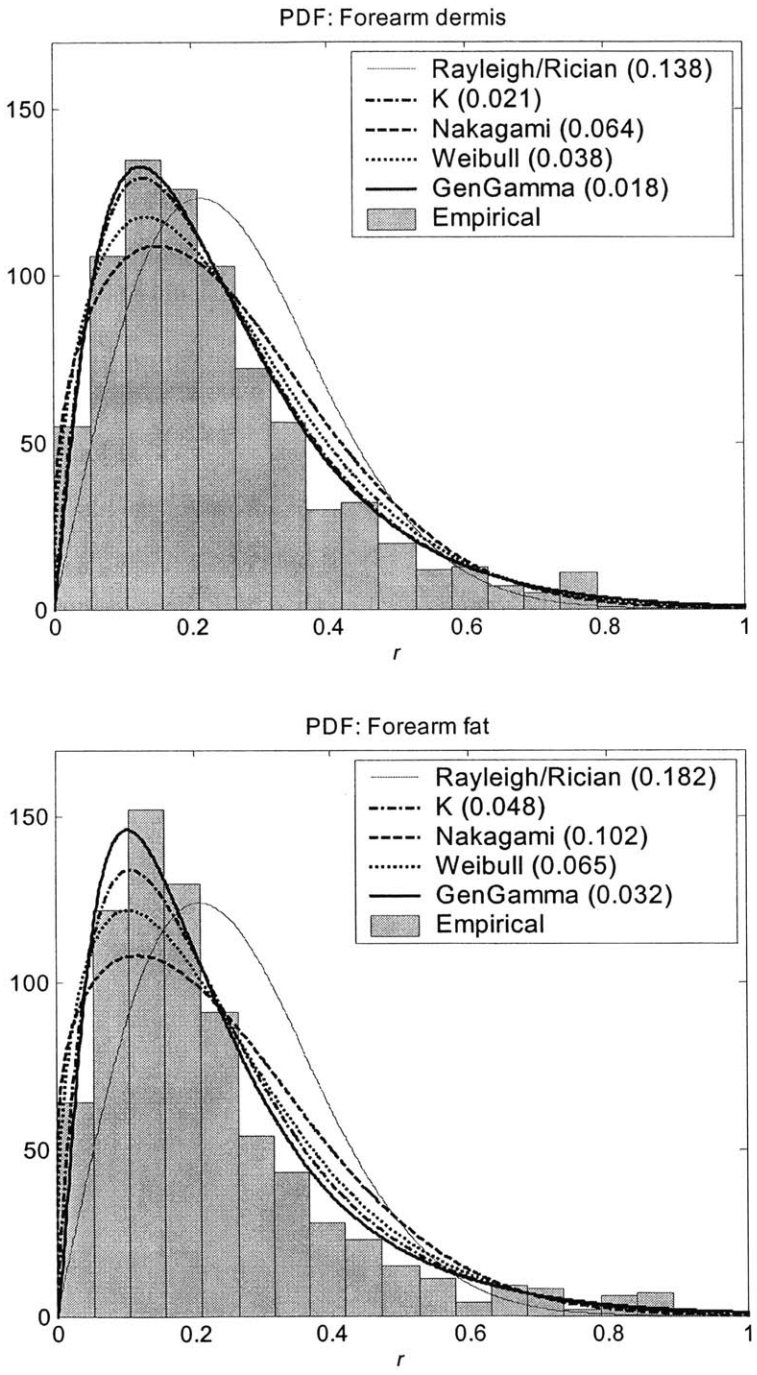

Figure 4.3: Fitting probability density functions to empirical data. The top figure corresponds to data from the forearm dermis and the bottom figure corresponds to data from the forearm fat. The pdf fits were scaled so that the area under the curves matched the total area under the histograms. The samples were normalized so that the maximum value was unity. The Rayleigh and Rician fits are co-linear. The values in the inset are the Kolmogorov-Smirnov goodness of fit values. See also Fig. 4.4.

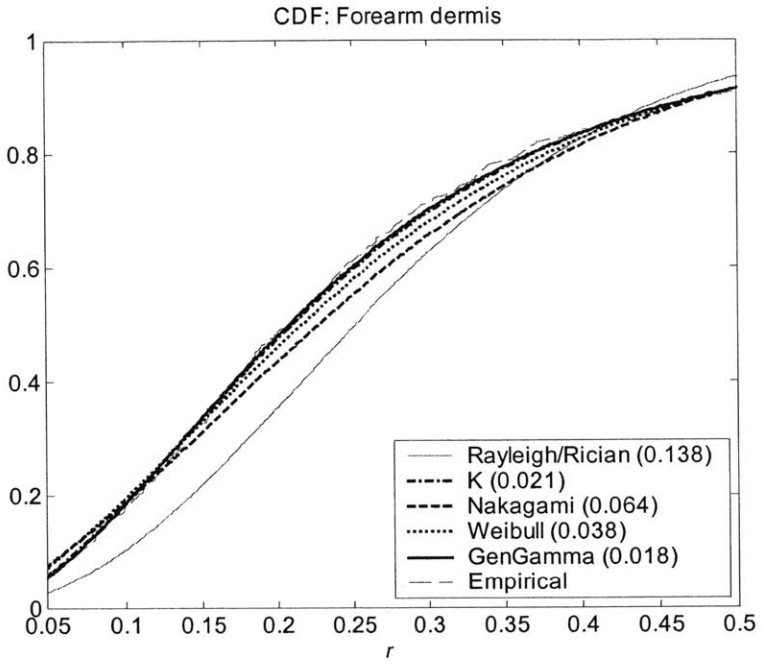

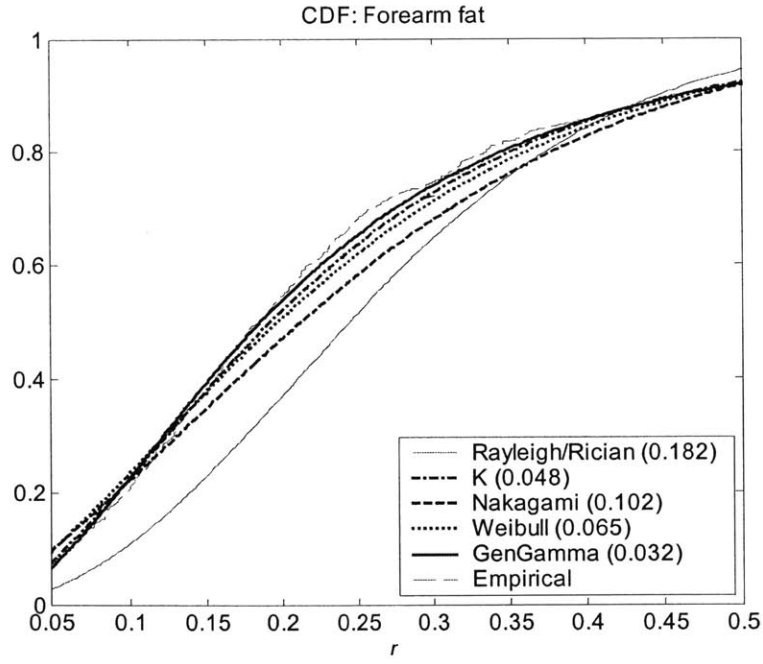

Figure 4.4: CDFs of the fitted distributions. Only portions of the data (0.05-0.50) are shown to illustrate the differences. The values in the inset are the Kolmogorov-Smirnov goodness of fit values. See also Fig. 4.3.

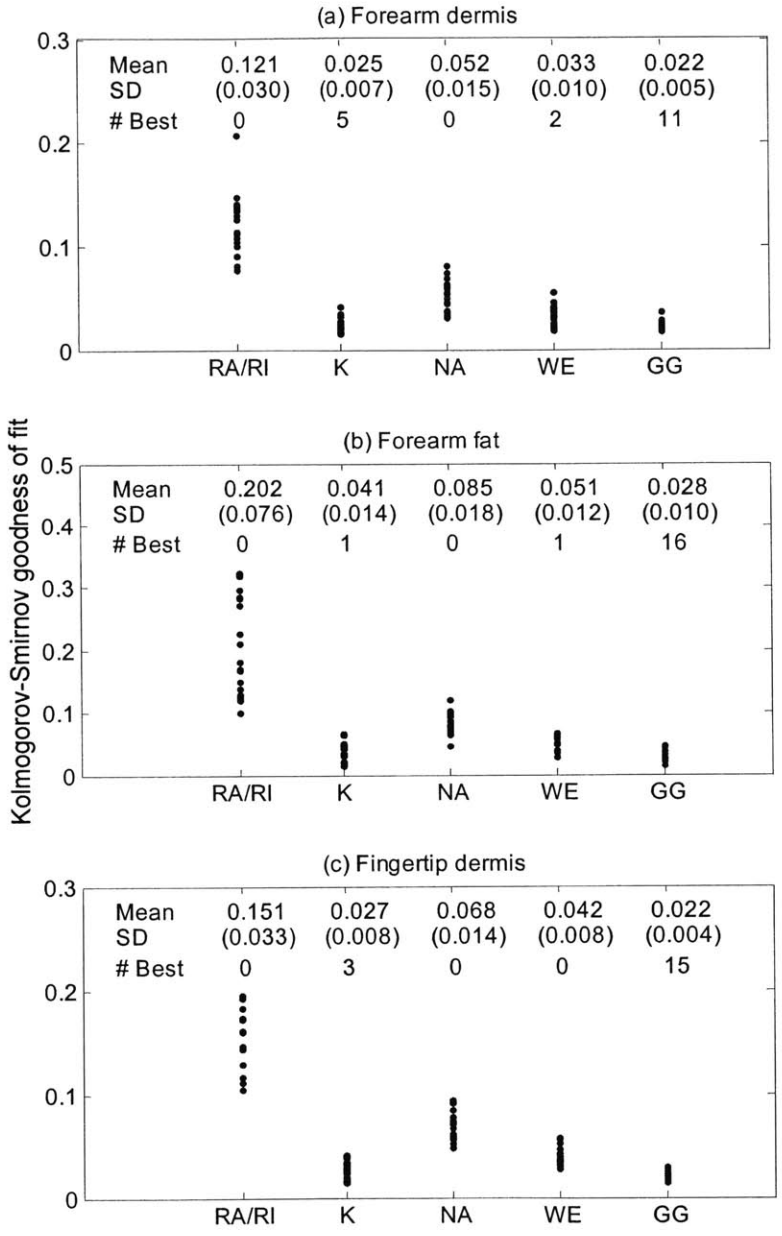

Figure 4.5: The KS goodness of fit measure between the empirical distribution and each of the 6 fitted distributions (RA-Rayleigh, RI-Rician, K-K, NA-Nakagami, WE-Weibull, GG-Generalized gamma) for the case of the dermis and fat at the forearm wrist and the dermis at the fingertip. Each dot corresponds to data from one particular subject. The mean, standard deviation (SD), and the number of subjects where the KS value of that particular distribution was the best (smallest), are indicated.

4.4.2 Inter-subject variability vs. intra-subject variability

Figure 4.6 shows a plot of the estimates of the SNR parameter and of the shape parameters of the K, Nakagami, Weibull, and the GG distributions for all the subjects and for 18 repetitions on the same subject. All the data were obtained at the fingertip. For both the inter- and intra-subject cases, the SNR and Weibull-*b* parameters showed smaller variability (5-7% of the mean) than the other parameters. The K and GG distribution parameters showed larger variability (17-43% of the mean). The Nakagami-*m* parameter showed about 9% variability with respect to the mean. For the SNR, Nakagami-*m*, and Weibull-*b* parameters, the percent variability was only marginally smaller for the inter-subject case than for the intra-subject case. Given that these parameters are positively biased, the smaller variability in the intra-subject case could be accounted for by the smaller mean values. In the case of the K-α and GG-*c* parameters, the percent variability was smaller for the intra-subject case, but once again these could be explained by the differences in mean values. For the GG-ν parameter the inter-subject variability was larger even though the means were comparable, but it is conceivable that the variability could have been lower than the intra-subject case if a couple of extreme values had been excluded (Fig. 4.6 (e)). These results suggest that the inter- and intra-subject variability in the parameter estimates are similar. Although the particular subject chosen for the intra-subject may not be characteristic of all subjects, the similarity in intra- and inter-subject variability indicates that reasons other than genuine inter-subject differences might be important and suggests further work for identifying and reducing variability.

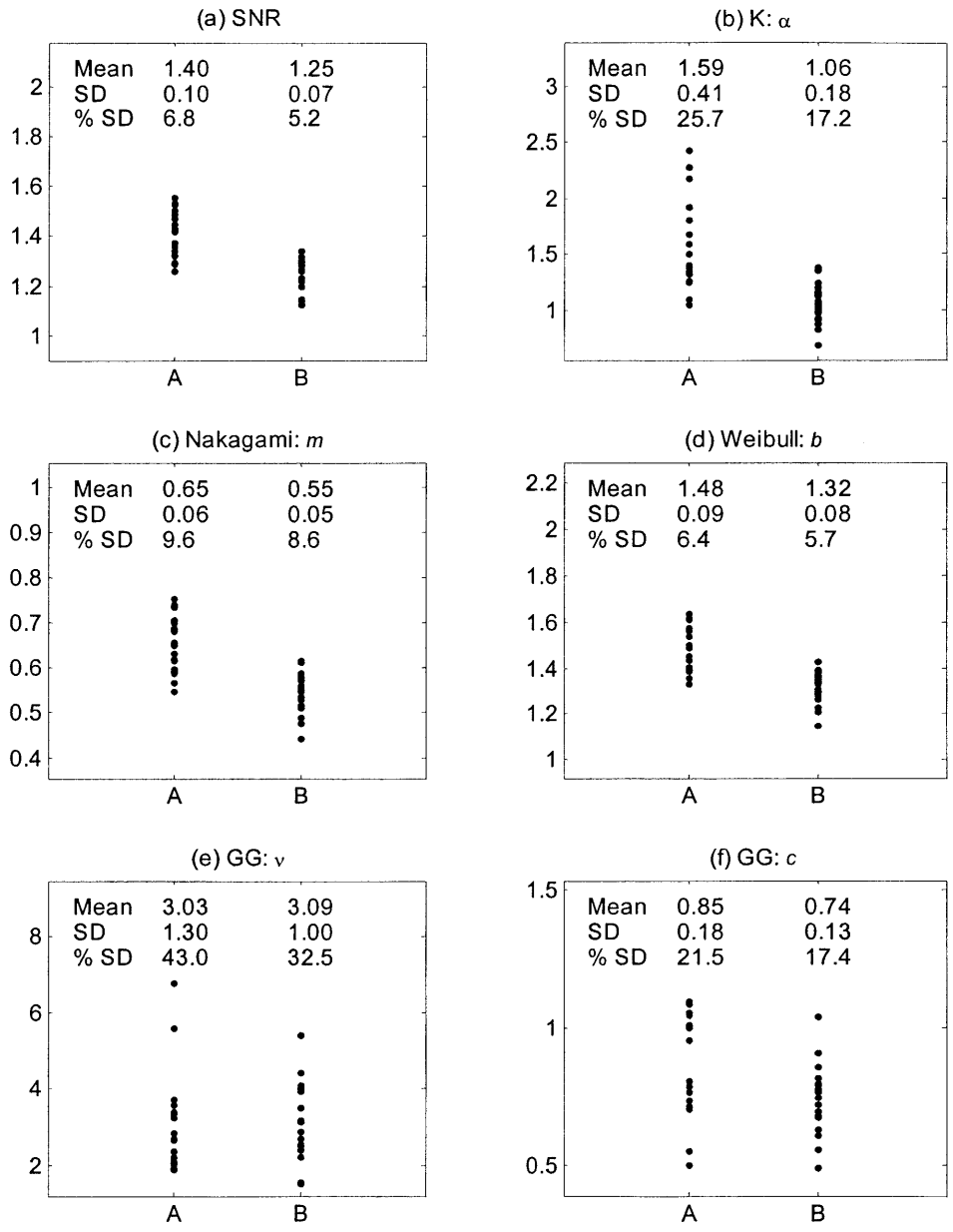

Figure 4.6: Comparison between inter-subject (A) and intra-subject (B) variability. The dots represent the estimated values for each subject or repetition. Numerical values for the mean (top row), the standard deviation (middle row), and the percentage variability defined as $\frac{\text{mean}}{\text{SD}} \times 100$ (bottom row) are also indicated.

4.4.3 Characterization of differences in tissues

The SNR parameter and the shape parameters of the K, Nakagami, Weibull and GG distributions were evaluated for their capability to differentiate between the dermis and fat at the forearm, and between the dermis at the forearm and fingertip regions. For this purpose the difference in the estimated parameters between the two tissues taken subject-wise were computed. The data to compare forearm dermis and fat were obtained from the same experiment in which the location of the transducer focal zone was axially shifted to focus first on the dermis and subsequently on fat. The data to compare the forearm and fingertip dermis were obtained from two separate experiments done one after the other at the two body-sites. From Fig. 4.7 it can be seen that the differences in parameter estimates between the dermis and fat was positive in a majority of the cases for SNR, K-α , Nakagami-*m*, Weibull-*b*, and GG-*c* parameters, and negative in a majority of cases for the GG-ν parameter. For all parameters, significant differences between the dermis and fat could be seen as indicated by low p-values. Between forearm dermis and fingertip dermis, a similar trend is seen but only the GG parameters showed significant differences at a 0.01 significance level. These results indicate that the GG-ν and GG-c parameters might be more capable of differentiating tissues than the other parameters.

4.5 Discussion

Skin is an easily accessible organ in the human body and is affected by a large number of lesions. With conventional ultrasound it is often difficult to distinguish between various lesions and hence additional quantitative studies might be useful. One such method is the use of envelope statistics. This study seems to be the first one on modeling the pdf of envelope signals from skin tissues. The statistics of envelope signals can provide additional information only if the statistics deviate from the Rayleigh behavior. If only Rayleigh statistics were present, no additional information other than the mean backscatter level can be used for tissue characterization. This study supports the hypothesis that non-Rayleigh, specifically pre-Rayleigh statistics are present in the case of skin tissues (at least for the specific transducer employed), which can therefore provide additional information for tissue characterization. The non-Rayleigh behavior cannot however automatically be ascribed to the small resolution cell sizes present in high frequency imaging systems. This is because tissues contain scatterers even at small length scales and the number of scatterers is not necessarily small for small resolution cell sizes. For example, collagen fibers, the dominant scatterers in the dermis, are themselves composed of smaller fibrils and microfibrils, all of which constitute scatterers ranging in size from tens of microns to tens of Angstroms [119, 148]. It is

likely that the variation in scatterer cross-sections is large enough to cause the effective number of scatterers within the resolution cell to be small, leading to pre-Rayleigh statistics. It should also be pointed out that the envelope statistics is not only dependent on the tissue being studied, but is also dependent on the imaging system used. When a less focused transducer (f/#=4, but similar frequency characteristics to the one reported in this work) was used, the mean estimated SNR values were about 9% larger for both the dermis and fat tissues (results based on this transducer not reported in this work). This is consistent with the fact that the resolution cell size is larger for a less focused transducer than a more focused transducer, leading to fewer pre-Rayleigh deviations.

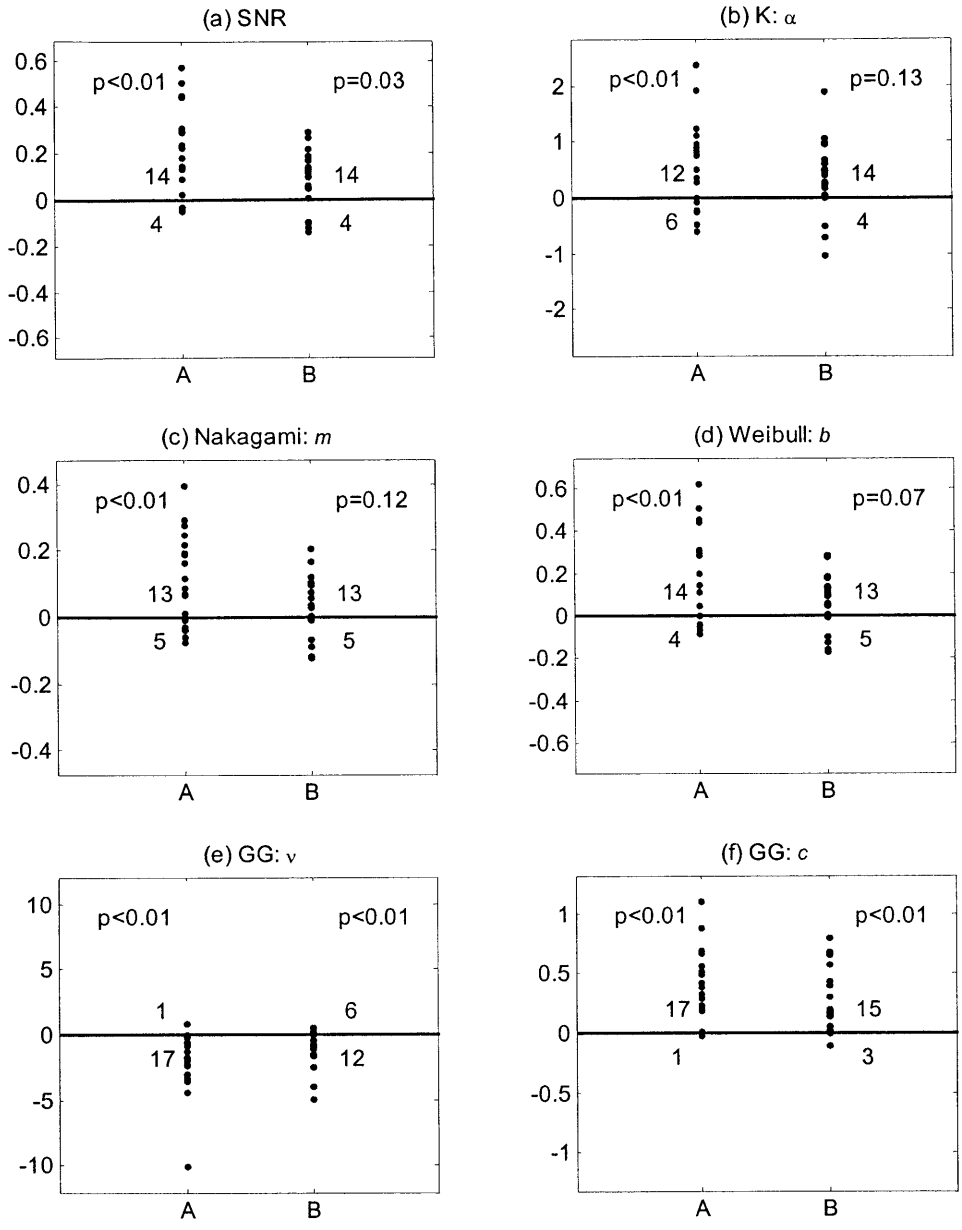

Figure 4.7: Differences in parameters between the dermis and fat at the forearm (A) and the dermis at the forearm and fingertip (B). Each data point is the difference in the respective estimated quantities. The number above and below the $y = 0$ line indicate the number of cases where the difference value was positive and negative respectively. The p-values based on a Wilcoxon sign rank test are also indicated.

Previous studies (involving other tissues) have rarely compared the performance of several distributions for modeling empirical data. Also, except for the recently published independent work by Shankar [89], the applicability of the GG distribution has not been studied in an ultrasound context. Our study shows that the GG distribution was able to fit the empirical envelope data from skin tissues better than all the other distributions. This is not surprising since the GG distribution has one additional parameter that makes it more flexible to tailor itself to empirical data as long as a sufficient sample size is available. It should however be noted that even among distributions that have the same number of parameters, some of them fit better than the others. For example, the K and Weibull distributions fit better than the Rician and Nakagami distributions even though all of them have two parameters, implying that the number of parameters does not solely determine the goodness of fit. Thus the better fit of the GG distribution is not merely because of having an additional parameter, but rather because of its ability to adjust its upper and lower tails independently with two shape parameters [89, 139]. Other distributions, especially the K and Weibull distributions were also able to model the envelope data well. In practice, the choice of an appropriate distribution will depend not only on the goodness of fit, but on other factors including the variability in the estimated parameters, the sample size available (which is related to the variability), and the capability of the estimated parameters to classify different tissues. Even though all the parameters were estimated using the same sample size, the GG-ν parameter showed larger percent variations than the other parameters. This would imply that in general a larger sample size would be necessary to estimate the GG parameters to a desired level of accuracy. Such variability issues regarding the GG distribution have been studied before, because of which the Weibull distribution has often been considered appropriate when the sample size is small [149]. The K distribution yielded very good goodness of fit measures, but showed more variability than the Weibull parameters. It is known that the K distribution becomes less useful when the true value of α is large, because the variance in the estimate becomes large [42]. The Weibull and Nakagami distributions do not have this difficulty. Between the Weibull and Nakagami distributions, the Weibull distribution outperformed the Nakagami distribution with better goodness of fits as well as smaller percent variability. It is likely that the Weibull and GG distributions might prove useful in modeling ultrasound echo signals when small and large sample sizes are available respectively.

One would expect the intra-subject variability in the parameters to be smaller than the inter-subject variability as additional differences from one subject to another could arise due to different skin conditioning, aging, or sun exposure. However, the intra-subject variability was

found to be similar to inter-subject variability for data collected at the fingertip. This indicates that any genuine variability between subjects is over-shadowed by other factors. One possible reason is the finite sample size used to estimate the parameters. Increasing the sample size could reduce variability but only at the loss of stationarity in tissue properties. Other possible factors include variations in ambient humidity, time to acclimatize to the ambient conditions, and diurnal changes associated with skin [150]. The fact that intra-subject variability is large indicates that for tissue characterization, data should preferably be acquired from both the suspected lesion and the adjoining normal skin tissue during the same experiment.

Dermis and fat are vastly different tissues. They can easily be differentiated using the absolute backscatter levels in the frequency range 20-50 MHz [92]. The present work supports the hypothesis that they can be differentiated using envelope statistics as well. This was despite the variability in the estimated parameters. Fat was seen to show more pre-Rayleigh behavior as shown by smaller SNR values. More deviation from Rayleigh to pre-Rayleigh is the result of more variations in the scattering cross-sections, or equivalently, smaller effective number of scatterers in fat. Such variations in fat tissue could be due to the presence of septa/fascia, adding to the inhomogeneity to the tissue. Between the dermis at the fingertip and forearm regions, only the GG parameters showed differences at a 0.01 significance level indicating that the GG distribution might be better suited in classifying skin tissues than other distributions (if a sufficient sample size is available). While computing the parameter estimates for the case of forearm fat, the effect of intervening attenuation (not the same as attenuation within the ROI) by the dermis, and to a lesser extent the much thinner epidermis, was not considered. The presence of intervening attenuation would tend to increase the size of the resolution cell thereby pushing the distributions closer to the Rayleigh distribution [151]. This would lead to larger estimates for parameters such as K-α, Nakagami-*m*, and Weibull-*b*. However even in the presence of intervening attenuation, the above parameters were found to be smaller for the case of fat than for the dermis. Intervening attenuation will also affect the parameters estimated at the fingertip dermis due to the thicker epidermis. Hence it is conceivable that the true estimates of the above parameters for the forearm fat and fingertip dermis are smaller than what was estimated. Such effects can be minimized using narrow-band filtering prior to estimation.

In fitting the pdfs to empirical data, only an overall goodness of fit measure (KS measure) was used. This measure however does not indicate the closeness of fit in different regions of the histogram, e.g. the lower tail, the body, or the upper tail. If sufficient data samples are available, it

may be worthwhile to determine the goodness of fits in different regions of the histograms, and compare them among the various distributions. Such a procedure could indicate which parts of the histogram are important, and might provide further insight on the physics of interaction of ultrasound with skin tissues.

5 Characterization of Skin Affected by Contact Dermatitis

5.1 Introduction

Ultrasonic tissue parameters such as the attenuation coefficient, backscatter coefficient, mean size of scatterers, scatterer number density, and echo statistics have been widely studied for their potential to classify normal vs. abnormal conditions in several tissues including the heart, liver, spleen, breast, eye, and kidney. These methods, commonly referred to as tissue characterization methods, are undertaken because of the fact that ultrasound B-scan images utilize only partial information in the backscattered echoes, and through appropriate signal processing, additional parameters that might provide information about tissue pathologies could be extracted. In the case of skin tissues such studies have not been widely investigated for characterizing skin lesions, despite the increasing reliance of high frequency ultrasound as a non-invasive imaging tool. Although ultrasound has the capability to image fine features in skin such as sweat gland ducts, hair follicles, and veins, the diagnostic capabilities of skin images to identify specific pathologies are limited. For instance, it is difficult to differentiate between benign and malignant lesions using B-scan images, as both types of lesions appear hypoechogenic with respect to normal skin [15]. Another study indicated that both scar tissue and malignant melanoma could appear similar in ultrasound scans [17]. Given the fact that skin is affected by a large number of lesions, it is worthwhile to study if tissue characterization methods have the potential to extract additional information for identifying and classifying various skin lesions.

Previous quantitative studies of skin lesions in vivo using ultrasound have mostly been limited to parameters that could be computed directly from images obtained using 20 MHz systems. Dermal echogenicity (mean backscatter amplitude) was found to be capable of differentiating between basal cell papilloma and melanoma [152]. Skin echogenicity and thickness were found to be related to changes due to photoaging [20]. Other parameters that require analysis of the radio frequency backscattered echoes such as the attenuation coefficient [88] and apparent integrated backscatter [153] have also been studied in normal skin tissues in vivo. In our earlier work we have studied frequency dependent attenuation and backscatter coefficients [92] as well as parameters related to echo statistics, such as the SNR (ratio of mean to standard deviation) and

parameters of envelope probability density functions (pdfs) of normal skin tissues in vivo [154]. The purpose of the present study is to determine if some of the above parameters could distinguish between normal skin and skin lesions. To test the methods, contact dermatitis (both allergic and irritant), is used as an example. Previous studies of skin affected by contact dermatitis using 15 and 20 MHz ultrasound have shown that changes in the dermis such as the increase in skin thickness, and decrease in echogenicity of the upper dermis can be visualized [19, 155, 156]. In this chapter, tissue characterization parameters namely the attenuation coefficient, and parameters related to the fluctuations of the envelope of backscattered signals are studied for their capability to differentiate skin affected by contact dermatitis from normal skin tissues. Skin thickness and echogenicity measurements are also reported. Before the tissue characterization parameters could be computed however, compensation for the system-dependent effects must be made. For instance when focused transducers are used, depth dependent diffraction effects due to variation in beam amplitude and beam size along the length of the beam could influence the results. Hence in this study we first obtain the diffraction correction curves empirically using human dermal tissue in vivo, and then use the correction curves to compute the various parameters with minimal diffraction effects. The computed parameters for normal skin and skin affected by contact dermatitis are then compared.

5.2 Materials and Methods

5.2.1 Experimental system

The fast-scan high-frequency imaging system (system III) described in Chapter 2 was used in this work. Briefly, the system consisted of a PVDF transducer (Panametrics, Waltham, MA; Model PI50), a pulser/receiver (Panametrics; Model PR5900), a 3-axis scanning system (Compumotor/Parker-Hannifin, Cleveland, OH), and a high-speed PCI-bus based A/D board (Gage Applied Sciences, Montreal, Canada). The pulser was set to operate at the energy and damping settings of 4 uJ and 50 ohms respectively. At these settings, the center frequency and –6 dB bandwidth of the reflection spectrum from a planar interface placed at the focus were measured to be 33 MHz and 28 MHz respectively. The f-number, focal length and diameter were specified by the manufacturer to be 2, 12.7 mm, 6.35 mm respectively. The theoretical axial and lateral resolutions of the system were computed to be about 25 and 90 μm respectively. The vertical range on the A/D ranged from –0.5 to 0.5 volts, which was sufficient to record backscatter echoes from the skin tissues, although the surface echo was sometimes saturated. The

transducer was set to scan continuously at a speed of 2 mm/sec and scan lines (RF data corresponding to A-scans) were acquired and stored at regular intervals corresponding to a spacing of 25 μm between the scan lines. Each echo sequence, digitized at 200 MHz, was an average of 50 repeated acquisitions, which significantly improved the echo signal-to-noise ratio. The distance moved by the transducer during the acquisition of the 50 waveforms that made up a single scan line was 5 μm (for a pulse repetition frequency setting of 20 kHz and a scan speed of 2 mm/sec; 50 μs/waveform x 50 waveforms x 2 mm/sec = 5 μm), which was small compared to the system's lateral resolution. Distilled water was used as the coupling medium between the transducer and tissue. For this purpose, a small water cup with a slot for allowing the ultrasound beam to pass through was used. At a scan speed of 2 mm/sec, a typical scan of 5 mm took 2.5 seconds. In practice, between 2 to 4 scans separated by 1 mm laterally were recorded. Also each lateral scan consisted of three scans focused at different axial locations. These three scans were such that for one of them the region of interest (ROI) was positioned at the transducer's focal zone, and for the other two the ROIs were positioned one above and one below the focal zone by 1 mm. In order to position the tissue of interest in the above manner, scan lines were visualized at the start of the experiment using the real-time oscilloscope capabilities of the software provided with the A/D board, and the location of the echo-entry line was adjusted by moving the transducer using a joystick. The three axial scans were done in order to reduce any residual post-correction diffraction effects by averaging the parameters computed for the three cases. Also, parameters computed from the different transverse scans were averaged to further reduce variability. Once the RF data were collected, B-scan images were created by computing the envelope using the Hilbert-transform approach. The field-of-view was 5.25 mm in the axial direction, and adjustable by the user in the lateral direction, typically 5 mm. Custom-written programs in Matlab (The MathWorks, Inc., Natick, MA) were used for generating and displaying the images.

5.2.2 Subjects and patch tests

Contact dermatitis is an inflammatory skin condition caused by skin contact with an exogenous agent. It can be broadly classified into two types, allergic contact dermatitis (ACD) and irritant contact dermatitis (ICD). One standard procedure to evaluate contact dermatitis is known as patch testing, wherein the allergen or irritant is mixed with petrolatum solution is applied to the skin for a specified amount of time. The affected areas are then subsequently evaluated, either immediately after patch removal, or after a specified amount of time. Seven subjects with a

clinical history of allergic contact dermatitis were recruited for the study by the collaborating investigators from the Massachusetts General Hospital (MGH). The subjects ranged in age from 25 to 66 (mean=41). Patch testing was performed on the subjects with contact allergens (fragrance mix, wool alcohol, nickel sulphate) incorporated in petrolatum using Finn chambers (Epitest Ltd. Oy, Norway) affixed with Scanpor tape (Norgesplaster, Vennesia, Norway). Allergens were applied for a period of 48 hours to the ventral side of the forearm for 2 subjects, and to the thigh for 5 subjects. Imaging was performed 24 hours after removal of the patches. Patch testing was also performed at the same body sites using 5% sodium lauryl sulphate in petrolatum to induce irritant contact dermatitis for the same seven patients. Similar to the allergic sites, patches were applied for 48 hours and ultrasonic imaging was done 24 hours after patch removal. Since the allergic and irritant reactions arise out of different mechanisms, they could be independent reactions for the same subject. Thus a total of 14 independent experiments were available to compare the lesion (both ACD and ICD) with normal skin. Clinical grading of the reactions as 0, 1, 2, and 3 was performed at the time of imaging by one of the clinical collaborators from MGH. A higher grade represented a more severe reaction. Nearby normal sites were also imaged. For control purposes, evaluation of a patch test site with petrolatum alone was done at an adjacent location for all subjects.

Additional patch tests were performed on the same set of patients: both allergic and irritant patches were applied for 12 hours and the sites were evaluated 12 hours after removal (referred to as 12-hour tests). The allergic patches were also applied for 24 hours and evaluated 48 hours after patch removal (referred to as 24-hour tests). Results from these additional tests were used along with the 48-hour tests mentioned in the preceding paragraph to determine trends in ultrasound parameters with clinical score. All the subjects who participated in the study signed informed consent documents approved by the Institutional Review Boards of both MIT and MGH.

5.2.3 Ultrasound parameters

Table 5.1 provides a summary of the quantitative parameters studied in this work.

Skin thickness: Skin thickness was measured using images displayed on the computer screen. The thickness was measured from the start of the entry echo to the interface between the dermis and subcutaneous fat. Since the interface between the dermis and fat was irregular, an average of

several thickness values based on several scans and several locations within a particular scan was used. Typically, a total of 16 measurements were used to compute the mean thickness.

Echogenicity of upper dermis: Echogenicity refers to the mean amplitude of echo envelope obtained from within an ROI. Echogenicity values were computed for the upper dermis, which was taken to be the region from 225 μm to 450 μm below the start of the surface echo. To accurately determine the depth in the above manner, the location of the surface echo was computed for each echo line by a threshold detection procedure.

Table 5.1: Summary of ultrasound parameters studied in this work.

Parameter	ROI
Skin thickness	Start of entry echo to the border between dermis and fat.
Echogenicity (mean backscatter amplitude)	Upper dermis, extending from 0.225 mm to 0.450 mm from the skin surface.
Attenuation coefficient slope	(a) Full dermis (b) Partial thickness corresponding to the thickness of the normal skin
Echo-statistics parameters: SNR, Weibull-*b*, K-α, GG-ν, and GG-*c*	Dermis extending from 0.5 mm to 1 mm from the surface.

Attenuation coefficient slope: Attenuation coefficient at any given frequency is the rate of decay of ultrasound with distance of propagation and is measured in units of dB/mm. Our previous studies have shown that within the range 14-50 MHz, the attenuation coefficient of skin tissues increases linearly with frequency [92]. The slope of the attenuation coefficient vs. frequency curve is referred to as the attenuation coefficient slope (β), which is represented in units of dB/mm/MHz. Computing this quantity involves the computation of mean power spectra as a function of depth for several frequencies. At first, an ROI parallel to the skin surface and corresponding to the dermis was selected by the user by a visual examination of the B-scan image. The dermis was identified as the hyperechoic tissue lying above the hypoechoic fat. The ROI selected by the user, which was initially an arbitrary quadrilateral, was modified into a parallelogram so as to have a uniform length in the axial direction at all the scan lines within the

ROI. Each scan line within the ROI was divided into several axial segments of 40 samples (200 ns) each with an overlap of 50%. The time duration of 200 ns corresponded to an axial slice thickness of 150 μm assuming a speed of sound of 1.5 mm/μs for the dermis. For a normal skin thickness of 1.2 mm in the volar forearm, 15 axial segments were available per scan line to compute attenuation in dB/mm. In the lateral direction a typical ROI of 4.0 mm consisted of 160 scan lines, each separated by 25 μm. Power spectra corresponding to all the segments and scan lines were obtained by computing the Fourier transform after applying a Hamming window, and squaring the magnitude of the resultant. The segment length of 200 ns provided a frequency resolution of 5 MHz. Once power spectra were obtained, diffraction correction determined by the location of the center of each of the segments were applied (see next section). Mean power spectra as a function of depth from the surface were then computed by laterally averaging the corresponding diffraction-corrected power spectra from all the scan lines. Spectral slopes (dB/mm) representing the decay of ultrasound with depth were then computed for several frequencies in the range 10-50 MHz. Finally, a linear fit to the spectral slope vs. frequency curve was computed to obtain the attenuation coefficient slope.

In the case of normal skin tissues, the entire dermis was used to compute the attenuation coefficient slope. In the case contact dermatitis, the thickness of the skin increased in many cases. In such cases, attenuation coefficient slopes were computed for both the full thickness as well as for the smaller thickness corresponding to that of the normal skin. In some of the affected sites, a sub-epidermal hypoechogenic band was seen. Including this band for the ROI did not however seem to affect the computed attenuation coefficient slopes significantly for cases analyzed in this work.

Echo-statistics parameters: The echo-statistics parameters studied in this work included the SNR of echo envelope, and the shape parameters of the Weibull, K, and Generalized Gamma (GG) distributions fitted to the envelope data histograms. The SNR is the ratio of mean to standard deviation of the envelope data and is related to the number density of scatterers within the resolution cell. It was computed using the estimated mean and standard deviations of the envelope data. The SNR is also a measure of deviation from the Rayleigh statistics, which occurs when the resolution cell consists of a large number of randomly distributed scatterers. The SNR is equal to 1.91 when the Rayleigh conditions are satisfied, less than 1.91 for pre-Rayleigh conditions, and larger than 1.91 for post-Rayleigh or Rician conditions.

The Weibull, K, and the GG distributions were studied because of their excellent fit to envelope data from normal skin tissues [154]. The shape parameters of the three distributions were determined by fitting probability density functions (pdfs) using the maximum likelihood (ML) method. The Weibull pdf is given by the following expression:

$$p(r) = \frac{b}{a}\left(\frac{r}{a}\right)^{b-1} e^{-\left(\frac{r}{a}\right)^{b}} \qquad r \geq 0;\ a,b > 0 \tag{5.1}$$

The parameter b is referred to as the shape parameter as it determines the shape of the pdf, whereas the parameter a is a scaling parameter. By suitably changing the values of the parameter b, the Weibull distribution can be made to model pre-Rayleigh $(b < 2)$, Rayleigh $(b = 2)$, and Rician $(b > 2)$ conditions. Hence the parameter b can also be seen to be a measure of deviation from the Rayleigh condition. To estimate this parameter, the log-likelihood function was first obtained:

$$L(r_1, r_2, ..., r_N, a, b) = N \ln b - (b-1)\sum \ln r_i - \sum\left(\frac{r_i}{a}\right)^{b} - Nb \ln a \tag{5.2}$$

where r_i represents an envelope sample, N represents the number of samples, and the summation is over all the samples. By setting the first partial derivative of the log-likelihood function with respect to a to zero, the following relationship between the parameters a and b is obtained:

$$a = \left(\frac{\sum r_i^{b}}{N}\right)^{1/b} \tag{5.3}$$

A simple one-dimensional exhaustive search method was then used to obtain the ML solution. A sufficiently large grid of solution points for the parameter b was chosen and the corresponding values for the parameter a were computed using Eq. (5.3). The log-likelihood function was computed at the points (a, b) using Eq. (5.2), and the one corresponding to the maximum was taken to be the solution. Further refinement around the solution point was then done to improve the accuracy of the estimates.

The K distribution has been previously studied in modeling ultrasound echo signals from the breast and liver [157]. Its pdf is given by:

$$p(r) = 2\left(\frac{r}{2}\right)^{\alpha} \frac{b^{\alpha+1}}{\Gamma(\alpha)} K_{\alpha-1}(br) \qquad r \geq 0;\ \alpha, b > 0 \tag{5.4}$$

The parameter α is the shape parameter, and can be identified as an effective scatterer number density [158]. The parameter b is a scaling parameter and $K_{\alpha-1}(x)$ is the modified Bessel function of the second kind of order α-1. The α parameter can take values ranging from zero to infinity. The K distribution approaches the Rayleigh distribution when α approaches infinity. To obtain the ML solution, the log-likelihood function was obtained:

$$L(r_1, r_2, ..., r_N, b, \alpha) = N\left[(\alpha+1)\ln(b) - \ln\left(\frac{\Gamma(\alpha)}{2}\right)\right] + \alpha\sum \ln\left(\frac{r_i}{2}\right) + \sum \ln\left(K_{\alpha-1}(br_i)\right) \tag{5.5}$$

Since the partial derivatives of the above expression are difficult to compute, a two-dimensional Nelder-Mead simplex optimization method in the Matlab's Optimization toolbox was used to obtain the ML solution as described in chapter 4.

The GG pdf is given by the following expression:

$$p(r) = \frac{c r^{(c\nu-1)}}{a^{c\nu}\Gamma(\nu)} e^{-\left(\frac{r}{a}\right)^{c}} \qquad r \geq 0 \qquad a, \nu, c > 0 \tag{5.6}$$

In the above expression, the parameter a is a scaling parameter and the parameters ν and c are the two shape parameters. In particular, the parameters ν and c are capable of adjusting more or less independently the lower and upper tails of the pdf respectively [89, 139]. The GG distribution has several other distributions as special cases: Rayleigh (c=2, ν=1), exponential (c=1 and ν=1), Nakagami (c=2), Weibull (ν=1) and also the usual gamma (c=1) distribution. Although no physical explanation seems available, this distribution has been found to be useful in modeling envelope signals from skin tissues better than many other distributions [154]. Besides it provides two shape parameters for characterizating tissues as opposed to one for the Weibull and K distributions. To compute the shape parameters, the log-likelihood function was first obtained:

$$L(r_1, r_2, ..., r_N, a, \nu, c) = N\ln c - (c\nu - 1)\sum \ln r_i - \sum\left(\frac{r_i}{a}\right)^{c} - Nc\nu \ln a - N\ln\Gamma(\nu) \tag{5.7}$$

By setting the first partial derivatives of the above expression with respect to c and a to zero we get [145]:

$$\nu = -\left\{ c\left(\frac{\sum \ln r_i}{N} - \frac{\sum r_i^c \ln r_i}{\sum r_i^c} \right) \right\}^{-1} \tag{5.8}$$

$$a = \left(\frac{\sum r_i^c}{N\nu} \right)^{1/c} \tag{5.9}$$

The ML solution was obtained using a 1D exhaustive search method similar to the one described for the Weibull pdf. At first a large solution grid was assumed for the parameter c, and the corresponding values for ν and a were obtained using Eqs. (5.8) and (5.9). The likelihood expression was then evaluated at the points (a, ν, c) using Eq. (5.7), and the one corresponding to the maximum was selected. Further refinement around the solution space was then done to improve accuracy.

It should also be pointed out that the parameters SNR, Weibull-b and K-α are not independent of one another, but the dynamic ranges for these three parameters are different. It can also be shown that over a small range of values, there is an approximately linear relationship between the Weibull-b parameter and the SNR.

For computing the above echo-statistics parameters, an ROI corresponding to the dermis from 0.5 to 1 mm below the skin surface was chosen. The reason for choosing only 0.5 mm for the ROI was to keep the length small enough to minimize both attenuation and diffraction effects within the ROI (although diffraction correction is applied based on the overall location of the ROI). The envelope samples corresponding to the scan lines within this ROI were collected to form empirical histograms. While combining the data only every other scan line and every fourth sample along a scan line were used due to the correlated nature of adjacent data samples. The spacing between the samples roughly corresponded to one-half of the system resolution in both the lateral and axial directions. Typically, a total of about 1600 samples were available for constructing envelope histograms. Once the parameters were estimated as described above, a correction for diffraction was applied to the parameters depending on the location of the center of the ROI (next section).

5.2.4 Statistics to compare normal and affected skin

The parameters computed for the skin affected by contact dermatitis (both allergic and irritant considered as one population and will be referred to as the affected sites) were compared against normal skin tissues using the Wilcoxon sign rank test. P-values to test if the difference in the values were significantly different from zero were computed (paired test). A value of $p < 0.05$ was considered significant.

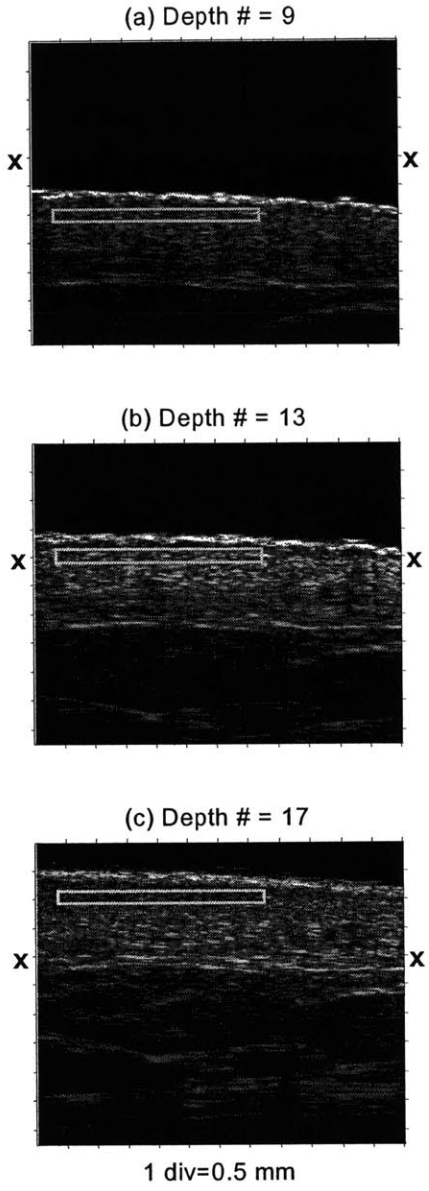

Figure 5.1: Experiments to determine diffraction correction curves. Ultrasound data were collected from skin in vivo when the tissue was at several depths separated by 0.25 mm. The figure shows three such depths, one each corresponding to the ROI being (a) below the focus, (b) at the focus and (c) above the focus. The 'x' marks indicate the location of the transducer's focal zone. The ROI drawn in the images indicate the ones used to compute mean power spectra at various distances from the transducer. Another set of ROIs, larger than the above were used to compute echo-statistics parameters.

5.3 Diffraction correction

The use of focused transducers requires compensation for diffraction effects while computing quantitative tissue characterization parameters. Due to variation in the beam amplitude with distance, diffraction affects power spectra measurements and consequently the attenuation coefficient slope. Diffraction also affects the echo statistics due to variation in the beam size with distance. Various approaches, both theoretical and experimental have been proposed for compensating measured power spectra for diffraction effects. In our previous studies [92, 154], the transducer was axially translated so as to shift the location of the focal zone to a particular depth of interest. In such experiments, a correction was not required as data were always obtained from the transducer's focal zone. Such a technique was found to be less preferable in a clinical research setting due to the increased time of imaging. Hence it was decided to correct for the diffraction effects using empirically obtained correction curves. Previous studies have shown that the diffraction correction curves are themselves dependent on the medium being imaged [159]. Hence instead of using tissue-mimicking material, human dermis in vivo was used to obtain the diffraction correction curves. The basic premise in our methods is that if the same tissue is placed at different distances from the transducer, then any parameter being computed (e.g power spectrum at a particular frequency, SNR, Weibull-*b* etc.) must be the same at all the locations once diffraction compensation is applied. Data were collected at the dorsal forearm of five subjects for 19 locations spaced apart by 0.25 mm through axial translation of the transducer. Two repetitions were done for all the subjects, who were different from the ones that participated in patch testing. Figure 5.1 illustrates the images obtained when the tissue was at three of the 19 distances from the transducer. For each of the 19 images, two sets of ROI, one for studying variations in mean spectra with depth, and the other for studying the variation in echo-statistics parameters with depth, were selected. The former ROI spanned a distance of 0.225 mm (60 samples) in the axial direction while the latter spanned a distance of about 0.5 mm in the axial direction. The mean spectra, echogenicity, SNR, Weibull-*b*, K-α, GG-ν and GG-*c* parameters were computed for all the 19 locations as described in the previous section.

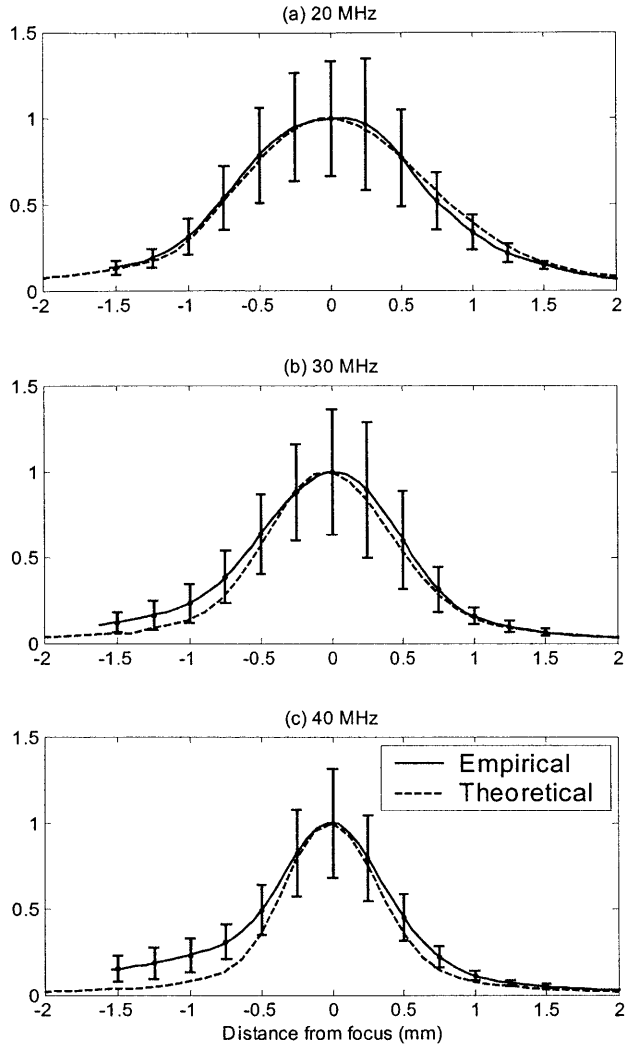

Figure 5.2: Diffraction correction curves for correcting power spectra as a function of the distance from the focus. The correction curves were obtained using human dermal tissues in vivo. The solid line is the mean correction curve from 10 experiments (5 subjects, 2 repetitions each) and the error bars indicate the standard deviations. The dashed curve is based on the theoretical formulation developed by Chen et al [100].

Figure 5.2 shows the diffraction correction curves for the power spectra at three frequencies over a distance of 1.5 mm on both sides of the focus. It can be seen that the correction curve has a narrower width at higher frequencies, which is consistent with the fact that higher frequencies are more tightly focused. For comparison, theoretical diffraction correction curves developed by Chen et al [100] are also shown. The theoretical and empirical correction curves agree very well at lower frequencies. At higher frequencies the empirical curve is seen to be broader than the

theoretical curve. This could be due to the fact that a finite length was used for both the segment length in computing the power spectrum (0.225 mm) and for the stepping distance between the different locations (0.25 mm). These two effects tend to smear the correction curves, the effects of which are more prominent for the higher frequencies. During data reduction, the empirically computed diffraction corrections were used to correct power spectra measurements by dividing by the correction factor at the appropriate distance. The attenuation coefficient slope was then computed using the corrected power spectra.

Figure 5.3 shows the computed diffraction correction curves for the echo-statistics parameters. The SNR generally increases with distance from the focus. This is expected as away from the focus, the beam becomes broader and therefore larger number of scatterers contributes to the resultant. The increase in the number of scatterers pushes the envelope pdf closer to Rayleigh pdf and the SNR approaches 1.91. The location of the minimum point of SNR however does not match the location of the focus, but is seen to be deeper. The reason for this is not clear, but is probably due to the fact that the dermal tissue scatterers are not uniformly dense within the 0.5 mm ROI, and that variations in amplitude of the beam within this 0.5 mm affect the echo statistics in a complex way. Similar trend is seen for the Weibull-*b* and K-α parameters. The Weibull-*b* curve is very similar to the SNR curve, which is due to the fact that the two quantities are approximately linearly related over the limited range of values obtained. The K-α parameter becomes large as we move away from the focus, which is a consequence of the envelope pdf approaching the Rayleigh pdf. The percentage variability in the estimates is larger for this parameter than that for the other parameters, which is due to the fact that a very large sample size is needed for estimation even for moderately large values of α. The GG-ν curve shows a trend that is opposite to that of the SNR, Weibull-*b* and K-α parameters while the GG-*c* parameter shows a trend that is similar to the above parameters. The mean correction curves for all the parameters were normalized so as to have minimum value of unity for all the parameters except the GG-ν, which was normalized to have a maximum value of unity. The normalized diffraction correction curves were then used to correct estimated quantities by dividing by the correction factor at the appropriate distance.

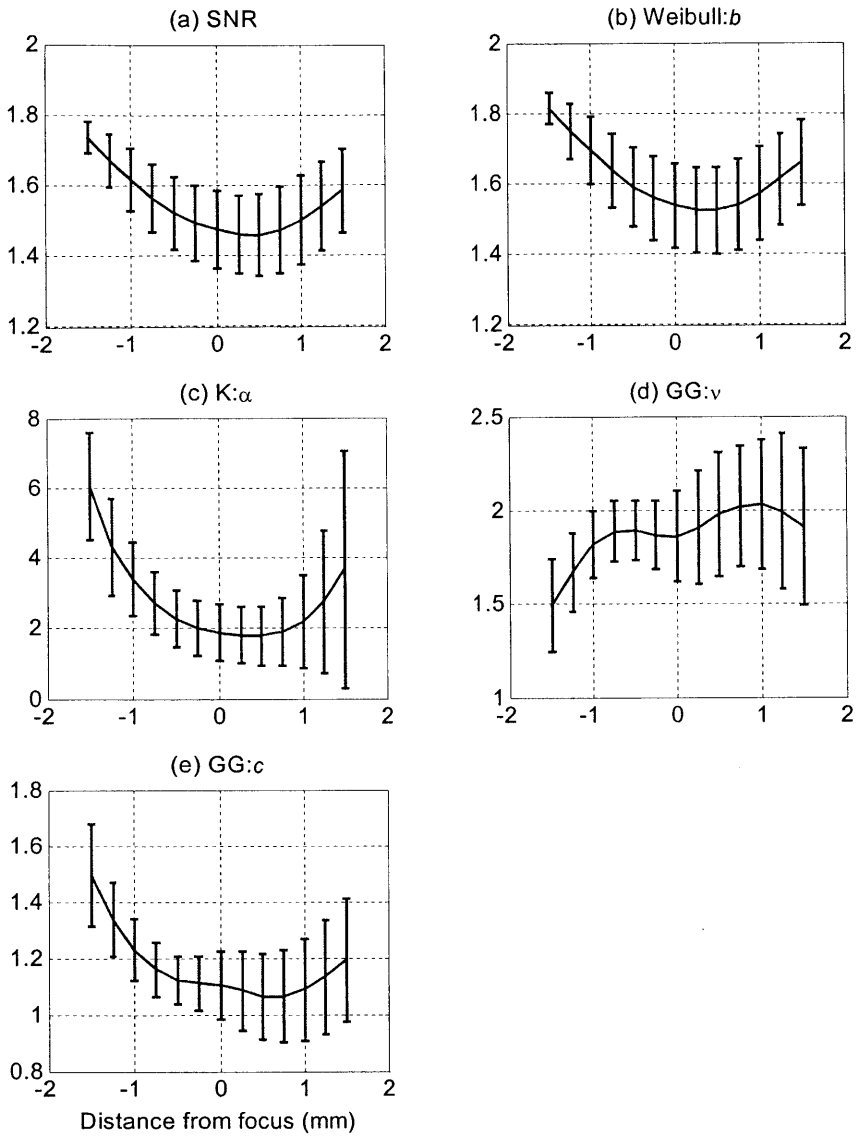

Figure 5.3: Diffraction correction curves for correcting estimates of echo-statistics parameters as a function of the distance from the focus. The correction curves were obtained using human dermal tissues in vivo. The solid line is the mean correction curve from 10 experiments (5 subjects, 2 repetitions each) and the error bars indicate the standard deviations. The increase in SNR away from the focus indicates that the envelope pdf approaches the Rayleigh pdf.

In order to verify the diffraction correction procedure, data were collected from one additional subject (this subject was different from the ones used in obtaining the correction curves). All the ultrasonic parameters were computed and corrected for diffraction effects. Figure 5.4 shows the power spectra at 20, 30, and 40 MHz as a function of distance from the focus. Comparing Figures 5.2 and 5.4, it can be seen that the correction has resulted in a more uniform distribution of the

power spectra. The power spectra show variability, which could be attributed to the use of a finite number of scan lines in computing the mean power spectra. The variability in the corresponding attenuation coefficient slope would be smaller because the linear fit of the dB/mm vs. frequency curve would tend to smoothen the variations. The variability was further minimized through averaging the computed attenuation coefficient slopes obtained from several scans, both axial and lateral. Figure 5.5 shows the corrected echo-statistics parameters as a function of the distance from the focus. Comparing Figures 5.3 and 5.5, it can be seen that the diffraction correction to these parameters has resulted in a more uniform distribution of the parameters with distance. The variability is seen to be the highest for the K-α parameter. The variability is also reduced by averaging estimates from several axial and lateral scans.

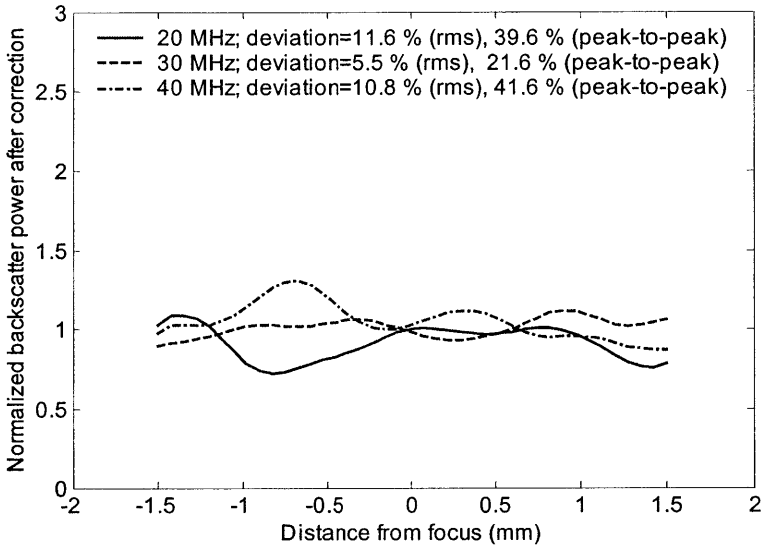

Figure 5.4: Corrected power spectra as a function of the distance from the focus.

It should also be emphasized that the diffraction corrections for the SNR and pdf shape parameters are only valid within a limited range of values. To apply the correction curves to the echo-statistics parameters, the scattering conditions need to be pre-Rayleigh after correction. For example, if the diffraction correction in Fig. 5.3 (b) is used for a tissue that already shows Rayleigh statistics at the focus (SNR=1.91), the compensated values when the ROI is away from the focus would be larger than 1.91, which is incorrect, as the increased beam size should still

result in Rayleigh conditions. In this work, all the computed values for both the normal tissues and skin lesions were pre-Rayleigh even after the application of correction functions.

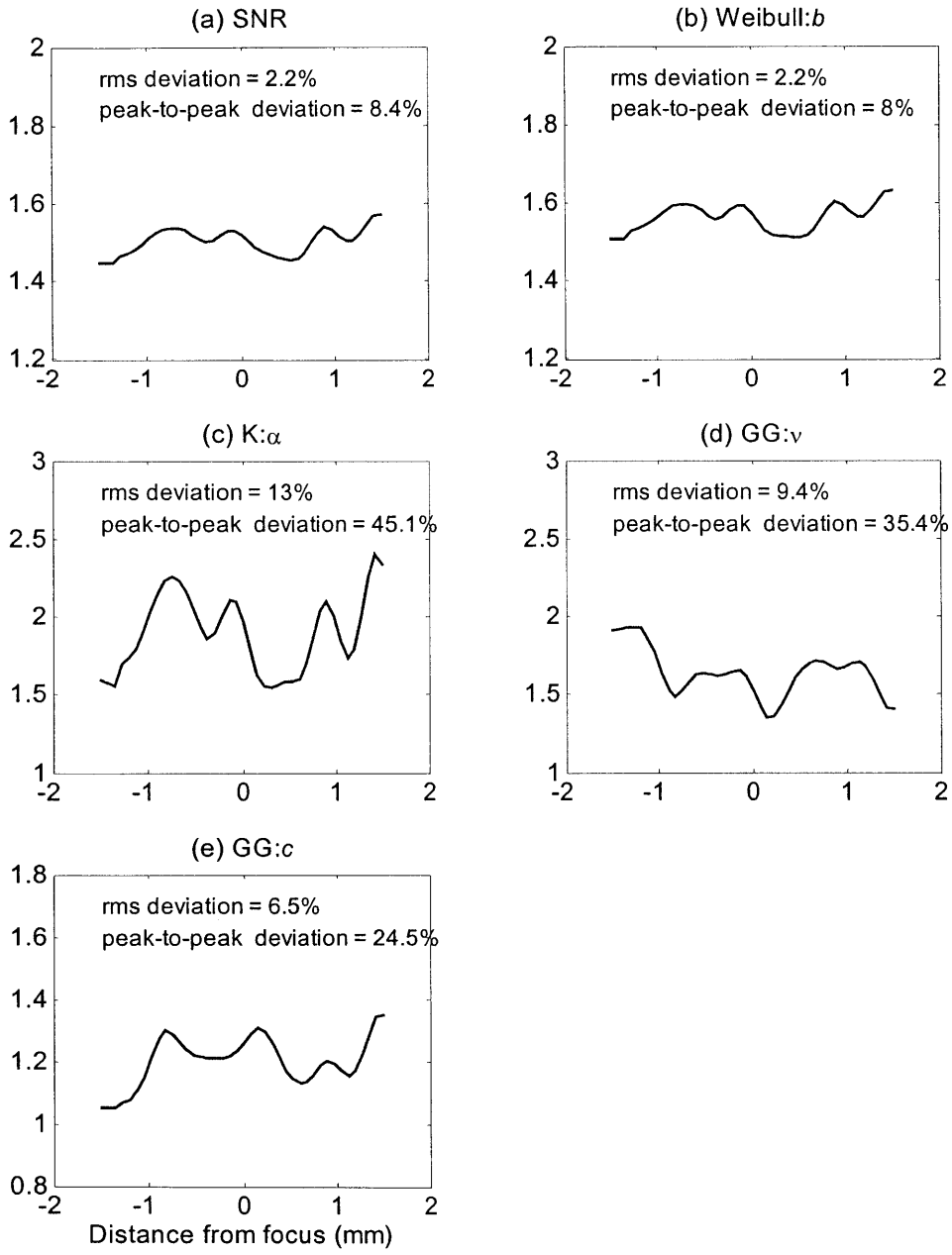

Figure 5.5: Corrected echo-statistics parameters as a function of the distance from the focus.

5.4 Results

Figure 5.6 shows an image of a normal skin tissue and skin affected by allergic contact dermatitis for one subject. It can be seen that the skin thickness increased significantly for the case of contact dermatitis. It can also be seen that in the case of the affected skin, the amplitude of the pixels in the upper dermis decreases. Figure 5.7 shows the differences in skin thickness measurements at the affected sites and the corresponding normal skin. Only data from the 48-hour patch tests (Section 5.2.2) were used in these results. Also, data from all subjects irrespective of whether changes were clinically observed or not, were used. Significant increases in the skin thickness can be seen at the affected sites. The petrolatum control site also showed a slight but insignificant increase in skin thickness. Figure 5.8 shows the skin thickness increase from the normal values as a function of clinical score. In these results, data from all the three patch tests were used. A progressive increase in the mean skin thickness with increasing clinical score was observed. No significant difference is seen between the zero score cases and the petrolatum control cases.

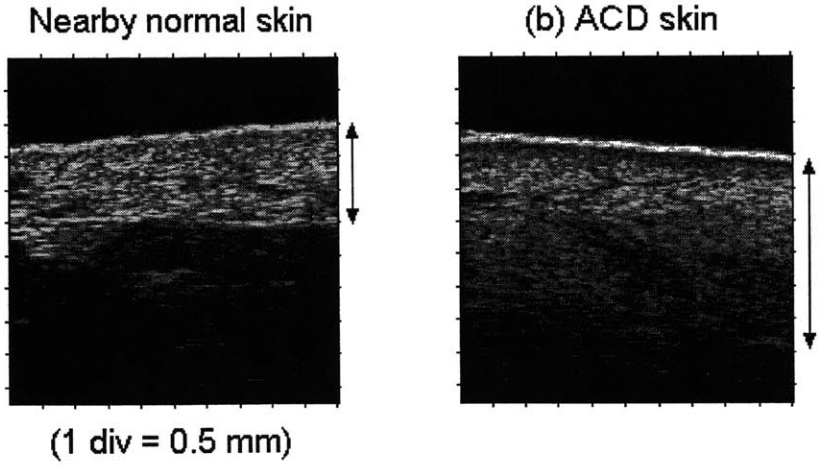

Figure 5.6: Images of (a) normal skin and (b) skin affected by allergic contact dermatitis (ACD). The extent of the dermis is shown by the arrows. The increased thickness in the case of contact dermatitis can be seen.

Figure 5.9 shows the differences in the echogenicity of the upper dermis between the affected sites and the normal skin for the 48-hour patch tests. A significant decrease in the echogenicity value could be seen. Figure 5.10 shows the differences in echogenicity as a function of the clinical score for data from all the patch tests. The decrease in the mean values from the normal skin value is found to be more for more severe reactions.

Figure 5.11 shows the differences in attenuation coefficient slope between the affected sites and the normal skin. As in Figs. 5.7 and 5.9, only data from the 48-hour patch tests were used. Since the skin thickness in general increased for the affected sites, the values were computed for both the full thickness of the skin and for the partial thickness corresponding to that of the normal skin. In both cases the affected skin showed a significant decrease in the attenuation coefficient slope. The change for the partial thickness case was slightly smaller than that for the full skin thickness case. Figure 5.12 shows the differences in attenuation coefficient slope as a function of the clinical score. As in Figs. 5.8 and 5.10, data from all three patch tests were used. The cases corresponding to scores 1, 2 and 3 showed significant differences from the normal skin. When the full thickness was used, a noticeable decrease in the mean value from score 2 to 3 was seen. Such a trend is however not seen when only the partial skin thickness was used to compute the attenuation coefficient slope.

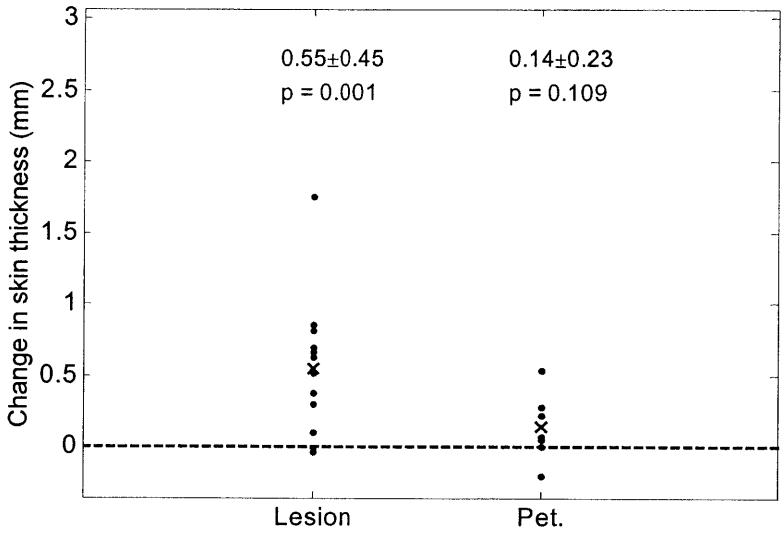

Figure 5.7: Difference in skin thickness between the affected sites and the normal skin, and between the petrolatum control site and the normal skin. In the case of the lesion, 14 data points (7 subjects, 2independent cases per subject – one for ACD and the other for ICD) were available and are shown by the dots. In the case of the control site, 7 data points were available. The 'x' marks indicates the mean of the respective data sets. The text in the figure refers to mean±SD (first row) and the p-values (second row).

Figure 5.13 shows the differences in echo-statistics parameters between the affected sites and the normal skin for the 48-hour patch tests. Although slight increases in the mean values could be seen for all the parameters except for the GG-ν parameter where a decrease was seen, the differences were not statistically significant. Among the various parameters, the GG-ν and GG-*c* parameters were seen to perform relatively better in that their p-values were smaller than that of the others.

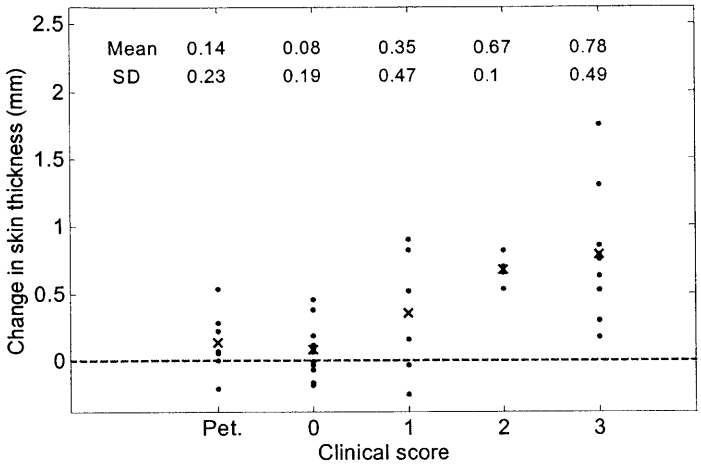

Figure 5.8: Difference in skin thickness between the affected sites and normal skin as a function of the clinical score. Also shown is the difference for the petrolatum control case. Each dot represents a data point and the 'x' mark indicates the mean.

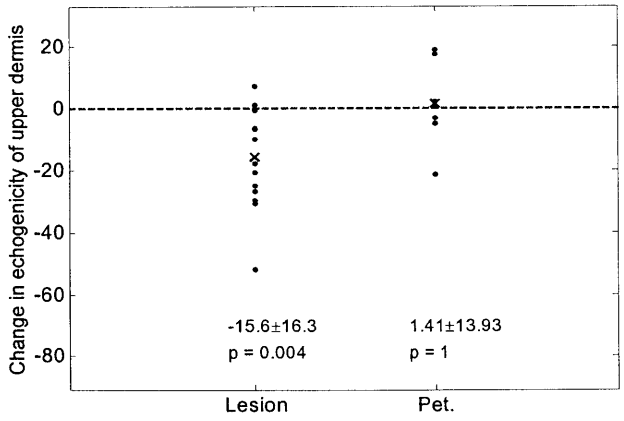

Figure 5.9: Difference in echogenicity values between the affected sites and the normal skin, and between the petrolatum control site and the normal skin. Each dot represents a data point and the 'x' mark indicates the mean. The text in the figure refers to mean±SD (first row) and the p-values (second row).

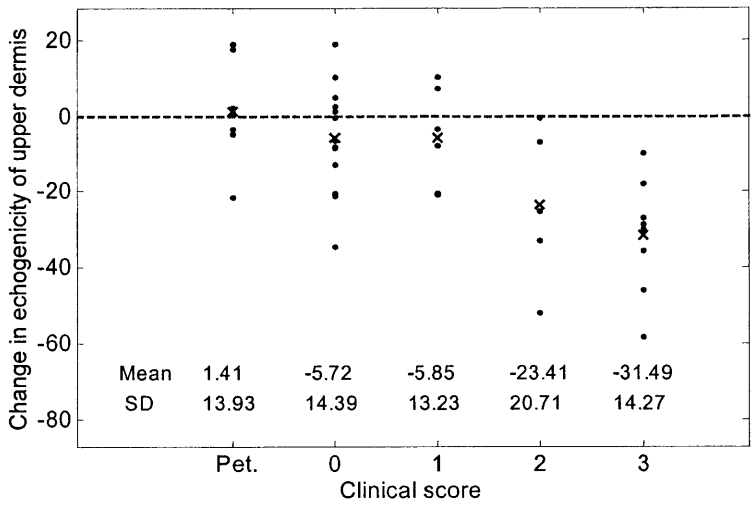

Figure 5.10: Difference in echogenicity of the upper dermis between the affected sites and normal skin as a function of the clinical score. Also shown is the difference for the petrolatum control case. Each dot represents a data point and the 'x' mark indicates the mean.

5.5 Discussion

In this work, the application of ultrasonic tissue characterization methods for evaluating skin lesions was studied. Contact dermatitis was chosen as an example because of the ease of patch testing methods. Table 5.2 summarizes the quantitative results from this work for all the parameters studied.

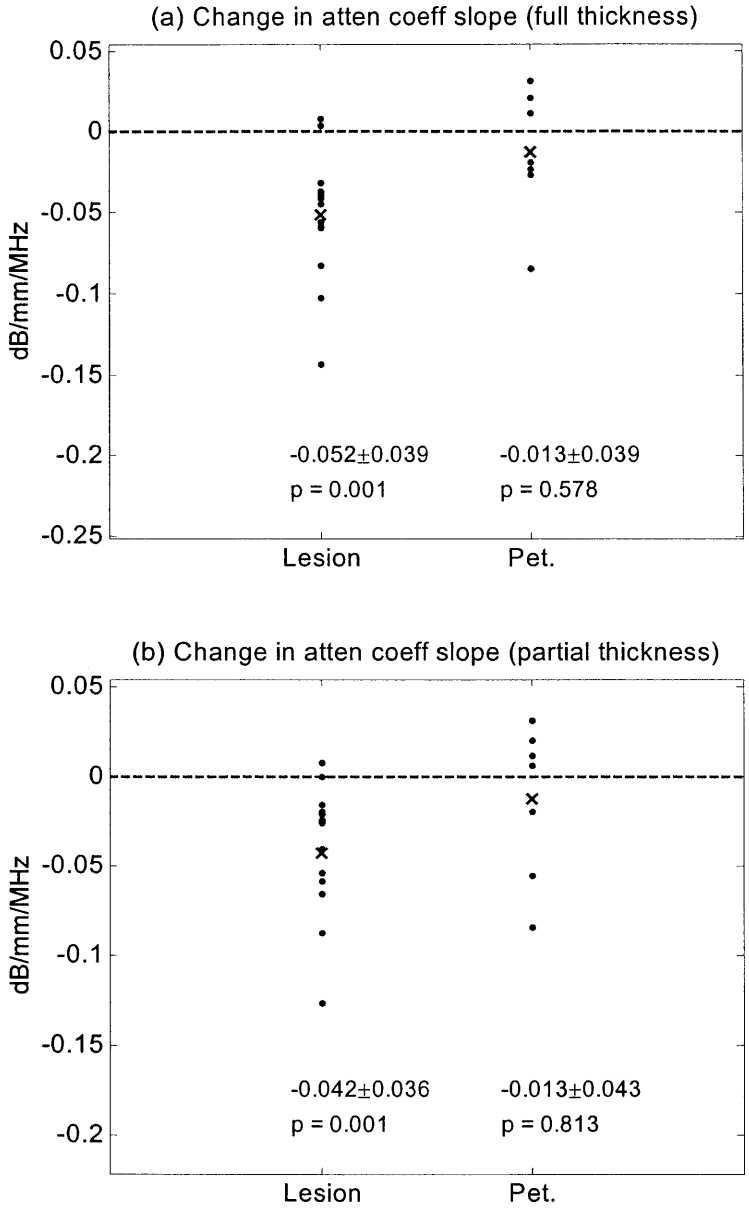

Figure 5.11: Difference in attenuation coefficient slope between the affected sites and the normal skin. Also shown is the corresponding difference at the petrolatum control site. Each dot represents a data point and the 'x' mark indicates the mean. The text in the figure refers to mean±SD (first row) and the p-values (second row). The top panel is for the case when the entire skin thickness was used in computing the attenuation coefficient slope. The bottom figure is for the case when only the skin thickness corresponding to that of the normal skin was used in computing the attenuation coefficient slope.

Our results confirm earlier work with 15 MHz ultrasound that showed that the thickness increases in skin affected by contact dermatitis, and that the increase is larger for more severe reactions [160]. Our results also confirm earlier results using 20 MHz ultrasound [19] that alterations occurring at the papillary dermis decrease the echogenicity in this region. Our study seems to be the first where attenuation coefficient slope has been calculated for skin affected by contact dermatitis. The results indicated that the attenuation coefficient slope decreases when skin is affected by contact dermatitis. The attenuation coefficient slope at the affected sites was 80%±17% (mean±SD) of that of the normal skin. When the sites that did not show any reactions clinically were excluded (cases corresponding to zero scores), the attenuation coefficient slope was 71%±13% of that of the normal skin. One reason for the decrease in the affected skin areas could be that the dermis expands due to edema and is filled by fluids that increase the water content. A previous study has shown that attenuation is inversely related to water content [82]. The increase in water content in the affected areas would then decrease the attenuation coefficient. Another reason could be that due to the increased thickness of the skin, the same amount of attenuation occurs over a larger distance, which in turn decreases the attenuation coefficient. This might also explain why the decrease in attenuation coefficient slope is larger for more severe reactions, for which the increases in skin thickness were larger.

On B-scan images, the exact increase in skin thickness for the lesions was sometimes hard to visualize as the border between the dermis and fat was less pronounced compared to the normal skin tissues. In such cases the contrast in the images had to be adjusted on the screen, and more than one scan had to be looked at to determine the border between the dermis and fat. For this reason, the attenuation coefficient slope might be an additional useful parameter to include in characterizing contact dermatitis.

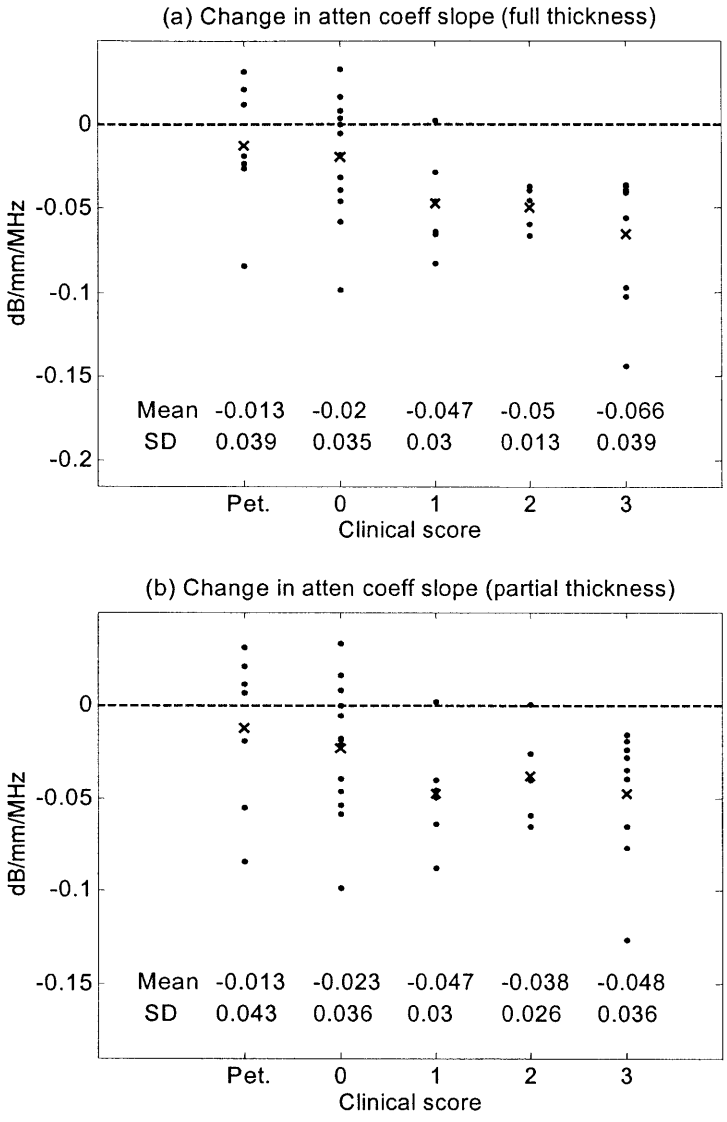

Figure 5.12: Difference in attenuation coefficient slope between the affected sites and normal skin as a function of the clinical score. Also shown is the corresponding difference at the petrolatum control site. Each dot represents a data point and the 'x' mark indicates the mean.

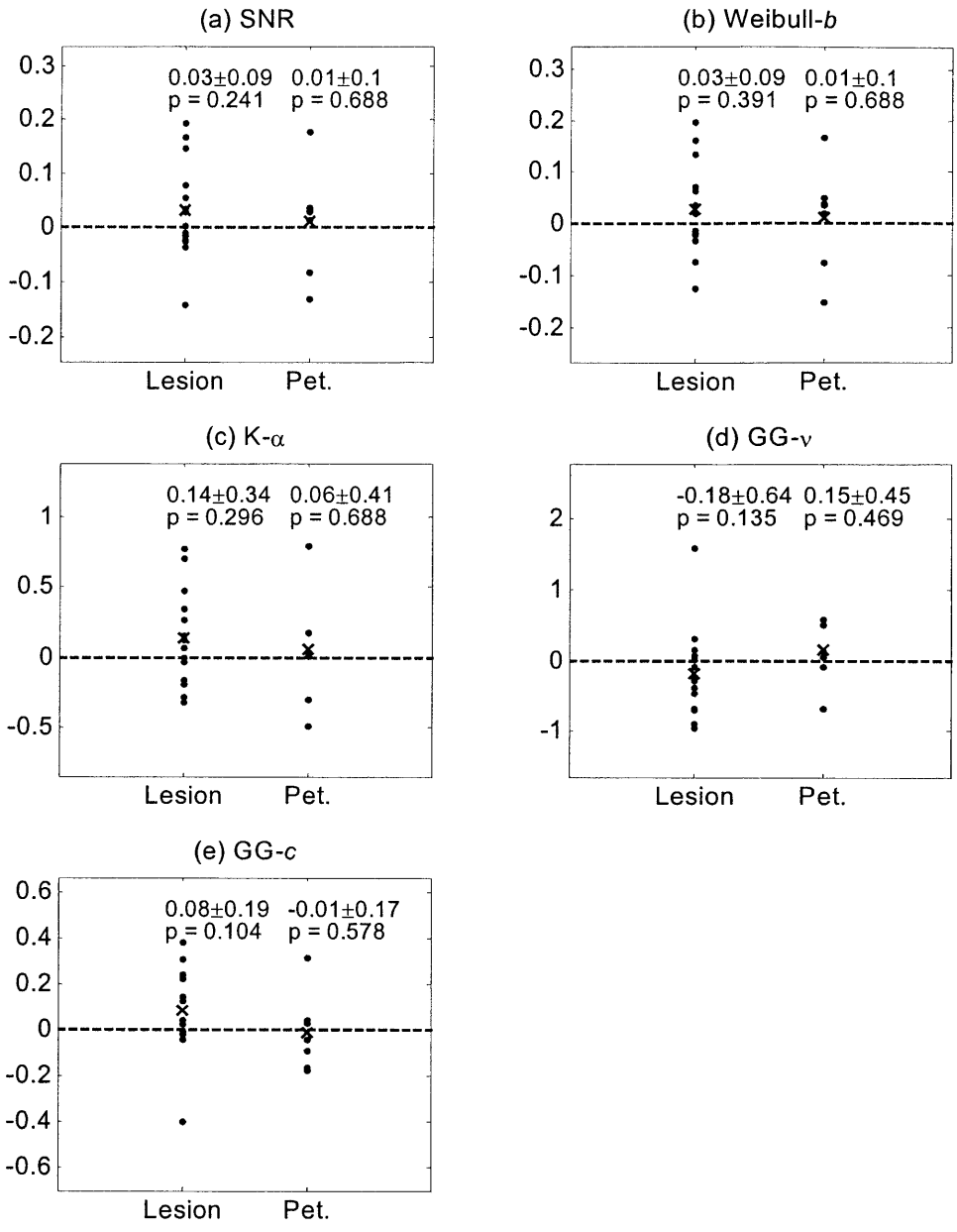

Figure 5.13: Difference in echo-statistics parameters between the affected sites and the normal skin. Also shown is the corresponding difference at the petrolatum control site. Each dot represents a data point and the 'x' mark indicates the mean. The text in the figure refers to mean±SD (first row) and the p-values (second row).

Our previous study on echo statistics showed that the Weibull, K and GG pdfs were good at modeling the statistical fluctuations of envelope of backscatter signals from skin tissues [154]. In

this study the parameters of these pdfs were computed at an ROI that spanned from 0.5 to 1 mm from the skin surface. The aim was to determine if there were changes to mid-dermis that could be registered by these parameters. However the results showed no significant differences between the affected sites and the normal skin. This is surprising since due to edema, the density of scatterers could be expected to decrease, and consequently the SNR could be expected to decrease. Our results indicate that the edema formation might be localized to the upper dermis. Further studies would be required to investigate changes in these parameters. In general, the study of echo-statistics parameters was difficult because a large homogeneous ROI could not always be chosen due to the presence of inhomogeneities such as hair follicles or sweat gland ducts.

Table 5.2: Summary of results. The values indicated are mean (SD). In the case of attenuation coefficient slope β, two values were computed, one corresponding to the full thickness of the lesion and the other corresponding to the thickness of the normal skin. Data from all three patch tests, for both ACD and ICD were used.

	Normal	Lesion (all scores)	Lesion (excluding zero scores)
Thickness (mm)	1.459 (0.212)	1.865 (0.462)	2.059 (0.478)
Upper dermis echogenicity	56.8 (17.7)	41.2 (15.6)	32.7 (11.0)
Full thickness β (dB/mm/MHz)	0.199 (0.040)	0.157 (0.042)	0.139 (0.035)
Partial thickness β (dB/mm/MHz)	0.199 (0.040)	0.163 (0.034)	0.150 (0.028)
SNR	1.375 (0.067)	1.377 (0.070)	1.387 (0.070)
Weibull-*b*	1.439 (0.072)	1.440 (0.072)	1.447 (0.074)
K-α	1.329 (0.322)	1.330 (0.277)	1.380 (0.291)
GG-ν	2.344 (0.391)	2.442 (0.755)	2.236 (0.595)
GG-*c*	0.945 (0.087)	0.953 (0.166)	0.995 (0.156)

In this study, both the allergic and irritant reactions were considered together as one population. It is possible that any genuine differences in the computed parameters between the allergic and irritant sites contribute to the variability seen in the results. Future work could study if significant differences between the allergic and irritant reactions are observed for the ultrasonic tissue characterization parameters. In future studies, other non-invasive methods such as trans-

epidermal water loss measurements and confocal imaging parameters [161] could be combined with ultrasonic tissue parameters to characterize skin affected by contact dermatitis

6 Summary and Future Work

6.1 Contributions of this thesis

The overall contribution of this thesis is the introduction of quantitative ultrasonic methods in characterizing skin tissues in vivo. Very few studies on characterizing skin with ultrasound exist at present. Almost all of these studies dealt with excised skin tissues. This is a serious limitation as the ultimate aim of tissue characterization methods is to evaluate tissues in a clinical and preferably, an out-patient setting, The specific contributions of this thesis are as follows:

The attenuation coefficient of normal skin tissues was shown to be a linearly increasing function of frequency over a range of frequencies relevant to dermatological applications (14-50 MHz). The fact that a linear dependence was sufficient indicates that the attenuation coefficient slope could be a useful parameter for characterization. However whether such a linear dependence is a good model for specific skin lesions needs to be tested.

The study also found that the attenuation coefficient slopes of the dermis and fat tissues were similar. This was a surprising result given that these tissues differ in so many other ways. The study also found that ultrasonic properties of the dermis such as the attenuation coefficient slope could vary from one body-site to another. This is important in that it indicates that in future studies the normal skin data should be obtained as close as possible to the site of the lesion.

The backscatter coefficient of normal skin tissues were measured in vivo for the first time. The computation of backscatter coefficients is considerably more complicated than the attenuation coefficients in that the system-dependent effects should be removed through appropriate data reduction methods. To ensure that the results were independent of the measuring system, three different transducers were used and the results were found to agree with one another. Moreover two different methods to extract the backscatter coefficient also gave similar results. The backscatter coefficient of the dermis was found to have an increasing dependence with frequency, but did not show a single power-law type dependence over the range 14-50 MHz.

This thesis also seems to be the first time the statistical fluctuations of ultrasonic backscatter signals from skin tissues have been studied. The results indicated that non-Rayleigh statistics are present in the case of envelope backscatter fluctuation from skin tissues for the systems that are

commonly used in skin imaging. The presence of non-Rayleigh statistics leads to additional possibilities for characterizing skin tissues through the use of the pdf shape parameters.

In this work, the generalized gamma distribution was used for the first time in modeling backscatter data from *any* tissue. Although a recent independent work [89] also proposed the use of this distribution in modeling ultrasound echo fluctuations, this thesis seems to be the first where actual data from tissues have been modeled. The generalized gamma distribution was found to be able to fit the echo data from skin tissues very well. However the estimated parameters showed a larger variability than the parameters of the other distributions. Despite this variability the shape parameters of the generalized gamma distribution were able to differentiate dermal tissues at different locations better than that of the other distributions.

This is also the first time, to the best of the author's knowledge, that tissue characterization parameters that require data reduction have been applied for any skin lesion, and not just contact dermatitis. Previous works have at best have used image-based parameters such as echogenicity to characterize skin lesions. While such image-based quantities are certainly useful, they have the same limitations that a conventional image has, namely they utilize only partial information in the backscatter echoes. The results of this study showed that skin affected by contact dermatitis has a smaller attenuation coefficient slope than that of the normal skin. However no changes in the echo statistics were found. These results indicate that in the future, a combination of several parameters might be useful in characterizing tissues.

6.2 Suggestions for future work

The work presented here represents only an initial attempt at characterizing skin tissues with high-frequency ultrasound. Suggestions for future work are as follows. Ultrasound data could be collected from various skin lesions, and a database of ultrasonic properties could be created. The specificity and sensitivity of the parameters to identify and differentiate skin lesions could then be tested using independent subjects. Of particular importance would be skin cancer, both melanoma and non-melanoma cancer, as well as other pigmented skin lesions. In addition to characterizing various skin lesions, ultrasound would also be suited for determining the tumor margins, if in fact a biopsy is needed.

At present the device is limited to imaging body-sites that are topologically accessible to ultrasound. These include reasonably flat regions such as the forearm, thigh, or parts of the body that could be easily constrained such as the fingertip. Further ergonomic modifications to make the device more easily accessible to other parts of the body would be very useful.

The data collected in this work could be analyzed to extract additional parameters such as the mean scatterer size in skin. The scatterer size could be determined from the frequency dependence of the backscatter coefficient. Such studies using conventional ultrasound have been previously shown to have potential in characterizing renal tissues [162].

The epidermis was not studied in this work because the resolution of the device was not sufficient to resolve layers in the epidermis. The use of much higher frequency systems could provide the capability to characterize epidermal layers.

In future studies, ultrasound parameters could be combined with parameters extracted with other non-invasive imaging methods, especially confocal microscopy and optical coherence tomography, in order to characterize skin lesions. This might prove to be more useful than using a single modality because ultrasonic and optical methods provide different information about the tissue microstructure and could compliment each other.

Other ultrasonic techniques such as elastography (strain imaging) could also be studied for their potential in characterizing skin lesions. Such methods would require modifications to the present device. In particular, a method to deliver a known indentation to the skin surface would be needed. Additionally, if mechanical properties such as the Young's Modulus or Poisson's ratio are needed, the force of indentation must be known as well. The mechanical properties can then be used to characterize skin lesions.

Compared to other tissues, scattering from structures in skin tissues is poorly understood. In normal skin, scattering occurs from densely packed collagen fibers. Commonly made assumptions such as the absence of shear waves and the absence of multiple scattering effects may not be applicable in this case. More fundamental studies using simpler tissue-mimicking phantoms or computer simulations may provide insight into the scattering mechanisms in skin tissues.

The generalized gamma and Weibull distributions could also be studied for characterizing tissues other than the skin.

Appendix A: Derivation of the Diffraction Correction Term for the Computation of Backscatter Coefficients

This Appendix presents the derivation of Eq. (3.9). In the following, the symbols f, λ and k represent the frequency, wavelength and the wave number of the wave respectively. Although these three quantities are related, it is convenient to use all of them explicitly in the derivation. The aim is not to be rigorous, but to provide simple derivations based on well known concepts in linear acoustics. See also Madsen [101].

Let us assume that the field generated at the face of the transducer is represented by $A(f)$. This field is assumed to be constant over the face of the transducer. The propagated field due to this aperture in the vicinity of a scatterer located at the point r is given by [105]

$$P_{inc}(f) = \frac{A(f)}{j\lambda} \iint_{S'} \frac{e^{jk|r-r'|}}{r-r'} ds' \tag{A.1}$$

where S' represents the transducer aperture and r' represents a point on it. The suffix *inc* indicates that this field is the incident field to the scatterer, which is subsequently backscattered towards the transducer. The backscattered field at a generic point on the transducer's face (once again denoted by r') is given by:

$$\begin{aligned} P(r,r') &= P_{inc} \frac{e^{jk|r-r'|}}{|r-r'|} \Phi(f) \\ &= \left(\frac{A(f)}{j\lambda} \iint_{S'} \frac{e^{jk|r-r'|}}{r-r'} ds' \right) \frac{e^{jk|r-r'|}}{|r-r'|} \Phi(f) \end{aligned} \tag{A.2}$$

where $|\Phi(f)|^2$ is the differential scattering cross-section of the scatterer at an angle of 180 degrees. Here we have assumed that the scatterer is far enough from the transducer such that the angular dependence of $\Phi(f)$ can be ignored. Now integrating the backscattered field over the face of the transducer, and applying the electromechanical response of the transducer $T(f)$, the following expression is obtained for the voltage signal due to this single scatterer:

$$
\begin{aligned}
V(f,r) &= T(f)\iint_{S'} p(r,r')ds' \\
&= T(f)\iint_{S'}\left(\frac{A(f)}{j\lambda}\iint_{S'}\frac{e^{jk|r-r'|}}{r-r'}ds'\right)\frac{e^{jk|r-r'|}}{|r-r'|}\Phi(f)ds' \\
&= T(f)\frac{A(f)}{j\lambda}\left(\iint_{S'}\frac{e^{jk|r-r'|}}{r-r'}ds'\right)^2\Phi(f)
\end{aligned}
\tag{A.3}
$$

Now assuming incoherent scattering by the tissue, the total power recorded is obtained by summing or integrating the contributions from all scatterers (incoherent assumption leads to summing powers rather than summing instantaneous amplitudes):

$$
\begin{aligned}
\left|V^2_{tissue}(f)\right|^2 &= \iiint_{\Omega}\left|V(f,r)\right|^2 N d\Omega \\
&= \iiint_{\Omega}\frac{\left|A(f)\right|^2\left|T(f)\right|^2}{\left|j\lambda\right|^2}\left|\iint_{S'}\frac{e^{jk|r-r'|}}{r-r'}ds'\right|^4\left|\Phi(f)\right|^2 N d\Omega \\
&= \frac{\left|A(f)\right|^2\left|T(f)\right|^2}{\left|j\lambda\right|^2}\left|\Phi(f)\right|^2 N\iiint_{\Omega}\left|\iint_{S'}\frac{e^{jk|r-r'|}}{r-r'}ds'\right|^4 d\Omega
\end{aligned}
\tag{A.4}
$$

where Ω represents the scattering volume and N is the number of scatterers per unit volume in the tissue.

To get rid of the transducer's electromechanical response, the reflection from a planar reflector located at the focus is recorded. This is the same as the signal recorded by an identical transducer located at a distance of twice the focus (referred to as the mirror transducer), except for the reflection coefficient between the planar reflector and the surrounding fluid, usually water. To compute this quantity, first consider the field at a distance twice the focal length:

$$
\text{Field at twice the focal length}=\frac{A(f)}{j\lambda}\iint_{S'}\frac{e^{jk|r-r'|}}{r-r'}ds' \tag{A.5}
$$

where r is now a point on the mirror transducer. The total signal recorded by the transducer due to the reflection is now given by:

$$V_{ref}(f) = R_{amp}T(f)\iint_{S_{mirror}} \frac{A(f)}{j\lambda} \iint_{s',r\in S_{mirror}} \frac{e^{jk|r-r'|}}{|r-r'|} ds' ds_{mirror}$$
$$= R_{amp}\frac{A(f)}{j\lambda}T(f)\iint_{S_{mirror}} ds_{mirror} \iint_{s',r\in S_{mirror}} \frac{e^{jk|r-r'|}}{|r-r'|} ds' \tag{A.6}$$

where R_{amp} is the amplitude reflection coefficient between the planar reflector and water. Now taking absolute value of the square of the above quantity we get

$$|V_{ref}(f)|^2 = R_{int}\left|\frac{A(f)}{j\lambda}\right|^2 |T(f)|^2 \left|\iint_{S_{mirror}} ds_{mirror} \iint_{s',r\in S_{mirror}} \frac{e^{jk|r-r'|}}{|r-r'|} ds'\right|^2 \tag{A.7}$$

where $R_{int} = R_{amp}^2$ is the intensity reflection coefficient between the planar reflector and water, which can be computed if the material properties of the reflector are known.

The backscatter coefficient of the tissue is given by

$$B(f) = N|\Phi(f)|^2 \tag{A.8}$$

The above quantity can now be obtained using Eq. (A.7) and (A.4) to give:

$$B(f) = \frac{|V_{tissue}^2(f)|^2 R_{\text{int}} \left|\iint_{S_{mirror}} ds_{mirror} \iint_{s',r\in S_{mirror}} \frac{e^{jk|r-r'|}}{|r-r'|} ds'\right|^2}{\iiint_{\Omega}\left|\iint_{s'} \frac{e^{jk|r-r'|}}{r-r'} ds'\right|^4 d\Omega} \tag{A.9}$$

To complete the derivation, we only need to add the effect of attenuation within the gate used in computing Fourier Transforms, and account for the signal loss due to the Hamming window function. Then the expression given in Eq. (3.9) is obtained.

Appendix B: On Estimating the Parameters of the Generalized Gamma Distribution

The three-parameter Generalized Gamma (GG) distribution is an interesting distribution in that it contains several simpler distributions as special cases, and provides two shape parameters for tissue characterization. However its parameters are more difficult to estimate, and in general show larger variability than those of other distributions commonly used in tissue characterization. This Appendix describes some aspects regarding the estimation of the parameters of the GG distribution using the method of moments and the maximum likelihood method. It is shown that when the skewness of the logarithm of data is outside the limits (-2, 0), the method of moments fails to provide a solution. It is also shown through examples that the maximum likelihood method also fails to provide a solution in certain cases. Using Monte-Carlo simulations it is shown that the maximum likelihood method provides better estimates than the method of moments, especially for small values of ν (~ 1). The difficulty in estimating ν for both the methods for large ν (~ 4) is demonstrated.

B.1 Method of moments (MOM)

The GG distribution is given by the following expression:

$$p(r)=\frac{cr^{(c\nu-1)}}{a^{c\nu}\Gamma(\nu)}e^{-\left(\frac{r}{a}\right)^{c}} \qquad r\geq 0 \qquad a,\nu,c>0 \tag{B.1}$$

The method of moments to estimate its parameters was first described by Stacy and Mihram [142] and requires solving the following three equations:

$$\frac{\psi''(\nu)}{[\psi'(\nu)]^{1.5}}=-\left|\frac{E\left[\left(\ln(r)-\overline{\ln(r)}\right)^{3}\right]}{\left\{E\left[\left(\ln(r)-\overline{\ln(r)}\right)^{2}\right]\right\}^{1.5}}\right| \tag{B.2}$$

$$c=\sqrt{\frac{\psi'(\nu)}{E\left[\left(\ln(r)-\overline{\ln(r)}\right)^{2}\right]}} \tag{B.3}$$

$$a = E(r)\frac{\Gamma(\nu)}{\Gamma\left(\nu+\frac{1}{c}\right)} \tag{B.4}$$

where $\psi(\nu) = \frac{\Gamma'(\nu)}{\Gamma(\nu)}$ is the digamma function, and $\Gamma(\nu)$ is the gamma function. To solve the above equations, the RHS of Eq. (B.2), which is the skewness of the logarithm of the data , is first computed. The estimate of ν is then obtained by solving the transcendental equation numerically. Once ν is obtained, c and a are obtained using Eqs. (B.3) and (B.4).

Under some conditions, a solution to Eq. (B.2) may not be possible. This is because the LHS of Eq. (B.2) is bounded between –2 and 0 whereas the RHS can in general take any negative value. To prove that the LHS is bounded, let us first compute the lower asymptotic limit when $\nu \to 0$. Consider the following series expansions for the first two derivatives of the digamma function [146] :

$$\psi'(\nu) = \sum_{k=0}^{\infty}\frac{1}{(\nu+k)^2} \tag{B.5}$$

$$\psi''(\nu) = -2\sum_{k=0}^{\infty}\frac{1}{(\nu+k)^3} \tag{B.6}$$

From the above we get

$$\begin{aligned}\frac{\psi''(\nu)}{(\psi'(\nu))^{1.5}} &= -2\frac{\left(\frac{1}{\nu^3}+\frac{1}{(\nu+1)^3}+\frac{1}{(\nu+2)^3}+\ldots\right)}{\left(\frac{1}{\nu^2}+\frac{1}{(\nu+1)^2}+\frac{1}{(\nu+2)^2}+\ldots\right)^{1.5}} \\ &= -2\frac{\left(1+\left(\frac{\nu}{\nu+1}\right)^3+\left(\frac{\nu}{\nu+2}\right)^3+\ldots\right)}{\left(1+\left(\frac{\nu}{\nu+1}\right)^2+\left(\frac{\nu}{\nu+2}\right)^2+\ldots\right)^{1.5}}\end{aligned} \tag{B.7}$$

Now taking the limit as $\nu \to 0$, we get

$$\lim_{\nu \to 0} \frac{\psi''(\nu)}{\left(\psi'(\nu)\right)^{1.5}} = -2 \tag{B.8}$$

To obtain the limit as $\nu \to \infty$, consider the series expansions for large ν [146]:

$$\psi'(\nu) \simeq \frac{1}{\nu} + \frac{1}{2\nu^2} + \frac{1}{6\nu^3} - \frac{1}{30\nu^5} + \frac{1}{42\nu^7} - \frac{1}{30\nu^9} + \ldots \qquad \nu \text{ large} \tag{B.9}$$

$$\psi''(\nu) \simeq -\frac{1}{\nu^2} - \frac{1}{\nu^3} - \frac{1}{2\nu^4} + \frac{1}{6\nu^6} - \frac{1}{6\nu^8} + \frac{3}{10\nu^{10}} - \frac{5}{6\nu^{12}} + \ldots \qquad \nu \text{ large} \tag{B.10}$$

Hence for large ν,

$$\begin{aligned} \frac{\psi''(\nu)}{\left(\psi'(\nu)\right)^{1.5}} &\simeq \frac{\left(-\frac{1}{\nu^2} - \frac{1}{\nu^3} - \frac{1}{2\nu^4} + \frac{1}{6\nu^6} - \frac{1}{6\nu^8} + \frac{3}{10\nu^{10}} - \frac{5}{6\nu^{12}} + \ldots\right)}{\left(\frac{1}{\nu} + \frac{1}{2\nu^2} + \frac{1}{6\nu^3} - \frac{1}{30\nu^5} + \frac{1}{42\nu^7} - \frac{1}{30\nu^9} + \ldots\right)^{1.5}} \\ &= \frac{\left(-1 - \frac{1}{\nu} - \frac{1}{2\nu^2} + \frac{1}{6\nu^4} - \frac{1}{6\nu^6} + \frac{3}{10\nu^8} - \frac{5}{6\nu^{10}} + \ldots\right)}{\sqrt{\nu}\left(1 + \frac{1}{2\nu} + \frac{1}{6\nu^2} - \frac{1}{30\nu^4} + \frac{1}{42\nu^5} - \frac{1}{30\nu^8} + \ldots\right)^{1.5}} \\ &= \frac{-1}{\sqrt{\nu}} \end{aligned} \tag{B.11}$$

Thus for large ν, the LHS is simply an inverse square root function. Now taking the limit as $\nu \to \infty$, we get

$$\lim_{\nu \to \infty} \frac{\psi''(\nu)}{\left(\psi'(\nu)\right)^{1.5}} = 0 \tag{B.12}$$

Having obtained the lower and upper asymptotic limits of the LHS, a straightforward plotting of the LHS function shows that it is monotonic and bounded between –2 and 0 (see Fig. 4.2). This implies that if the RHS is outside these limits, then *no solution exists*. Monte-Carlo simulations to verify that the MOM could indeed fail to yield a solution are presented in Section B.4.

B.2 Maximum likelihood method (MLM)

The maximum likelihood estimates are obtained by maximizing the log-likelihood function given by the following expression:

$$L(r_1, r_2, ..., r_N, a, \nu, c) = N \ln c - (c\nu - 1)\sum \ln r_i - \sum \left(\frac{r_i}{a}\right)^c - Nc\nu \ln a - N \ln \Gamma(\nu) \quad \text{(B.13)}$$

where r_i refers to a sample value, and N is the number of samples. By setting the first partial derivatives of the above expression with respect to c and a to zero we get

$$\nu = -\left\{ c\left(\frac{\sum \ln r_i}{N} - \frac{\sum r_i^c \ln r_i}{\sum r_i^c} \right) \right\}^{-1} \quad \text{(B.14)}$$

$$a = \left(\frac{\sum r_i^c}{N\nu} \right)^{1/c} \quad \text{(B.15)}$$

To obtain the estimates, the value of c that maximizes the log-likelihood function in Eq. (5.7) is first obtained. This optimization procedure can be implemented as a one-dimensional exhaustive search technique for c, as the other two parameters a and ν are known from Eqs. (5.9) and (5.8) once the solution space for c is chosen. Once the estimate of c is obtained, the estimates of ν and a are obtained using Eq. (5.8) and (5.9).

One problem with the ML method is that for some sets of data, the maximum of the likelihood function might occur at inadmissible boundaries such as $c = 0$ or $c = \infty$. These violate the constraints on the parameters and hence no ML solution exists in these cases. In practice the solution was found inadmissible for small but finite values of $c \sim 0.018$, as the corresponding values for a were 0 at the computer's precision, which was also inadmissible. To illustrate the MLM, and to show that in some cases solutions do not exist, 4 examples will now be presented. The first two are cases where the solution exists, and the next two are cases where no solution exists. The data for the four examples were as follows:

Data set 1:

0.4894	0.5381	0.9458	0.5115	0.7545	0.1026	0.7685	0.1117	0.5081	0.3701
1.0379	1.0144	0.2911	0.4809	0.6508	0.9623	0.4759	0.1665	0.9415	0.9117

0.7597 0.9327 1.1431 1.2566 1.4848 1.1166 0.5619 0.6714 0.7698 0.8240
0.8001 1.3940 0.7225 1.2626 0.4194 0.8768 0.7974 1.0090 0.3866 0.8077
0.6285 0.3238 0.2701 0.6877 0.5168 1.1832 1.1209 0.5364 0.8337 0.8077

Data set 2 [163], expressed in natural logarithm of the data:
0.216 -0.410 -1.064 -6.824 -0.758 4.054 0.032 1.262 -0.030 -2.640
0.438 2.208 -0.754 -0.684 -3.506 1.954 0.716 -1.686 -0.832 0.438

Data set 3:
1 2 3 4 5 6 7 8 9 10
11 12 13 14 15 16 17 18 19 20

Data set 4:
1.7004 2.3060 3.0967 1.4422 1.8927 1.8427 1.3323 2.2770 2.9700 1.0764
1.2298 1.2609 1.9310 1.8200 2.0940 1.9889 1.6170 1.0971 1.4590 1.0268
1.6479 1.9747 2.6232 1.9977 2.3441 1.6001 2.4848 2.6380 1.7846 1.8186
1.1817 1.4501 2.1128 1.8171 2.4596 2.2352 3.6193 1.5267 2.4195 1.4499
2.6537 1.7604 2.1651 2.7308 2.1268 1.4737 1.5511 1.5249 1.5695 1.4657

Figure B.1 shows the log-likelihood function for the four examples as a function of c. In the first example, a unique extremum exists, which also happens to be the maximum. In the second example, two extrema are obtained, one corresponding to the maximum and the other corresponding to the minimum. Wingo [145] has also analyzed this data set and stated that the two extrema correspond to local maxima, but his second maximum actually corresponds to a minimum of the log-likelihood function. The third example shows that the maximum of the log-likelihood function could occur at $c = \infty$. While numerically it is not possible to prove that the solution is indeed occurring at ∞ unless the exhaustive search is extended up to ∞, from a practical standpoint, a finite solution was unobtainable. The fourth example shows that the maximum of the likelihood function could occur at $c = 0$. Thus in the third and fourth cases, the ML solution does not exist. The interested reader could verify these cases as the full data sets have been provided. It should also be pointed out that these examples are based on very few data samples compared to what is normally available in ultrasonic tissue characterization studies, and should not necessarily imply a serious limitation with the MLM.

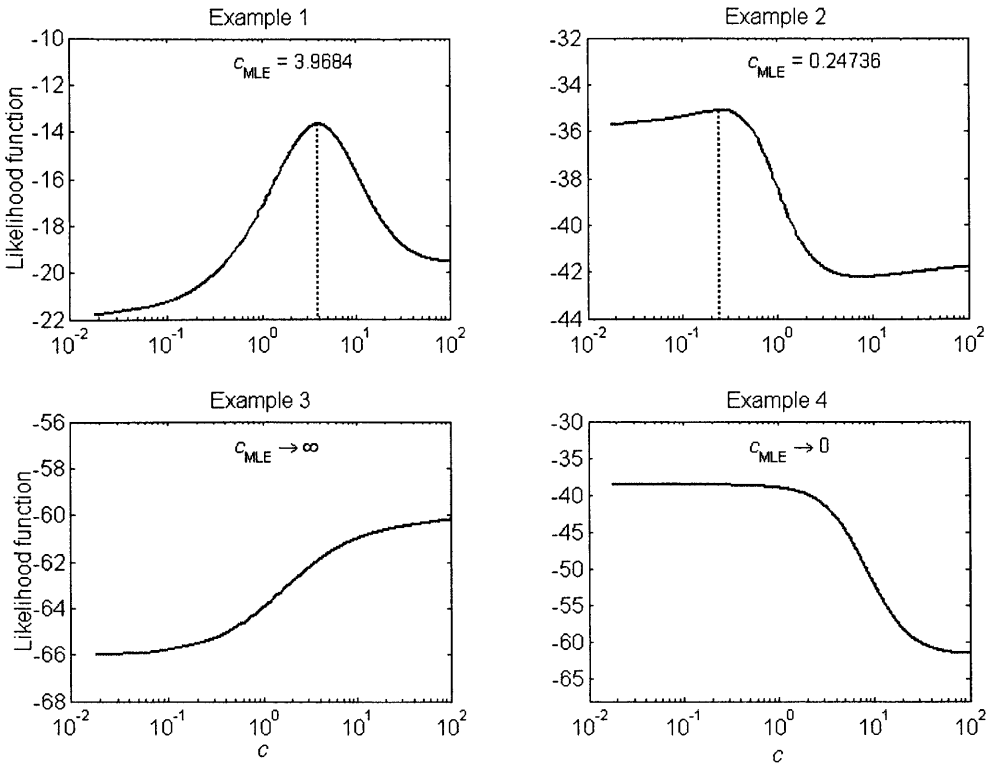

Figure B.1: Four examples to illustrate the Maximum Likelihood Method of estimation of the GG-*c* parameter. The estimated values of the parameter *c* are shown in the figures.

B.3 Monte-Carlo simulations

In order to further illustrate the above aspects, and to study variability issues in estimating the GG parameters, Monte-Carlo simulations were performed using random number generators, and both the MOM and MLM estimates were obtained. GG random numbers were obtained from the usual gamma random numbers using a simple transformation. For instance, let the random variable x be distributed according to the usual gamma distribution with parameters a and ν:

$$p(x) = \frac{x^{(\nu-1)} e^{-\frac{x}{a}}}{\Gamma(\nu) a^{\upsilon}} \tag{B.16}$$

Then a new random variable obtained by the following transformation

$$r = x^{\frac{1}{c}} \tag{B.17}$$

is GG distributed with parameters a^c, ν, and c [164]. Thus by using the usual gamma random number generator available in Matlab, GG random numbers were generated.

Monte-Carlo simulations were done for fixed values of $a = 1$ and $c = 2$, for eight values of ν=0.5, 1.0, 1.5, 2.0, 2.5, 3.0, 3.5, and 4.0. For each ν, simulations were done for eleven sample sizes N=100, 150, 200, 300, 400, 600, 800, 1200, 1600, 2400, and 3600. For all the above 88 cases, 1000 repetitions were done in order to study the variance in the estimates. Thus a total of 88,000 set of estimates (both MOM and MLM) were obtained. For later convenience, we will refer to values of ν around 1 as "small ν" and to values around 4 as "large ν".

Figure B.2 shows the number of cases for which no solution was possible for all the ν's, and for four sample sizes. It can be seen that the MOM did not yield a solution in several cases. The MLM yielded a solution in almost all cases, except for the case of $N = 200$ and large ν. For all sample sizes, the above problem with MOM decreased with increasing values of ν.

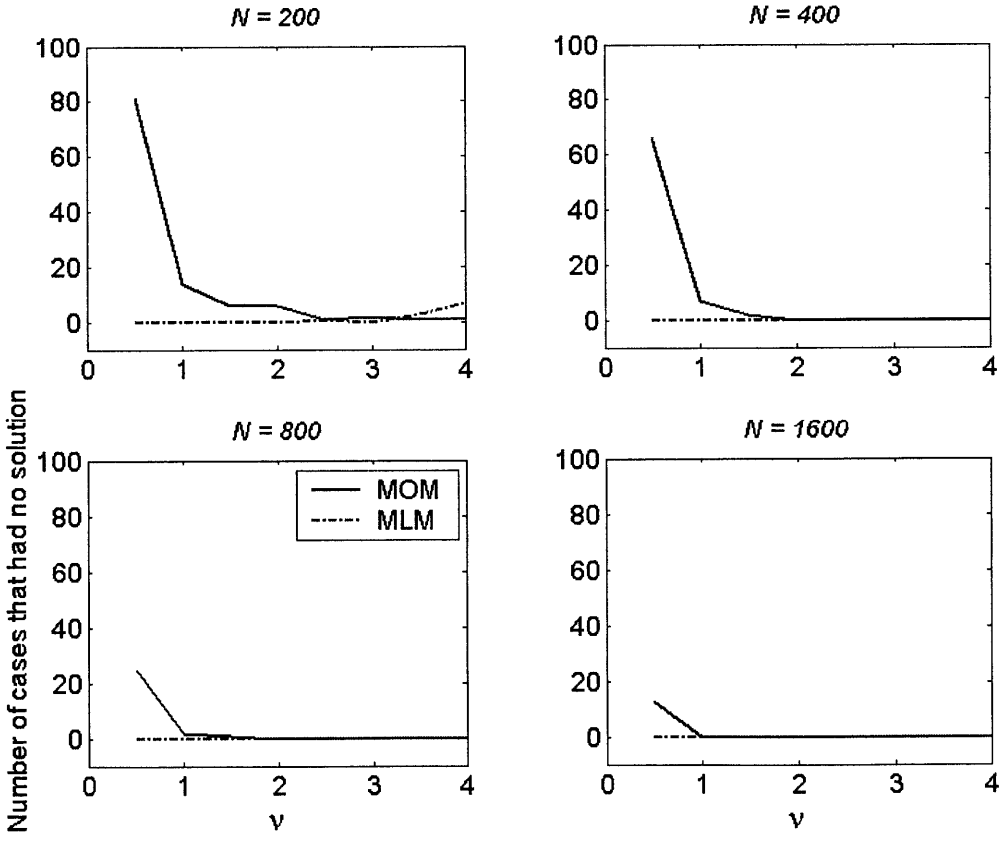

Figure B.2: Number of cases, among 1000 trials, for which the Method of Moments (MOM) and the Maximum Likelihood Method (MLM) did not yield any solution. The x-axis is the true value of the parameter ν used in the random number generation. The sample size N is indicated on top of each panel.

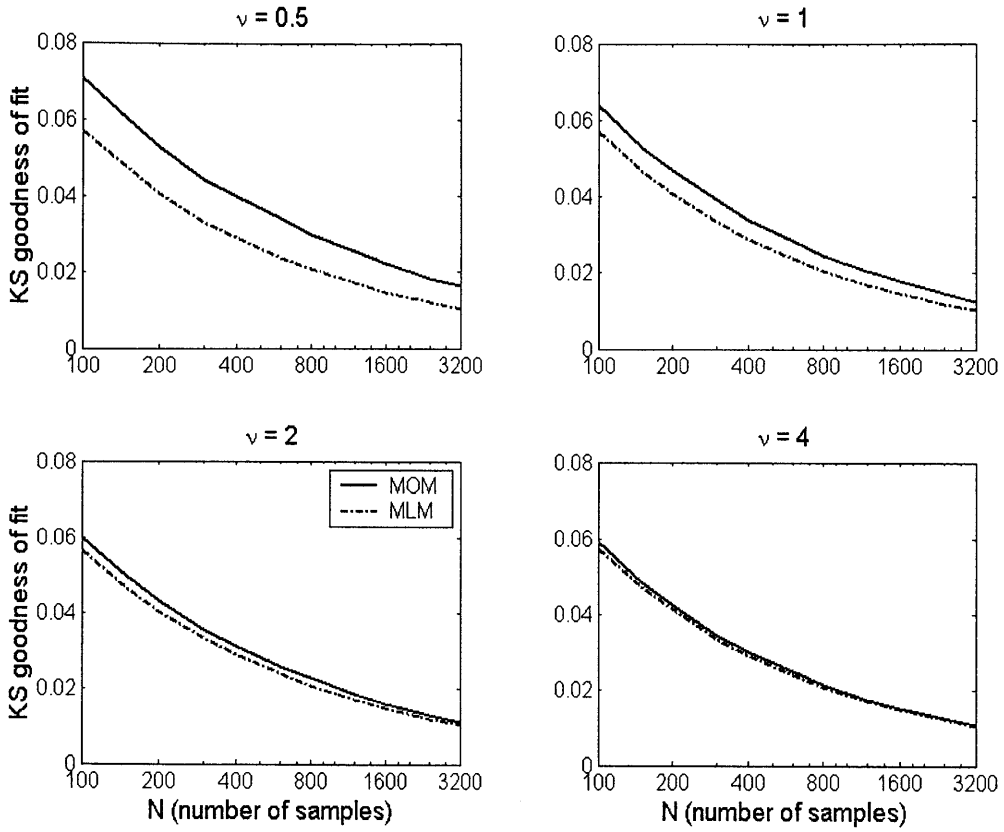

Figure B.3: Kolmogorov-Smirnov (KS) goodness of fit measures for the Method of Moments (MOM) and Maximum Likelihood method as a function of *N* for four values of ν.

Figure B.3 shows the Kolmogorov-Smirnov (KS) goodness of fit for both the MOM and MLM, for $\nu = 0.5, 1, 2,$ and 4. It can be seen that the MLM always gave a smaller KS value than the MOM, implying that its pdf fit was closer to the actual histogram than that of the MOM. The difference in KS values between the two methods is more pronounced for smaller ν, but for large ν both the methods yield similar goodness of fits. As expected, for every ν, the performance of both the methods improves with increasing *N*.

Figure B.4 shows the performance of the estimate of ν as a function of sample size for two cases corresponding to ν=1 and 4. For both the cases, the MLM estimates were closer to the true values on the average and had smaller variability compared to the MOM estimates. When the true value of ν was 4, occasionally large values of the estimates were obtained for both the methods, which lead to very large mean estimates, even higher than the 95th percentile points. Such occasional large values for the estimate of ν when its true value is large have also been mentioned by

previous researchers [149]. Figures B.5 and B.6 further illustrate the problem in estimating ν when its true value is even moderately large. In general, the ML estimates are asymptotically normal [165], and the histogram of the estimates should show a normal distribution for large sample sizes. In Figure B.5, when ν=1, the histogram of the estimates is normal when the sample size was 3200. However in Figure B.6, when ν=4, even for a sample size of 3200, the histogram was not normal, but skewed towards the right. Thus when the true value of ν is large, a very large sample size might be needed to reach asymptotically normal distribution its estimate. Figure B.7 shows the estimated values of the other shape parameter c. Once again the MLM shows better performance in that the variability of its estimates is smaller than those of the MOM. However, unlike in the case of estimating ν, occasional large values do not occur.

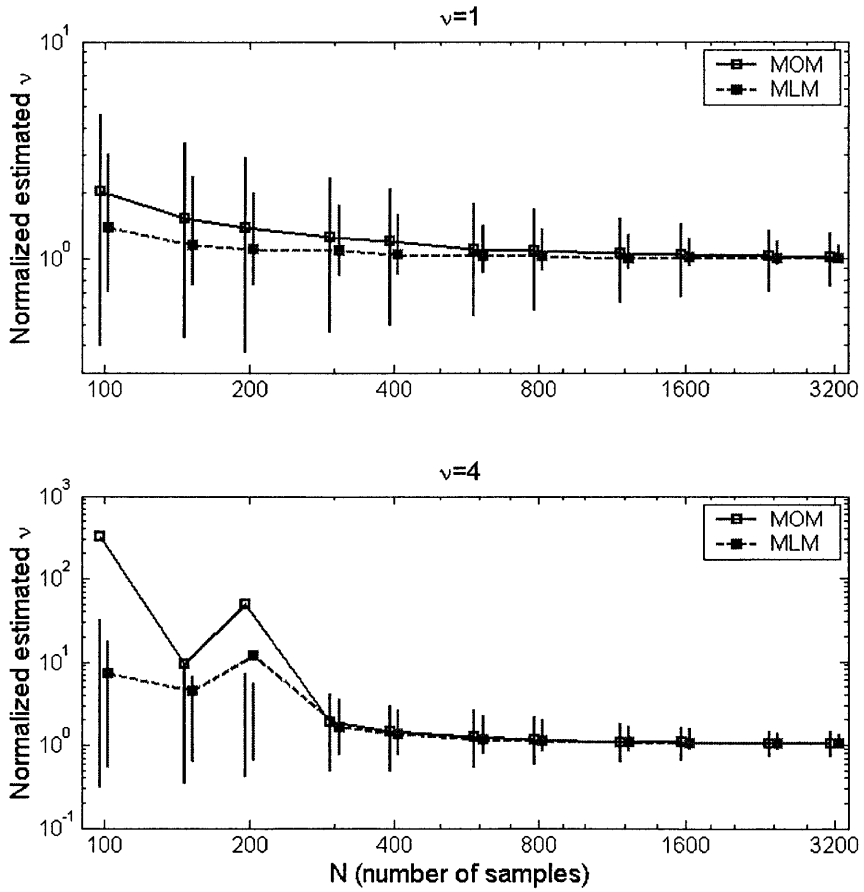

Figure B.4: Variability in the estimated values of ν as a function of sample size N. Results are shown for two cases corresponding to true values of ν=1 and 4. The markers indicate the mean of the estimates based on 1000 Monte-Carlo trials. The error bars indicate the extent of estimated values between the 5th and 95th percentile points. In some cases (for true ν=4, N≤200), the mean estimates are seen to be higher than the 95th percentile points, due to occasionally large estimates.

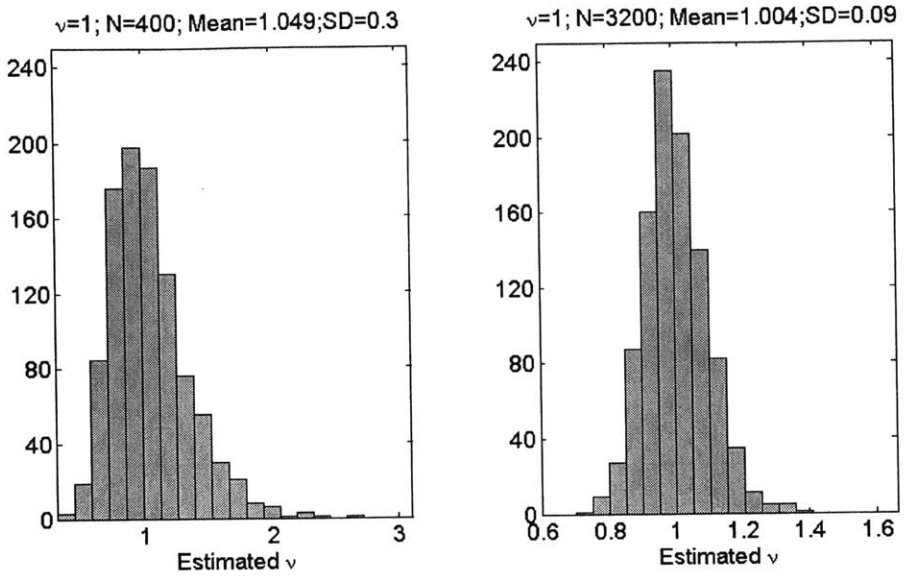

Figure B.5: Histogram of estimated values of ν for two sample sizes (N=400 and 3200). The true value of ν was 1 in both cases and the estimates were obtained using the MLM.

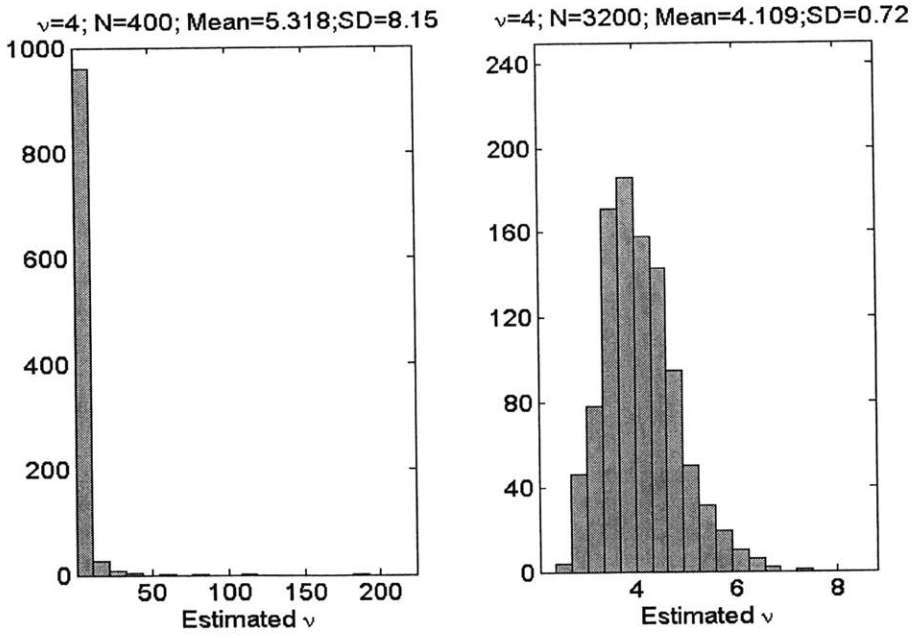

Figure B.6: Histogram of estimated values of ν for two sample sizes (N=400 and 3200). The true value of ν was 4 in both cases and the estimates were obtained using the MLM.

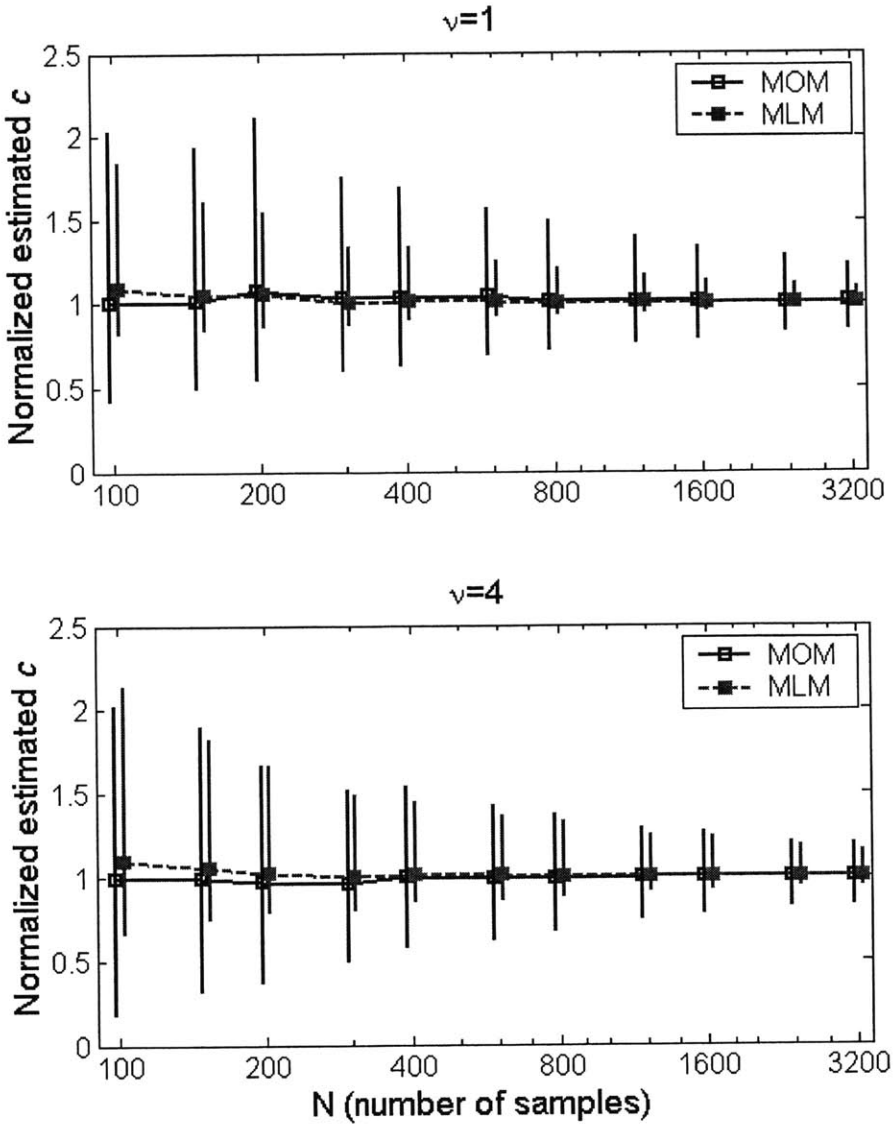

Figure B.7: Variability in the estimated values of *c* as a function of sample size N. Results are shown for two cases corresponding to true values of ν=1 and 4. The markers indicate the mean of the estimates based on 1000 Monte-Carlo trials. The error bars signify the extent of estimated values between the 5th and 95th percentile points.

B.4 Summary of results

This appendix provided several useful results regarding estimation of the parameters of the GG distribution:

- Both the MOM and MLM methods may fail to provide solutions. In practice, such failures occur more for the MOM than MLM, especially for small ν and small *N*.

- The MLM is in general better than the MOM in terms of the KS goodness of fit, especially for small ν. For large ν, both the methods give comparable goodness of fits.
- The MLM always gives better estimates (smaller bias and smaller variance) than the MOM, at least for the cases analyzed here.
- Reliable estimation of ν is hard when its true value is large due to the possibility of occasionally very large estimates. This is true for both the MOM and MLM. When the true value of ν is large, a very large sample size might be needed for estimating the parameter ν reliably.

These results should be useful to researchers in many fields including radar, communications, sonar, and medical ultrasound, where the estimation of the GG parameters is needed.

References

[1] H. K. Koh, "Cutaneous melanoma", *New England Journal of Medicine*, vol. 325, pp. 171-182, 1991.

[2] D. S. Preston and R. S. Stern, "Nonmelanoma cancers of the skin", *New England Journal of Medicine*, vol. 327, pp. 1649-1662, 1992.

[3] E. P. van der Esch, *et al.*, "Temporal change in diagnostic criteria as a cause of the increase of malignant melanoma over time is unlikely", *International Journal of Cancer*, vol. 47, pp. 483-490, 1991.

[4] http://www.whitehouse.gov/news/releases/2001/02/20010207-6.html

[5] R. U. Peter, O. Braun-Falco, A. Birioukov, N. Hacker, M. Kerscher, U. Peterseim, T. Ruzicka, B. Konz, and G. Plewig, "Chronic cutaneous damage after accidental exposure to ionizing radiation: the Chernobyl experience", *Journal of the American Academy of Dermatology*, vol. 30, pp. 719-723, 1994.

[6] P. Gottlober, M. J. Kerscher, H. C. Korting, and R. U. Peter, "Sonographic determination of cutaneous and subcutaneous fibrosis after accidental exposure to ionising radiation in the course of the Chernobyl nuclear power plant accident", *Ultrasound in Medicine and Biology*, vol. 23, pp. 9-13, 1997.

[7] M. A. Srinivasan and R. H. LaMotte, "Tactile discrimination of shape: Responses of slowly and rapidly adapting mechanoreceptive afferents to a step indented into the monkey fingerpad", *Journal of Neuroscience*, vol. 7, pp. 1682-1697, 1987.

[8] B. I. Raju and M. A. Srinivasan, *Encoding and decoding of shape in tactile sensing*, MIT: Research Laboratory of Electronics Technical Report-630, 1999.

[9] J. Ophir, I. Cespedes, H. Ponnekanti, Y. Yazdi, and Z. Li, "Elastography: a quantitative method for imaging the elasticity of biological tissues", *Ultrasonic Imaging*, vol. 13, pp. 111-134, 1991.

[10] G. Odland, *Structure of the Skin*, in *Physiology, Biochemistry, and Molecular Biology of the Skin*, L. Goldsmith, Editor. 1991, Oxford University Press: New York. pp. 3-62.

[11] M. Rajadhyaksha, M. Grossman, D. Esterowitz, R. H. Webb, and R. R. Anderson, "In vivo confocal scanning laser microscopy of human skin: melanin provides strong contrast", *Journal of Investigative Dermatology*, vol. 104, pp. 946-952, 1995.

[12] M. Rajadhyaksha, S. Gonzalez, J. M. Zavislan, R. R. Anderson, and R. H. Webb, "In vivo confocal scanning laser microscopy of human skin II: Advances in instrumentation and comparison with histology", *Journal of Investigative Dermatology*, vol. 113, pp. 293-303, 1999.

[13] D. Huang, E. Swanson, C. P. Lin, J. S. Schuman, W. G. Stinson, W. Chang, M. R. Hee, T. Flotte, K. Gregory, C. A. Puliafito, and J. G. Fujimoto, "Optical Coherence Tomography", *Science*, vol. 254, pp. 1178-1181, 1991.

[14] J. Welzel, E. Lankenau, R. Birngruber, and R. Engelhardt, "Optical coherence tomography of the human skin", *Journal of the American Academy of Dermatology*, vol. 37, pp. 958-963, 1997.

[15] B. D. Fornage, M. H. McGavran, M. Duvic, and C. A. Waldron, "Imaging of the skin with 20-MHz US", *Radiology*, vol. 189, pp. 69-76, 1993.

[16] T. Cammarota, F. Pinto, A. Magliaro, and A. Sarno, "Current uses of diagnostic high-frequency US in dermatology", *European Journal of Radiology*, vol. 27, pp. 215-223, 1998.

[17] D. H. Turnbull, B. G. Starkoski, K. A. Harasiewicz, J. l. Semple, L. From, A. K. Gupta, D. N. Sauder, and F. S. Foster, "A 40-100 B-scan ultrasound backscatter microscope for skin imaging", *Ultrasound in Medicine and Biology*, vol. 21, pp. 79-88, 1995.

[18] K. Hoffmann, J. Jung, S. El Gammal, and P. Altmeyer, "Malignant melanoma in 20 MHz B scan sonography", *Dermatology*, vol. 185, pp. 49-55, 1992.

[19] S. Seidenari and B. Belletti, "The quantification of patch test responses: A comparison between echographic and calorimetric methods", *Acta dermato-venereaologica*, vol. 78, pp. 364-366, 1998.

[20] M. Gniadecka and G. B. E. Jemec, "Quantitative evaluation of chronological ageing and photoageing in vivo: studies on skin echogenicity and thickness", *British Journal of Dermatology*, vol. 139, pp. 815-821, 1998.

[21] C. M. Moran, N. L. Bush, and J. C. Bamber, "Ultrasonic propagation properties of excised human skin", *Ultrasound in Medicine and Biology*, vol. 21, pp. 1177-1190, 1995.

[22] S. Leeman, L. Ferrari, J. P. Jones, and M. Fink, "Perspectives on attenuation estimation from pulse-echo signals", *IEEE Transactions on Sonics and Ultrasonics*, vol. 31, pp. 352-360, 1984.

[23] M. F. Insana and D. G. Brown, *Acoustic scattering theory applied to soft biological tissues*, in *Ultrasonic Scattering in Biological Tissues*, K.K. Shung and G.A. Thieme, Editors. 1993, CRC Press: Boca Raton, FL. pp. 75-124.

[24] J. A. Campbell and R. C. Waag, "Normalization of ultrasonic scattering measurements to obtain average differential scattering cross sections for tissues", *Journal of the Acoustical Society of America*, vol. 74, pp. 393-399, 1983.

[25] T. J. Hall, E. L. Madesn, J. A. Zagzebski, and E. V. Boote, "Accurate depth-independent determination of acoustic backscatter coefficients with focused transducers", *Journal of the Acoustical Society of America*, vol. 85, pp. 2410-2416, 1989.

[26] M. F. Insana, R. F. Wagner, D. G. Brown, and T. J. Hall, "Describing small-scale structure in random media using pulse-echo ultrasound", *Journal of the Acoustical Society of America*, vol. 87, pp. 179-192, 1990.

[27] F. L. Lizzi, M. Greenebaum, E. J. Feleppa, M. Elbaum, and D. J. Coleman, "Theoretical framework for spectrum analysis in ultrasonic tissue characterization", *Journal of the Acoustical Society of America*, vol. 73, pp. 1366-1373, 1983.

[28] F. L. Lizzi, M. Ostromogilsky, E. J. Feleppa, M. C. Rorke, and M. M. Yaremko, "Relationship of ultrasonic spectral parameters to features of tissue microstructure", *IEEE Transactions on Ultrasonics, Ferroelectrics, and Frequency Control*, vol. 34, pp. 319-329, 1987.

[29] E. L. Madsen, M. F. Insana, and J. A. Zagzebski, "Method of data reduction for accurate determination of acoustic backscatter coefficients", *Journal of the Acoustical Society of America*, vol. 76, pp. 913-923, 1984.

[30] R. A. Sigelmann and J. M. Reid, "Analysis and measurement of ultrasound backscattering from an ensemble of scatterers excited by sine-wave bursts", *Journal of the Acoustical Society of America*, vol. 53, pp. 1351-1355, 1973.

[31] Y. W. Yuan and K. K. Shung, "The effect of focusing on ultrasonic backscatter measurements", *Ultrasonic Imaging*, vol. 8, pp. 121-130, 1986.

[32] J.-F. Chen, J. A. Zagzebski, and E. L. Madsen, "Tests of backscatter coefficient measurement using broadband pulses", *IEEE Transactions on Ultrasonics, Ferroelectrics, and Frequency Control*, vol. 40, pp. 603-607, 1993.

[33] K. K. Shung and G. A. Thieme, *Ultrasonic Scattering in Biological Tissues*, Boca Raton, Florida: CRC Press, 1993.

[34] C. B. Burckhardt, "Speckle in ultrasound B-mode scans", *IEEE Transactions on Sonics and Ultrasonics*, vol. SU-25, pp. 1-6, 1978.

[35] J. G. Abbott and F. L. Thurstone, "Acoustic speckle: Theory and experimental analysis", *Ultrasonic Imaging*, vol. 1, pp. 303-324, 1979.

[36] G. E. Sleefe and P. P. Lele, "Tissue characterization based on scatterer number density estimation", *IEEE Transactions on Ultrasonics, Ferroelectrics, and Frequency Control*, vol. 35, pp. 749-757, 1988.

[37] V. Dutt and J. Greenleaf, "Ultrasound echo envelope analysis using a homodyned K distribution signal model", *Ultrasonic Imaging*, vol. 16, pp. 265-287, 1994.

[38] P. M. Shankar, J. M. Reid, H. Ortega, C. W. Piccoli, and B. B. Goldberg, "Use of non-Rayleigh statistics for the identification of tumors in ultrasonic B-Scans of the breast", *IEEE Transactions on Medical Imaging*, vol. 12, pp. 687-692, 1993.

[39] R. F. Wagner, M. Insana, and D. Brown, "Unified approach to the detection and classification of speckle texture in diagnostic ultrasound", *Optical engineering*, vol. 25, pp. 738-742, 1986.

[40] N. A. H. K. Rao, S. Venkataraman, and M. Helguera, "On understanding the relationship between ultrasound speckle and the scattering microstructure", *Acoustical Imaging*, vol. 23, pp. 391-398, 1997.

[41] T. A. Tuthill, R. H. Sperry, and K. J. Parkar, "Deviations from Rayleigh statistics in ultrasonic speckle", *Ultrasonic Imaging*, vol. 10, pp. 81-89, 1988.

[42] K. A. Wear, R. F. Wagner, D. G. Brown, and M. F. Insana, "Statistical properties of estimates of signal-to-noise ratio and number of scatterers per resolution cell", *Journal of the Acoustical Society of America*, vol. 102, pp. 635-641, 1997.

[43] J. W. Goodman, "Some fundamental properties of speckle", *Journal of the Optical Society of America*, vol. 66, pp. 1145-1150, 1976.

[44] J. C. Dainty, *Laser Speckle and Related Phenomena*, New York: Springler-Verlag, 1984.

[45] E. Jakeman and P. N. Pusey, "A model for non-Rayleigh sea echo", *IEEE Transactions on Antennas and Propagation*, vol. AP-24, pp. 806-814, 1976.

[46] E. Conte, M. Longo, and M. Lops, "Modeling and Simulation of non-Rayleigh radar clutter", *IEE Proceedings (F)*, vol. 138, pp. 121-130, 1991.

[47] M. Nakagami, *The m-distribution - A general formula of intensity distribution of rapid fading*, in *Statistical Methods in Radio Wave Propagation*, W.C. Hoffman, Editor. 1960, Permagon Press: New York. pp. 3-36.

[48] J. Miller, *et al.*, "Backscatter imaging and myocardial tissue characterization", *IEEE Ultrasonics Symposium,* 1998, pp. 1373-1383.

[49] M. O'Donnell, J. W. Mimbs, and J. G. Miller, "Relationship between collagen and ultrasonic backscatter in myocardial tissue", *Journal of the Acoustical Society of America*, vol. 69, pp. 580-588, 1981.

[50] I. Y. Kuo and K. K. Shung, "High frequency ultrasonic backscatter from erythrocyte suspension", *IEEE Transactions on Biomedical Engineering*, vol. 41, pp. 29-34, 1994.

[51] J. C. Bamber and C. R. Hill, "Acoustic properties of normal and cancerous human liver - I. Dependence on pathological condition", *Ultrasound in Medicine and Biology*, vol. 7, pp. 121-133, 1981.

[52] J. A. Campbell and R. C. Waag, "Measurements of calf liver ultrasonic differential and total scattering cross sections", *Journal of the Acoustical Society of America*, vol. 75, pp. 603-611, 1984.

[53] R. Kuc and M. Schwartz, "Estimating the acoustic attenuation coefficient slope for liver from reflected ultrasound signals", *IEEE Transactions on Sonics and Ultrasonics*, vol. SU-26, pp. 353-362, 1979.

[54] F. L. Lizzi, D. L. King, M. C. Rorke, J. Hui, M. Ostromogilsky, M. M. Yaremko, E. J. Feleppa, and P. Wai, "Comparison of theoretical scattering results and ultrasonic data from clinical liver examinations", *Ultrasound in Medicine and Biology*, vol. 14, pp. 377-385, 1988.

[55] S. G. Ye, K. A. Harasiewicz, C. J. Pavlin, and F. S. Foster, "Ultrasound characterization of normal ocular tissue in the frequency range from 50 MHz to 100 MHz", *IEEE Transactions on Ultrasonics, Ferroelectrics, and Frequency Control*, vol. 42, pp. 8-14, 1995.

[56] R. H. Silverman, R. Folberg, H. C. Boldt, H. O. Lloyd, M. J. Rondeau, M. G. Mehaffey, F. L. Lizzi, and D. J. Coleman, "Correlation of ultrasound parameter imaging with microcirculatory patterns in uveal melanomas", *Ultrasound in Medicine and Biology*, vol. 23, pp. 573-581, 1997.

[57] R. L. Romijn, J. M. Thijssen, B. J. Oosterveld, and A. M. Verbeek, "Ultrasonic differentiation of intraocular melanomas: Parameters and estimation methods", *Ultrasonic Imaging*, vol. 13, pp. 27-55, 1991.

[58] M. F. Insana, T. J. Hall, J. G. Wood, and Z.-Y. Yan, "Renal ultrasound using parametric imaging techniques to detect changes in microstructure and function", *Investigative Radiology*, vol. 28, pp. 720-725, 1993.

[59] T. J. Hall, M. F. Insana, L. A. Harrison, and G. G. Cox, "Ultrasonic measurement of glomerular diameters in normal adult humans", *Ultrasound in Medicine and Biology*, vol. 22, pp. 987-997, 1996.

[60] L. L. Fellingham and F. G. Sommer, "Ultrasonic characterization of tissue structure in the In Vivo human liver and spleen", *IEEE Transactions on Sonics and Ultrasonics*, vol. SU-31, pp. 418-428, 1984.

[61] F. T. D'Astous and F. S. Foster, "Frequency dependence of ultrasound attenuation and backscatter in breast tissue", *Ultrasound in Medicine and Biology*, vol. 12, pp. 795-808, 1986.

[62] E. Cherin, A. Saied, P. Laugier, P. Netter, and G. Berger, "Evaluation of acoustical parameter sensitivity to age-related and osteoarthritic changes in articular cartilage using 50 MHz ultrasound", *Ultrasound in Medicine and Biology*, vol. 24, pp. 341-354, 1998.

[63] B. K. Hoffmeister, E. D. Verdonk, S. A. Wickline, and J. G. Miller, "Effect of collagen on the anisotropy of quasi-longitudinal mode ultrasonic velocity in fibrous soft tissues: A comparison of fixed tendon and fixed myocardium", *Journal of the Acoustical Society of America*, vol. 96, pp. 1957-1964, 1994.

[64] L. S. Wilson, M. L. Neale, H. E. Talhami, and M. Appleberg, "Preliminary results from attenuation-slope mapping of plaque using intravascular ultrasound", *Ultrasound in Medicine and Biology*, vol. 20, pp. 529-542, 1994.

[65] L. Landini, R. Sarnelli, E. Picano, and M. Salvadori, "Evaluation of frequency dependence of backscatter coefficient in normal and atherosclerotic aortic walls", *Ultrasound in Medicine and Biology*, vol. 12, pp. 397-401, 1986.

[66] C. R. Meyer, D. S. Herron, P. L. Carson, R. A. Banjavic, G. A. Thieme, F. L. Bookstein, and M. L. Johnson, "Estimation of ultrasonic attenuation and mean backscatterer size via digital signal processing", *Ultrasonic Imaging*, vol. 6, pp. 11-23, 1984.

[67] G. A. Thieme, R. A. Banjavic, M. L. Johnson, C. R. Meyer, G. W. Silvers, D. S. Herron, and P. L. Carson, "Sonographic identification of lung maturation in the fetal lamb", *Investigative Radiology*, vol. 18, pp. 18-26, 1983.

[68] C.-Y. Wang and K. K. Shung, "Variation in ultrasonic backscattering from sketal muscle during passive stretching", *IEEE Transactions on Ultrasonics, Ferroelectrics, and Frequency Control*, vol. 45, pp. 504-510, 1998.

[69] V. Dutt, R. R. Kinnick, R. Muthupillai, T. E. Oliphant, R. L. Ehman, and J. F. Greenleaf, "Acoustic shear-wave imaging using echo ultrasound compared to magnetic resonance elastography", *Ultrasound in Medicine and Biology*, vol. 26, pp. 397-403, 2000.

[70] D. Zhang, X.-F. Gong, and X. Chen, "Experimental imaging of the acoustic nonlinearity parameter B/A for biological tissues via a parametric array", *Ultrasound in Medicine and Biology*, vol. 27, pp. 1359-1365, 2001.

[71] C. C. Harland, J. C. Bamber, B. A. Gusterson, and P. S. Mortimer, "High frequency, high resolution B-scan ultrasound in the assessment of skin tumours", *British Journal of Dermatology*, vol. 128, pp. 525-532, 1993.

[72] C. Edwards, M. M. Al-Aboosi, and R. Marks, "The use of A-scan ultrasound in the assessment of small skin tumours", *British Journal of Dermatology*, vol. 121, pp. 297-304, 1989.

[73] H. Ihn, M. Shimozuma, M. Fujimoto, S. Sato, K. Kikuchi, A. Igarashi, Y. Soma, K. Tamaki, and K. Takehara, "Ultrasound measurement of skin thickness in systemic sclerosis", *British Journal of Rheumatology*, vol. 34, pp. 535-538, 1995.

[74] A. K. Gupta, D. H. Turnbull, K. A. Harasiewicz, D. T. Shun, G. N. Watteel, F. S. Foster, and D. N. Sauder, "The use of high-frequency ultrasound as a method of assessing the severity of a plaque of psoriasis", *Archives of Dermatology*, vol. 132, pp. 658-662, 1996.

[75] L. Vaillant, M. Berson, L. Machet, A. Callens, L. Pourcelot, and G. Lorette, "Ultrasound imaging of psoriatic skin: A noninvasive technique to evaluate treatment of psoriasis", *International Journal of Dermatology*, vol. 33, pp. 786-790, 1994.

[76] J. H. Cantrell, R. E. Goans, and R. L. Roswell, "Acoustic impedance variations at burn-nonburn interfaces in porcine skin", *Journal of the Acoustical Society of America*, vol. 64, pp. 731-735, 1978.

[77] J. de Rigal, C. Escoffier, B. Querleux, B. Faivre, P. Agache, and J.-L. Leveque, "Assessment of aging of the human skin by in vivo ultrasonic imaging", *Journal of Investigative Dermatology*, vol. 93, pp. 621-625, 1989.

[78] J. Levy, J. Gassmuller, G. Schroder, H. Audring, and N. Sonnichsen, "Comparison of the effects of calcipotriol, predicarbate, and clobetasol 17-propionate on normal skin assessed by ultrasound measurement of skin thickness", *Skin Pharmacology*, vol. 7, pp. 231-236, 1994.

[79] C. Passmann and H. Ermert, "A 100-MHz ultrasound imaging system for dermatologic and ophthalmologic diagnostics", *IEEE Transactions on Ultrasonics, Ferroelectrics, and Frequency Control*, vol. 43, pp. 545-552, 1996.

[80] F. S. Foster, G. R. Lockwood, L. K. Ryan, K. A. Harasiewicz, L. Berube, and A. M. Rauth, "Principles and applications of ultrasound backscatter microscopy", *IEEE Transactions on Ultrasonics, Ferroelectrics, and Frequency Control*, vol. 40, pp. 608-617, 1993.

[81] S. El Gammal, C. El Gammal, K. Kasper, C. Pieck, P. Altmeyer, M. Vogt, and H. Ermert, "Sonography of the skin at 100 MHz enables in vivo visualization of stratum corneum and viable epidermis in palmar skin and psoriatic plaques", *Journal of Investigative Dermatology*, vol. 113, pp. 821-829, 1999.

[82] J. E. Olerud, W. O'Brien, M. A. Riederer-Henderson, D. Steiger, F. K. Forster, C. Daly, D. J. Ketterer, and G. F. Odland, "Ultrasonic assessment of skin and wounds with the scanning laser acoustic microscope", *Journal of Investigative Dermatology*, vol. 88, pp. 615-623, 1987.

[83] M. A. Riederer-Henderson, J. E. Olerud, W. D. O'Brien, F. K. Forster, D. L. Steiger, D. J. Ketterer, and G. F. Odland, "Biochemical and acoustical parameters of normal canine skin", *IEEE Transactions on Biomedical Engineering*, vol. 35, pp. 967-972, 1988.

[84] F. K. Forster, J. E. Olerud, M. A. Riederer-Henderson, and A. W. Holmes, "Ultrasonic assessment of skin and surgical wounds utilizing backscatter acoustic techniques to estimate attenuation", *Ultrasound in Medicine and Biology*, vol. 16, pp. 43-53, 1990.

[85] J. E. Olerud, W. D. O'Brien, M. A. Riederer-Henderson, D. L. Steiger, and J. R. Debel, "Correlation of tissue constituents with the acoustic properties of skin and wound", *Ultrasound in Medicine and Biology*, vol. 16, pp. 55-64, 1990.

[86] T. Baldeweck, P. Laugier, and G. Berger, "An in vitro study on porcine skin: Attenuation profile estimation using auto-regressive modeling", *IEEE Ultrasonics Symposium*, vol. 2, pp. 1141-1144, 1995.

[87] L. Pan, L. Zan, and F. S. Foster, "Ultrasonic and viscoelastic properties of skin under transverse mechanical stress *in vitro*", *Ultrasound in Medicine and Biology*, vol. 24, pp. 995-1007, 1998.

[88] C. Guittet, F. Ossant, L. Vaillant, and M. Berson, "In vivo high frequency ultrasonic characterization of human dermis", *IEEE Transactions on Biomedical Engineering*, vol. 46, pp. 740-746, 1999.

[89] P. M. Shankar, "Ultrasonic tissue characterization using a generalized Nakagami model", *IEEE Transactions on Ultrasonics, Ferroelectrics, and Frequency Control*, vol. 48, pp. 1716-1720, 2001.

[90] G. S. Kino, *Acoustic Waves: Devices, Imaging, and Analog Signal Processing*, Englewood Cliffs, New Jersey: Prentice-Hall, 1987.

[91] B. I. Raju and M. A. Srinivasan, *Ultrasound backscatter microscope for in vivo imaging of human fingertip*, MIT: Research Laboratory of Electronics Technical Report-631, 1999.

[92] B. I. Raju and M. A. Srinivasan, "High frequency ultrasonic attenuation and backscatter coefficients of in vivo normal human dermis and subcutaneous fat", *Ultrasound in Medicine and Biology*, vol. 27, pp. 1543-1556, 2001.

[93] J. C. Bamber, *Attenuation and absorption*, in *Physical Principles of Medical Ultrasonics*, C.R. Hill, Editor. 1986, Ellis Horwood: Chichester. pp. 118-199.

[94] J. Greenleaf and C. Sehgal, *Biological System Evaluation with Ultrasound*, New York: Springer-Verlag, 1992.

[95] M. E. Lyons and K. J. Parker, "Absorption and attenuation in soft tissues: II. Experimental results", *IEEE Transactions on Ultrasonics, Ferroelectrics, and Frequency Control*, vol. 35, pp. 511-521, 1988.

[96] J. A. Zagzebski, L. X. Yao, E. J. Boote, and Z. F. Lu, *Quantitative backscatter imaging*, in *Ultrasonic Scattering in Biological Tissues*, K.K. Shung and G.A. Thieme, Editors. 1993, CRC Press: Boca Raton. pp. 451-499.

[97] A. Ishimaru, *Electromagnetic Wave Propagation, Radiation, and Scattering*, Englewood Cliffs, New Jersey: Prentice Hall, 1991.

[98] P. K. Bhagat and W. Kerrick, "Ultrasonic characterization of aging in skin tissue", *Ultrasound in Medicine and Biology*, vol. 6, pp. 369-375, 1980.

[99] F. S. Foster, M. Strban, and G. Austin, "The ultrasound macroscope: Initial studies of breast tissue", *Ultrasonic Imaging*, vol. 6, pp. 243-261, 1984.

[100] X. Chen, D. Phillips, K. Q. Schwartz, J. G. Mottley, and K. J. Parker, "The measurement of backscatter coefficient from a broadband pulse-echo system: A new formulation", *IEEE Transactions on Ultrasonics, Ferroelectrics, and Frequency Control*, vol. 44, pp. 515-525, 1997.

[101] E. L. Madsen, *Method of determination of acoustic backscatter and attenuation coefficients independent of depth and instrumentation*, in *Ultrasonic Scattering in Biological Tissues*, K.K. Shung and G.A. Thieme, Editors. 1993, CRC Press: Boca Raton. pp. 205-249.

[102] L. X. Yao, J. A. Zagzebski, and E. L. Madsen, "Backscatter coefficient measurements using a reference phantom to extract depth-dependent instrumentation factors", *Ultrasonic Imaging*, vol. 12, pp. 58-70, 1990.

[103] M. O'Donnell and J. G. Miller, "Quantitative broadband ultrasonic backscatter: An approach to nondestructive evaluation in acoustically inhomogeneous materials", *Journal of Applied Physics*, vol. 52, pp. 1056-1065, 1981.

[104] D. Nicholas, C. R. Hill, and D. K. Nassiri, "Evaluation of backscattering coefficients for excised human tissues: Principles and techniques", *Ultrasound in Medicine and Biology*, vol. 8, pp. 7-15, 1982.

[105] J. W. Goodman, *Introduction to Fourier Optics*, New York: McGraw-Hill, 1996.

[106] J. A. Zagzebski, Z. F. Lu, and L. X. Yao, "Quantitative ultrasound imaging: in vivo results in normal liver", *Ultrasonic Imaging*, vol. 15, pp. 335-351, 1993.

[107] Z. F. Lu, J. A. Zagzebski, and F. T. Lee, "Ultrasound backscatter and attenuation in human liver with diffuse disease", *Ultrasound in Medicine and Biology*, vol. 25, pp. 1047-1054, 1999.

[108] K. A. Wear, B. S. Garra, and T. J. Hall, "Measurements of ultrasonic backscatter coefficients in human liver and kidney in vivo", *Journal of the Acoustical Society of America*, vol. 98, pp. 1852-1857, 1995.

[109] J. F. Faran, "Sound scattering by solid cylinders and spheres", *Journal of the Acoustical Society of America*, vol. 23, pp. 405-418, 1951.

[110] E. L. Madsen, *et al.*, "Interlaboratory comparison of ultrasonic backscatter, attenuation, and speed measurements", *Journal of Ultrasound in Medicine*, vol. 18, pp. 615-631, 1999.

[111] T. Lin, J. Ophir, and G. Potter, "Frequency-dependent ultrasonic differentiation of normal and diffusely diseased liver", *Journal of the Acoustical Society of America*, vol. 82, pp. 1131-1138, 1987.

[112] S. Murakami and Y. Miki, "Human skin histology using high-resolution echography", *Journal of Clinical Ultrasound*, vol. 17, pp. 77-82, 1989.

[113] F. B. Jensen, W. A. Kuperman, M. B. Porter, and H. Schmidt, *Computational Ocean Acoustics (pages 201-202)*, New York: Springer-Verlag, 2000.

[114] H. J. Huisman, J. M. Thijssen, D. J. T. Wagener, and G. J. E. Rosenbusch, "Quantitative ultrasonic analysis of liver metastasis", *Ultrasound in Medicine and Biology*, vol. 24, pp. 67-77, 1998.

[115] J. C. Bamber and C. R. Hill, "Ultrasonic attenuation and propagation speed in mammalian tissues as a function of temperature", *Ultrasound in Medicine and Biology*, vol. 5, pp. 149-157, 1979.

[116] N. Akashi, J. Kushibiki, N. Chubachi, and F. Dunn, "Acoustic properties of selected bovine tissues in the frequency range 20-200 MHz", *Journal of the Acoustical Society of America*, vol. 98, pp. 3035-3039, 1995.

[117] D. K. Taniguchi, R. W. Martin, J. Myers, and F. E. Silverstein, "Measurement of the ultrasonic attenuation of fat at high frequency", *Academic Radiology*, vol. 1, pp. 114-120, 1994.

[118] P. M. Gammell, D. H. L. Croissette, and R. C. Heysek, "Temperature and frequency dependence of ultrasonic attenuation in selected tissues", *Ultrasound in Medicine and Biology*, vol. 5, pp. 269-277, 1979.

[119] I. Brown, "Scanning electron microscopy of human dense fibrous tissue", *Journal of Anatomy*, vol. 113, pp. 159-168, 1972.

[120] A. M. Kligman, *The biology of the stratum corneum*, in *The Epidermis*, W. Montagna and W.C. Lobitz, Editors. 1964, Academic Press: New York. pp. 387-433.

[121] G. Sommer, R. Stern, and H. Chen, "Cirrhosis: US Images with narrow band filtering", *Radiology*, vol. 165, pp. 425-430, 1987.

[122] B. J. Oosterveld, J. M. Thijssen, P. C. Hartman, and G. J. E. Rosenbusch, "Detection of diffuse liver disease by quantitative echography: Dependence on *a priori* choice of parameters", *Ultrasound in Medicine and Biology*, vol. 19, pp. 21-25, 1993.

[123] I. Schnittger, A. Vieli, J. E. Heiserman, B. A. Director, M. E. Billingham, S. G. Ellis, R. S. Kernoff, T. Takamoto, and R. L. Popp, "Ultrasonic tissue characterization: detection of acute myocardial ischemia in dogs", *Circulation*, vol. 72, pp. 193-199, 1985.

[124] K. A. Wear, T. A. Shoup, and R. L. Popp, "Ultrasonic characterization of canine myocardium contraction", *IEEE Transactions on Ultrasonics, Ferroelectrics, and Frequency Control*, vol. UFFC-33, pp. 347-353, 1986.

[125] L. Clifford, P. Fitzgerald, and D. James, "Non-Rayleigh first-order statistics of ultrasonic backscatter from normal myocardium", *Ultrasound in Medicine and Biology*, vol. 19, pp. 487-495, 1993.

[126] P. M. Shankar, V. A. Dumane, J. M. Reid, V. Genis, F. Forsberg, C. W. Piccoli, and B. B. Goldberg, "Classification of ultrasonic B-mode images of breast masses using Nakagami distribution", *IEEE Transactions on Ultrasonics, Ferroelectrics, and Frequency Control*, vol. 48, pp. 569-580, 2001.

[127] J.-F. Chen, E. L. Madsen, and J. A. Zagzebski, "A method for determination of frequency-dependent effective scatterer number density", *Journal of the Acoustical Society of America*, vol. 95, pp. 77-85, 1994.

[128] R. F. Wagner, M. F. Insana, and D. G. Brown, "Statistical properties of radio-frequency and envelope-detected signals with applications to medical ultrasound", *Journal of the Acoustical Society of America*, vol. 4, pp. 910-922, 1987.

[129] J. S. Daba and M. R. Bell, "Statistics of the scattering cross-section of a small number of random scatterers", *IEEE Transactions on Antennas and Propagation*, vol. 43, pp. 773-783, 1995.

[130] Rayleigh, "On the resultant of a large number of vibrations of the same pitch and of arbitrary phase", *Philosophical Magazine (Series 5)*, vol. 10, pp. 73-78, 1880.

[131] S. O. Rice, "Statistical properties of a sine wave plus random noise", *Bell System Technical Journal*, vol. 27, pp. 109-157, 1948.

[132] J. G. Proakis, *Digital Communications (pages 43-44)*, New York: McGraw-Hill, 2000.

[133] E. Jakeman and R. J. A. Tough, "Generalized K distribution: A statistical model for weak scattering", *Journal of the Optical Society of America*, vol. 4, pp. 1764-1772, 1987.

[134] M. D. Yacoub, "Fading distributions and co-channel interference in wireless systems", *IEEE Antennas and Propagation Magazine*, vol. 42, pp. 150-158, 2000.

[135] P. M. Shankar, "A general statistical model for ultrasonic backscattering from tissues", *IEEE Transactions on Ultrasonics, Ferroelectrics, and Frequency Control*, vol. 47, pp. 727-736, 2000.

[136] W. Weibull, "A statistical distribution function of wide applicability", *Journal of Applied Mechanics*, vol. 18, pp. 293-297, 1951.

[137] D. Fernandes and M. Sekine, "Suppression of Weibull radar clutter", *IEICE Transactions on Communications*, vol. E76-B, pp. 1231-1235, 1993.

[138] E. W. Stacy, "A generalization of the gamma distribution", *Annals of Mathematical Statistics*, vol. 33, pp. 1187-1192, 1962.

[139] A. J. Coulson, A. G. Williamson, and R. G. Vaughan, "Improved fading distribution for mobile radio", *IEE Proceedings on Communications*, vol. 145, pp. 197-202, 1998.

[140] M. F. Insana, R. F. Wagner, B. S. Gara, D. G. Brown, and T. H. Shawker, "Analysis of ultrasound image texture via generalized Rician statistics", *Optical engineering*, vol. 25, pp. 743-748, 1986.

[141] J. A. Nelder and R. Mead, "A simplex method for function minimization", *The Computer Journal*, vol. 7, pp. 308-313, 1965.

[142] E. W. Stacy and G. A. Mihram, "Parameter estimation for a generalized gamma distribution", *Technometrics*, vol. 7, pp. 349-358, 1965.

[143] R. S. Raghavan, "A method for estimating parameters of K-distributed clutter", *IEEE Transactions on Aerospace and Electronic Systems*, vol. 27, pp. 238-246, 1991.

[144] V. Dutt and J. Greenleaf, "Speckle analysis using signal to noise ratios based on fractional order moments", *Ultrasonic Imaging*, vol. 17, pp. 251-268, 1995.

[145] D. R. Wingo, "Computing maximum-likelihood parameter estimates of the generalized gamma distribution by numerical root isolation", *IEEE Transactions on Reliability*, vol. 36, pp. 586-590, 1987.

[146] M. Abramowitz and I. A. Stegun, *Handbook of Mathematical Functions*, New York: Dover Publications, 1965.

[147] W. J. Conover, *Practical Nonparametric Statistics*, New York: John Wiley and Sons, 1980.

[148] W. Montagna and P. F. Parakkal, *The Structure and Function of Skin*, New York: Academic Press, 1974.

[149] H. W. Hager and L. J. Bain, "Inferential procedures for the generalized gamma distribution", *Journal of the American Statistical Association*, vol. 65, pp. 1601-1609, 1970.

[150] M. Gniadecka, R. Gniadecki, J. Serup, and J. Sondergaard, "Ultrasound structure and digital image analysis of the subepidermal low echogenic band in aged human skin: Diurnal changes and interindividual variability", *Journal of Investigative Dermatology*, vol. 102, pp. 362-365, 1994.

[151] J. A. Zagzebski, J.-F. Chen, F. Dong, and T. Wilson, "Intervening attenuation affects first-order statistical properties of ultrasound echo signals", *IEEE Transactions on Ultrasonics, Ferroelectrics, and Frequency Control*, vol. 46, pp. 35-40, 1999.

[152] C. C. Harland, S. G. Kale, P. Jackson, P. S. Mortimer, and J. C. Bamber, "Differentiation of common benign pigmented skin lesions from melanoma by high-resolution ultrasound", *British Journal of Dermatology*, vol. 143, pp. 281-289, 2000.

[153] C. Fournier, S. L. Bridal, G. Berger, and P. Laugier, "Reproducibility of skin characterization with backscattered spectra (12-25 MHz) in healthy subjects", *Ultrasound in Medicine and Biology*, vol. 27, pp. 603-610, 2001.

[154] B. I. Raju and M. A. Srinivasan, "Statistics of envelope of high frequency ultrasonic backscatter from human skin in vivo", *IEEE Transactions on Ultrasonics, Ferroelectrics, and Frequency Control*, accepted for publication, 2002.

[155] J. Serup and B. Staberg, "Ultrasound for assessment of allergic and irritant patch test reactions", *Contact Dermatitis*, vol. 17, pp. 80-84, 1987.

[156] S. Seidenari, A. Di Nardo, P. Pepe, and A. Giannetti, "Ultrasound B scanning with image analysis for assessment of allergic patch test reactions", *Contact Dermatitis*, vol. 24, pp. 216-222, 1991.

[157] R. C. Molthen, P. M. Shankar, J. M. Reid, F. Forsberg, E. J. Halpern, C. W. Piccoli, and B. B. Goldberg, "Comparisons of the Rayleigh and K-distribution models using in vivo breast and liver tissue", *Ultrasound in Medicine and Biology*, vol. 24, pp. 93-100, 1998.

[158] V. M. Narayanan, P. M. Shankar, and J. M. Reid, "Non-Rayleigh statistics of ultrasonic backscattered signals", *IEEE Transactions on Ultrasonics, Ferroelectrics, and Frequency Control*, vol. 41, pp. 845-852, 1994.

[159] D. E. Robinson, L. S. Wilson, and T. Bianchi, "Beam pattern (diffraction) correction for ultrasonic attenuation measurement", *Ultrasonic Imaging*, vol. 6, pp. 293-303, 1984.

[160] J. Serup, B. Staberg, and P. Klemp, "Quantification of cutaneous aedema in patch test reactions by measurement of skin thickness with high-frequency pulsed ultrasound", *Contact Dermatitis*, vol. 10, pp. 88-93, 1984.

[161] S. Gonzalez, E. Gonzalez, W. M. White, M. Rajadhyaksha, and R. R. Anderson, "Allergic contact dermatitis: Correlation of in vivo confocal imaging to routine histology", *Journal of the American Academy of Dermatology*, vol. 40, pp. 708-713, 1999.

[162] M. F. Insana, J. Wood, T. J. Hall, G. G. Cox, and L. Harrison, "Effects of endothelin-1 on renal microvasculature measured using quantitative ultrasound", *Ultrasound in Medicine and Biology*, vol. 21, pp. 1143-1151, 1995.

[163] M. V. Menon, "Estimation of the shape and scale parameters of the Weibull distribution", *Technometrics*, vol. 5, pp. 175-182, 1963.

[164] L. Devroye, *Non-Uniform Random Variate Generation*, New York: Springer-Verlag, 1986.

[165] V. B. Parr and J. T. Webster, "A method for discriminating between failure density functions used in reliability predictions", *Technometrics*, vol. 7, pp. 1-10, 1965.